

Sverre Aas Myhr
Juel Petter Bergseth

Optimization program for single-span suspension bridges

Aerodynamic stability and cost-optimization

Master's thesis in Civil and Environmental Engineering

Supervisor: Ole Øiseth

Co-supervisor: Øyvind Wiig Petersen

June 2022

Sverre Aas Myhr
Juel Petter Bergseth

Optimization program for single-span suspension bridges

Aerodynamic stability and cost-optimization

Master's thesis in Civil and Environmental Engineering
Supervisor: Ole Øiseth
Co-supervisor: Øyvind Wiig Petersen
June 2022

Norwegian University of Science and Technology
Faculty of Engineering
Department of Structural Engineering



MASTER THESIS 2022

SUBJECT AREA: Structural Dynamic	DATE: 10.06.2021	NO. OF PAGES: 70
-------------------------------------	---------------------	---------------------

TITLE:

Optimization program for single-span suspension bridges

Optimaliseringsprogram for ett-spenns hengebruer

BY:

Sverre Aas Myhr and Juel Petter Bergseth



SUMMARY:

This thesis follows the development of an optimization program for single-span suspension bridges. The program calculates the aerodynamic stability limit for a parameter configuration and compares this to a pre-defined criterion. This defines the constraint in the optimization, whereas the objective is to minimize the cost. For the time being, the program optimizes the configuration of tower and girder height as the main parameters. With the use of advanced regression methods, the program creates surrogate models for the aerodynamic derivatives, enabling parametrization of girder section parameters with less extensive wind-tunnel testing. A parametric Abaqus model is implemented in the program to calculate modal properties.

The program is tested and developed for the Langenuen crossing as an example. This concept includes an aluminum girder, which makes the dynamic performance highly relevant due to its low weight and reduced stiffness compared to steel. The program returned the optimal configuration to be a tower height of 220 meters and a girder height of 3.68 meters, yielding a critical wind speed of 76.4 m/s and a total cost of 2001 MNOK. Some simplifications are made in the input data for the case example, leaving room for some uncertainties in the results. However, the program works within its purpose and shows that there is potential in this approach to concept optimization of suspension bridges.

This potential lies in reducing the resources spent on wind-tunnel testing drastically, as well as bringing forward more optimal design solutions. The program can also be expanded to include additional parameters, constraints, and objectives to enable more general optimization.

RESPONSIBLE TEACHER: Professor Ole Øiseth

SUPERVISOR(S): Professor Ole Øiseth, Postdoc Øyvind Wiig Petersen

CARRIED OUT AT: Department of Structural Engineering, NTNU

Abstract

As bridges become longer and more slender, their aerodynamic behaviour comes to importance in the design phase. The interaction of wind flow and structure motion introduces aerodynamic stiffness and damping, which affects the structural properties. In strong winds, instability phenomena can occur, where the increasing response can cause structural failure. The calculations of these stability limits are rather complex, including wind-tunnel testing to describe the aerodynamic characteristics.

The objective of this project was to develop a program to determine the stability limits for suspension bridge concepts, and use this in a parametric optimization with respect to cost. With wind-tunnel data for a range of cross-sections, the program creates surrogate models of the aerodynamic derivatives with the use of Gaussian Process Regression. Together with modal properties from a parametric Abaqus model, the stability limits could be calculated for different concept configurations. The stability limit became a constraint in the optimization function, whereas minimizing the cost was the objective. An automatic optimization could follow by defining a parameter space for the main parameters, tower and girder height.

The program was developed and tested for the Langenuen crossing. The main span of 1235 meters is supposed to be crossed with an aluminium girder, making it the first of its kind. The program found the optimal design within the bounds to be a tower height of 220 meters and a girder height of 3.68 meters. This configuration gave a critical wind speed of 76.4 m/s and an estimated cost of approximately 2001 MNOK. The results come with some uncertainty, but prove the potential of this approach to concept optimization. The program is adaptable to concept studies of other suspension bridges. Additional parameters, constraints, and objectives can be implemented for a more general optimization.

Sammendrag

Med bruer som blir stadig lengre og slankere får aerodynamikk en større rolle i designfasen. Interaksjonen mellom luftstrøm og bevegelse i bruene medfører aerodynamiske bidrag til systemets totale stivhet og demping. Ved høye vindstyrker kan instabilitetsfenomener forekomme, med økende respons som fører til brudd i konstruksjonen. Stabilitetsberegninger av denne typen er komplekse, og beskrivelse av den aerodynamiske karakteristikken krever testing i vindtunnel.

Målet med dette prosjektet var å utvikle et program for å bestemme stabilitetsgrenser for hengebrukonsepter, og bruke dette i en parametrisert optimalisering med hensyn til kostnad. Med vindtunnel data for et utvalg av brutverrsnitt, lager programmet surrogatmodeller av de aerodynamisk deriverte ved bruk av Gaussian Process Regression. Sammen med modale egenskaper fra en parametrisert modell i Abaqus kunne stabilitetsgrensene bli beregnet for forskjellige konseptkonfigurasjoner. En grenseverdi for kritisk vind samt minimering av kostnad utgjorde optimaliseringsfunksjonen. Ved å sette et parameterrom kunne optimaliseringen bli utført med hensyn til de to hovedparameterne, tårnhøyde og tverrsnittshøyde.

Programmet ble utviklet og testet for kryssingen av Langenuen. Hovedspennet på 1235 er forespeilet å skulle krysses med en brukasse i aluminium, noe som gjør det til den første av sin type. Programmet fant den optimale konfigurasjonen til å være en tårnhøyde på 220 meter og tverrsnittshøyde på 3.68 meter. Dette ga en kritisk vindhastighet på 76.4 m/s og en estimert kostnad på 2001 MNOK. Resultatet kommer med noe usikkerhet, men viser et potensial i denne tilnærmingen til konseptoptimalisering. Programmet kan tilpasses og brukes i lignende konseptstudier. Ved å implementere nye parametre, begrensninger og objektiver kan optimaliseringen gjøres mer generell.

Preface

This report is the result of 20 weeks of work during the spring of 2022, and concludes our M.Sc. degree at the Department at Structural Engineering, at NTNU Trondheim.

The development of the program has been very interesting and rewarding, but also challenging with a lot of trial-and-error. Bridge aerodynamics, Python programming, and parametric modelling are some of the many topics we have both gained a greater understanding of throughout this project.

We would like to express our gratitude to our supervisors, Professor Ole Øiseth and Postdoctor Øyvind Wiig Petersen, for their guidance throughout this project. A special thanks to Øyvind for also providing us with the parametric Abaqus model. Lastly, we would like to thank Jungao Wang from the NPRA for great inspiration on how to structure the script used to calculate the critical wind speed.

Sverre Aas Myhr and Juel Petter Bergseth
Trondheim, 10.06.2022

Contents

Abstract	v
Sammendrag	vii
Preface	ix
Contents	xi
Figures	xiii
Tables	xv
Symbols and acronyms	xvii
1 Introduction	1
2 Theory	3
2.1 Suspension bridges	3
2.2 Modal analysis	4
2.3 Spectral analysis	5
2.4 Wind induced response	7
2.4.1 Buffeting theory	7
2.4.2 Aerodynamic derivatives	10
2.4.3 Vortex shedding	11
2.5 Motion induced instabilities	13
2.5.1 Static divergence	14
2.5.2 Galloping	15
2.5.3 Dynamic instability in torsion	15
2.5.4 Multi-modal flutter	16
2.5.5 Eigenvalue problem	16
2.6 Gaussian Processes Regression	17
2.6.1 Gaussian Processes	18
2.6.2 Kernels	19
2.6.3 Regression predictions	19
2.7 Optimization	20
2.7.1 SciPy Optimize	20
2.7.2 Bayesian Optimization	20
3 Methodology	23
3.1 General workflow	23
3.2 Global Abaqus model	25
3.3 Cross-section parametrization	28
3.4 Wind-tunnel testing	32
3.5 AD surrogate models	38
3.6 Calculation of critical wind speed	39

3.7	Optimization	39
3.8	Buffeting response	42
4	Optimization program	47
4.1	Objective and structure	47
4.2	Quick run with Langenuen example	48
5	Langenuen case study	51
5.1	Modal analysis	51
5.2	Vortex shedding	53
5.3	Static coefficients	53
5.4	Aerodynamic derivatives	55
5.5	Optimization	58
5.6	Buffeting response	61
5.7	Further discussions	65
6	Conclusions	71
7	Further work	73
	Bibliography	75
A	Optimize Program	79
A.1	User manual	79
A.1.1	Overview	79
A.1.2	How to run	83
B	Modal analysis	85
B.1	Mode shapes	86
B.2	Modal properties	88
C	Wind-tunnel results	89
C.1	ADs: sampling data	89
C.2	ADs: surrogate models	95
D	Optimization	113

Figures

1.1	Initial objective and solution strategy	2
2.1	Suspension bridge main components and load bearing mode	3
2.2	The continuous DOFs of a line-like structure	8
2.3	Illustration of a line-like structure exposed to buffeting load	9
2.4	An illustration of how vortex shedding appears on the cross-section of a line-like structure	12
2.5	A plot of the vortex shedding frequency in interaction with a structural system	13
2.6	Illustration of how the system is affected by the change in eigenvalues	17
2.7	Illustration of the difference between linear regression and linear interpolation	18
2.8	Illustration of the predicted mean drawn both from the prior and posterior distribution	20
2.9	Plots showing one iteration of the Bayesian Optimization algorithm	21
3.1	Flowchart illustrating the initial idea of the program. The section references indicates where each part is described.	24
3.2	The steps illustrating the establishment of the global Abaqus model	27
3.3	Illustrations of the cross-sections that are to be tested in the wind-tunnel	29
3.4	Illustrations of the geometries of the panels used in the transverse panel concept	30
3.5	Illustration of the transverse panel concept developed by Dr. Techn Olav Olsen for NPRA. Bulkheads are not shown.	31
3.6	The reference system for the sections models in the wind-tunnel tests	33
3.7	Photo of a section model with railing	34
3.8	Railing drawings	35
3.9	Photo of the section model fixed into the forced vibration rig	36
3.10	Motion plot for quasi steady test	37
3.11	Motion plots for harmonic tests	37
3.12	Illustration of a surrogate model	38
3.13	Plot illustrating the smoothing of the force coefficients	43
4.1	Folder structure for the optimization program	48
5.1	Surface plots of the eigenfrequencies for first asymmetric vertical and torsional mode	52
5.2	Static coefficients resulting from wind-tunnel tests of all section models	54
5.3	Plots of ADs resulting from wind-tunnel tests of the 4.0 meter girder	56
5.4	Surrogate models for all the ADs	57

5.5	3D-plots for the critical wind speed and configuration cost as function of tower and girder height. The green scatter plot depicts the configurations where $V_{cr} > 76\text{m/s}$.	59
5.6	Argand diagram illustrating coupled the failure mode for $h_g = 3.68\text{m}$ and $h_t = 220\text{m}$. The plot to the right is an up-scaled version of the plot to the left.	60
5.7	Cable force as function of tower height. Girder height = 4.0	60
5.8	3D-plot showing the cost per part for the Langenuen suspension bridge	61
5.9	Plots of the modal frequency response function for $U = 30\text{ m/s}$	62
5.10	Plots of the modal load spectra for $U = 30\text{ m/s}$	62
5.11	Plots of the modal coordinate spectra for $U = 30\text{ m/s}$	63
5.12	Plots of the maximum response along the bridge length for $U = 30\text{ m/s}$	63
5.13	Sensitivity study of the spacial maximum standard deviation of the buffeting response	64
5.14	Total damping ratio and eigenfrequency for symmetric vertical and torsional modes	66
5.15	Total damping ratio plotted towards increasing mean wind speed	66
5.16	Plot showing 2D-slices for the critical wind speed taken at three different tower heights. The girder height with the heighest and lowest V_{cr} are annotated	68
A.1	General overview of the structure of the program.	79
A.2	The FEM_Results folder.	80
A.3	The Scripts folder.	81
A.4	The suspensionbridge folder	83
C.1	Aerodynamic derivatives sampling data for girder height 3.5 m.	90
C.2	Aerodynamic derivatives sampling data for girder height 3.75 m.	91
C.3	Aerodynamic derivatives sampling data for girder height 4.0 m.	92
C.4	Aerodynamic derivatives sampling data for girder height 4.25 m.	93
C.5	Aerodynamic derivatives sampling data for girder height 4.5 m.	94
C.6	Surrogate model for P1*	95
C.7	Surrogate model for P2*	96
C.8	Surrogate model for P3*	97
C.9	Surrogate model for P4*	98
C.10	Surrogate model for P5*	99
C.11	Surrogate model for P6*	100
C.12	Surrogate model for H1*	101
C.13	Surrogate model for H2*	102
C.14	Surrogate model for H3*	103
C.15	Surrogate model for H4*	104
C.16	Surrogate model for H5*	105
C.17	Surrogate model for H6*	106
C.18	Surrogate model for A1*	107
C.19	Surrogate model for A2*	108
C.20	Surrogate model for A3*	109
C.21	Surrogate model for A4*	110
C.22	Surrogate model for A5*	111
C.23	Surrogate model for A6*	112

Tables

3.1	Material properties used in the Abaqus model	26
3.2	Variables in global Abaqus model	28
3.3	Summary of the section properties for the different girder heights.	32
3.4	Summary of the tests ran in the wind-tunnel.	36
3.5	Price factors used for the objective function.	40
5.1	Modal properties for $h_g = 4.0\text{m}$ and $h_t = 206\text{m}$	51
5.2	Maximum and minimum frequency for VS1 and TS1 along with the respective configuration and difference in percent	52
5.3	Summary of the results of the static coefficient tests.	55
B.1	Modal properties for the optimal design configuration. $h_t = 220\text{m}$, $h_g = 3.68\text{m}$	88
D.1	Flutter speed for all generated configurations	114
D.2	Total cost for all generated configurations	115

Symbols and acronyms

Acronyms

AD	Aerodynamic Derivative
ASD	Auto-spectral Density
CSD	Cross-spectral Density
DOF	Degree of Freedom
FEM	Finite Element Method
FRF	Frequency Response Function
GPR	Gaussian Process Regression
GUI	Graphical user interface
IDE	Integrated development environment
LN22	Langenuen 2022. Reference for the cross-section models.
MDOF	Multi-Degree-of-Freedom
N400	Bridge designing handbook from NPRA.
NPRA	Norwegian Public Road Administration
NTNU	Norwegian University of Science and Technology
SDOF	Single-Degree-of-Freedom
TMD	Tuned mass damper
VIV	Vortex Induced Vibration

Symbols

M, C, K	System mass, damping and stiffness matrices
ϕ	Mode shape vector
M_n, C_n, K_n	Modal mass, damping and stiffness for mode n
$\ddot{\eta}, \dot{\eta}, \eta$	Acceleration, velocity and displacement in terms of modal coordinates

r_y, r_z, r_θ	Physical DOFs. Referred to as horizontal, vertical and pitching, respectively.
P_n	Modal load for mode n
\ddot{r}, \dot{r}, r	Acceleration, velocity and displacement in terms of physical coordinates
H	Frequency response function
S_q	Load spectra cross-correlation matrix
S_η	Modal coordinate response spectra cross-correlation matrix
S_r	Response spectra cross-correlation matrix
q	Load vector
q_D, q_L, q_θ	Drag force, lifting force and pitching moment
ρ	Density (air density)
B	Width of line-like structure's cross-section
D	Height (depth) of line-like structure's cross-section
C_D, C_L, C_M	Drag force, lifting force and pitching moment coefficients
V_{rel}	Wind speed relative to line-like structure's motion
\bar{V}	Along mean wind speed
β	The relative wind speed's angle with the horizontal plane
α	Attacking angle of line-like structure
u, v, w	Turbulence components parallel to axes y, x, z, respectively
B_q	Buffeting load coefficient matrix
P_i, H_i, A_i	Aerodynamic derivatives
P_i^*, H_i^*, A_i^*	Normalized aerodynamic derivatives
V_{red}	Reduced wind velocity
K	Reduced frequency
ζ	Damping ratio
ζ_{ae}	Modal aerodynamic damping contribution
κ_{ae}	Modal aerodynamic stiffness contribution
$\tilde{\mathbf{M}}, \tilde{\mathbf{C}}, \tilde{\mathbf{K}}$	Modal mass, damping and stiffness matrices
$\tilde{\mathbf{C}}_{ae}, \tilde{\mathbf{K}}_{ae}$	Modal aerodynamic damping- and -stiffness matrices
$\tilde{\mathbf{Q}}$	Modal load matrix

$\tilde{\mathbf{H}}$	Modal frequency response function
$\tilde{\mathbf{E}}$	Modal impedance matrix
L	Length of line-like structure
L_{exp}	Wind-exposed length of line-like structure
V_{cr}	Critical wind velocity
m, k	Mean and co-variance (kernel) functions
\mathcal{GP}	Gaussian distribution
μ, \mathbf{K}	n-dimensional mean- and co-variance matrix functions
\mathcal{N}_n	n-dimensional Gaussian distribution
ν, l	Length scale and smoothness parameter
E, G	Modulus of elasticity and shear modulus
ν	Poisson ratio
I_{11}, I_{22}	Second moment of inertia around axis 1 and 2
i_{11}, i_{22}	Moment of inertia around axis 1 and 2
I_t	Torsional stiffness
A_m	Area within thin-walled cross-section mid-line
h_t, h_g	Tower height and girder height

Chapter 1

Introduction

With the Tacoma Narrows Bridge collapse in 1940 as an unfortunate example, the need for knowledge about the aerodynamic behaviour of suspension bridges was addressed [1][2]. The collapse was, in fact, due to aerodynamic instability, which is a state where the structure loses its damping or stiffness, and thus, its ability to counteract increasing response [3]. The Norwegian Bridge Designing handbook, *N400 Bruprosjektering*, requires a control towards such phenomena in the design of new suspension bridges. Such instabilities result from the interaction between the structural static and dynamic responses and the airflow around the girder section. This makes the calculation a rather demanding exercise, including experimental wind-tunnel tests. Because of the complexity of these calculations, the optimal design solutions are difficult to predict only from engineering judgement and previous experience.

The E39-project, creating ferry-free connections along the western coast of Norway, includes several groundbreaking fjord-crossings [4]. A variety of suspension bridges are among the current suggestions for the crossings, which brings forward the need for design methods that can optimize the different concepts to lower the cost in an effective manner. For the Langenuen crossing, the world's first suspension bridge with an aluminium girder has been suggested. The light weight, along with the decreased stiffness compared to steel, makes the dynamics of such a bridge challenging. Aerodynamic behaviour is then highly relevant.

The objective of this project is to develop a program that can be useful in choosing the optimal concepts for suspension bridges with regard to aerodynamic design and material cost. The program will be tested with the Langenuen case as an example, but adaptability is a priority, such that it can be utilized for future concept studies. Another intention is to keep the program versatile to facilitate further expansions. This project may therefore be regarded as a pilot project.

The strategy is to create a looping optimization algorithm with two main parameters: tower and girder height. For each configuration of these parameters, the stability limit as well as the material cost will be calculated. The stability limit calculations will be done using aerodynamic derivatives (ADs), which will be determined experimentally with wind-tunnel tests. Surrogate models are then to be made with the wind-tunnel data to refine the girder height parameter space. By implementing a parametric FE-model in the loop, the modal properties can be calculated. The idea is then to make a looping algorithm to approach the cheapest parameter

configuration, which simultaneously passes the stability limit criteria of 76 m/s. The initial approach to the objective is summed up in Figure 1.1.

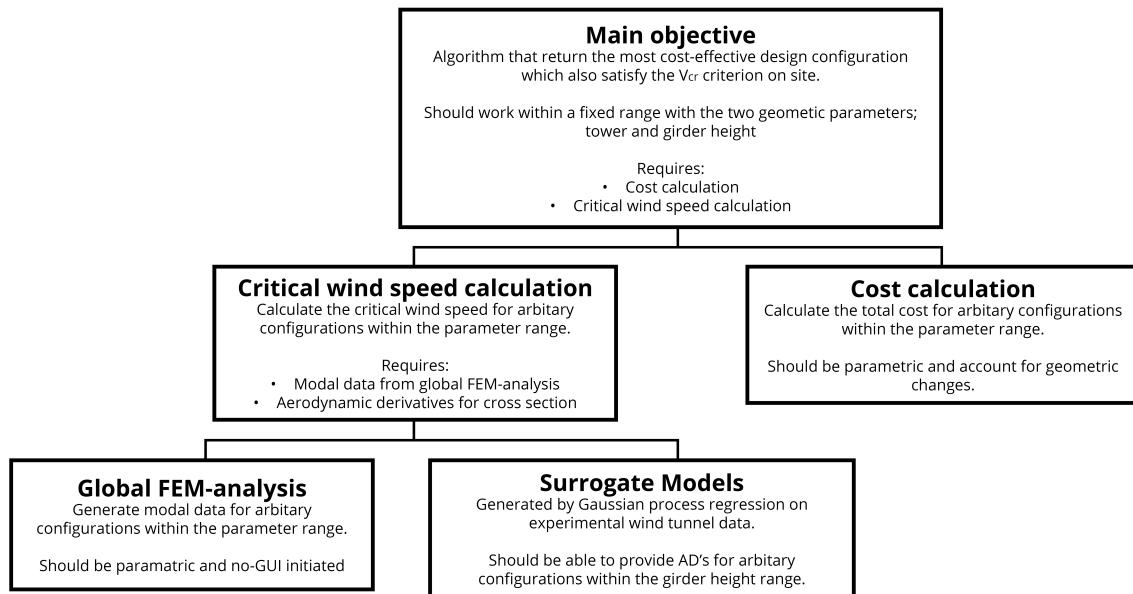


Figure 1.1: Initial objective and solution strategy

The optimization is limited to two main parameters. Some parameter dependencies are planned to be implemented, such as main cable and hanger cross-section. A detailed tower and foundation design is left out of the scope of this work. The program should not include aspects beyond the stability limits, material costs, and buffeting response analysis, such that an optimal design cannot be drawn directly from the optimization. The main priority is to get the code running. Details are then thought to be compromised to ensure progress towards this milestone. These details can be further improved when the code is running stable.

In the following chapter, the theory behind the stability limit and buffeting response calculations is presented. Chapter 3 presents the procedure of developing the program, while Chapter 4 presents its final structure and how it works. In Chapter 5, the results from the case study of Langenuen are presented, with a discussion on inaccuracies and room for improvement in the program judged from this case example. Chapter 6 concludes the work in the context of the project purpose, and Chapter 7 suggests further work that can be done from this.

Chapter 2

Theory

2.1 Suspension bridges

Suspension bridges have been used since the early 1800s with main spans ranging typically from around 600 to over 2000 meters [2][5]. The main components of a suspension bridge, as well as their main load-bearing mode, are shown in Figure 2.1.

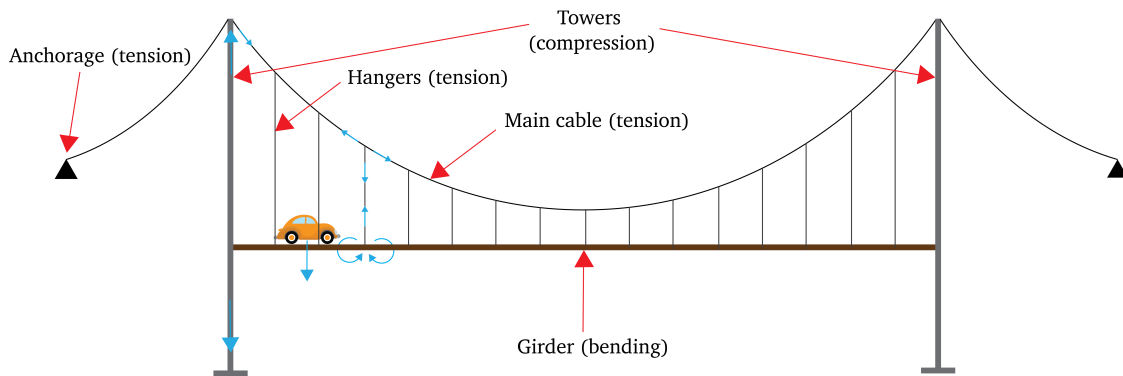


Figure 2.1: Suspension bridge main components and load bearing mode

In addition to loads such as self-weight and vehicle loading, wind loading is of great importance for the design of suspension bridges [1]. A suspension bridge has a low relative stiffness, as compared to traditional simple bridges, due to its entirely flexible cable system and lengthy spans. Dynamic wind loading may then cause large motions in the structure. This gives rise to a variety of challenges, such as fatigue and aerodynamic stability. The collapse of the Tacoma Narrows Bridge in 1940 demonstrated that standard design processes and calculations were insufficient for such complex structures [2]. The 853 meter spanning bridge collapsed 4 months after its completion, due to large torsional motion in a 19 m/s wind. This provoked a knowledge development introducing more sophisticated analytical methods, including vibration analysis with a modal approach [1]. Wind-tunnel testing is now used to forecast the aerodynamic behavior of girder sections. With ever-increasing computational power, detailed numerical FE-analysis has become the modern approach to the design of suspension bridges.

This allows for longer and more extreme bridge structures, with Çanakkale Bridge in Turkia as the current world record holder, spanning 2023 meters [5].

2.2 Modal analysis

Modal analysis can be done to describe the general dynamic properties of a structure in the form of its natural modes [6]. That is, the characteristic displacement patterns of the structure with the corresponding frequencies at which these mode shapes will occur. For a structural system, the mode shapes can be described by the DOFs of the structure, which can be both displacements and rotations at discrete locations. There are as many natural modes as there are DOFs in the system. Demanding a force-equilibrium for a structural system in free vibration, we obtain the equation of motion (EOM).

$$\mathbf{M}\ddot{r}(t) + \mathbf{C}\dot{r}(t) + \mathbf{K}r(t) = 0 \quad (2.1)$$

As can be seen from this, the motion of the structure is dependent on the spatial distribution of the mass, damping, and stiffness properties [6]. By assuming a harmonic motion, the eigenvalue problem can be derived from Equation (2.1). For simplicity, damping is neglected in this demonstration.

$$(\mathbf{K} - \omega^2\mathbf{M})\phi = 0 \quad (2.2)$$

The natural modes are obtained by looking for non-trivial solutions of this equation. Each of these solutions consists of a natural frequency, ω_n , and a corresponding mode shape vector, ϕ_n .

Such matrix systems are directly applicable only for idealized systems where the mass, stiffness (and damping) is directly connected (lumped) to the DOFs. Continuous systems with distributed properties are, however, soluble with a so-called generalized SDOF approach [7]. By employing the principle of virtual work to such a system, the generalized properties for each of the considered mode shapes $\varphi_n(x)$ can be derived as

$$M_n = \int_0^L m(x)\varphi_n(x)^2 dx + \sum_{i=1}^k m_i\varphi_n(x_i)^2 \quad (2.3)$$

$$C_n = \int_0^L c(x)\varphi_n(x)^2 dx + \sum_{i=1}^k c_i\varphi_n(x_i)^2 \quad (2.4)$$

$$K_n = \int_0^L EI(x)\varphi_n''(x)^2 dx + \sum_{i=1}^k k_i\varphi_n(x_i)^2 \quad (2.5)$$

The equation of motion can then be solved with respect to the generalized coordinates $\eta_n(t)$ for each of the considered modes to obtain the time-scaling of the current mode.

$$M_n\ddot{\eta}_n(t) + C_n\dot{\eta}_n(t) + K_n\eta(t) = 0 \quad (2.6)$$

As for simple SDOF systems, the natural frequency of each mode is determined by [7]

$$\omega_n = \sqrt{\frac{K_n}{M_n}} \quad (2.7)$$

Then, the principle of superposition can be applied to determine the total motion in the physical continuous DOFs [7].

$$r(x, t) = \sum_{n=1}^{n_{modes}} \eta_n(t) \varphi_n(x) \quad (2.8)$$

The mode shapes of the structure $\varphi_n(x)$, must be known in advance for the generalized SDOF approach to be applicable [7]. Without going into detail on this, it can be handled analytically by solving the beam differential equation for the particular system [6]. Alternatively, it can be estimated numerically with an FE-approach. A simple example is a vibrating string that has the natural mode shapes

$$\varphi_n(x) = \sin \frac{n\pi x}{L} \quad (2.9)$$

Approximately the same shape will appear for simply supported beams with uniformly distributed stiffness, only that shear strains will cause a little distortion [8]. Thus, similar shapes are also to be expected for simply supported bridge girders.

In the presence of loading on generalized SDOF systems, its effect on each mode will depend on how it coincides with the mode shape of the current mode [7]. Analogous to the determination of the generalized system parameters, M_n, C_n, K_n , the modal load can be calculated as

$$P_n = \int_0^L p(x, t) \varphi_n(x) dx + \sum_{i=1}^k p_i \varphi_n(x_i) \quad (2.10)$$

The response to a fluctuating load will also be highly dependent on the frequency of the load fluctuations. An approach to describe this sensitivity is the Frequency Response Function (FRF) [9] [7]. An interpretation of this is a recording of the response in a system that is exposed to a harmonic loading with a constant amplitude, but with varying frequency. The response can then be plotted in the frequency domain, which results in peaks around the natural frequencies. The FRF of a linear system is obtained by Fourier transforming the time domain response and dividing this by the Fourier transform of the time domain input.

$$\mathbf{H}(\omega) = [-\omega^2 \mathbf{M} + i\omega \mathbf{C} + \mathbf{K}]^{-1} \quad (2.11)$$

This relation is very useful, and can be utilized in further frequency domain analysis.

2.3 Spectral analysis

Stochastic processes, like wind loading, can sometimes appear chaotic and be hard to interpret in the time domain. It can therefore be convenient to Fourier transform the process to study its frequency compositions.

The Fourier transform is a mathematical operator that transform a process from the time or space domain into the frequency domain [10]. The transform is named after the French mathematician Joseph Fourier and is an important and commonly used operator in structural dynamics to enter back and forth into the frequency domain. Through integration, the time domain signal is decomposed into a sum of complex exponentials, each with its associated phase, frequency, and amplitude, whereas the latter is rendered along the new frequency axis.

For a given function $y(t)$ in the time-domain, the Fourier transform is given by Equation (2.12) [11]. The inverse Fourier transform is given by Equation (2.13).

$$Y(\omega) = \frac{1}{2\pi} \int_{-\infty}^{\infty} y(t)e^{-i\omega t} dt \quad (2.12) \quad y(t) = \int_{-\infty}^{\infty} Y(\omega)e^{i\omega t} d\omega \quad (2.13)$$

For an arbitrary stationary stochastic process $y(t)$, where the mean value and variance are invariant with absolute time, the condition

$$\int_{-\infty}^{\infty} |y(t)| dt < \infty \quad (2.14)$$

is not satisfied, and classical Fourier theory cannot be applied [11]. This difficulty can be overcome by utilizing time-domain process auto-correlation function, which indirectly contains information about the frequencies present in the stochastic process. The auto-correlation function is defined by Equation (2.15), and describe how correlated a time series is to a lagged version of itself. For a stationary process, the function depends only on the time separation τ and not the absolute time t .

$$R_{yy} = E[y(t)y(t + \tau)] \quad (2.15)$$

The auto-correlation function converges towards zero for large values of τ , and hereby satisfies the condition given in Equation (2.14) [11]. The process can now be transformed into the frequency domain as shown in Equation (2.16), which renders the auto spectral density spectrum.

$$S_{yy}(\omega) = \frac{1}{2\pi} \int_{-\infty}^{\infty} R_{yy}(\tau)e^{i\omega\tau} d\tau \quad (2.16)$$

The auto spectral density (ASD), sometimes referred to as power spectral density, contains information about which frequencies that dominates the stochastic process [11]. The area under the frequency bands is equal to the variance for the process, hence the ASD is always positive.

If a new stochastic process $x(t)$ is introduced, the same Fourier transform can be used on the cross-correlation function between the two processes [11]. The cross-correlation function is defined in Equation (2.17) and describes the correlation between the two processes relative to each other. The corresponding cross-spectral density (CSD) is defined in Equation (2.18). The area under frequency bands in the CSD is equal to the co-variance, meaning that the CSD can contain both positive and negative values.

$$R_{yx} = E[y(t)x(t + \tau)] \quad (2.17)$$

$$S_{yx}(\omega) = \frac{1}{2\pi} \int_{-\infty}^{\infty} R_{yx}(\tau) e^{i\omega\tau} d\tau \quad (2.18)$$

The ASD and CSD can be used in frequency domain analysis of structural systems subjected to stochastic loads [11]. The ASD provides information of which frequencies that are most prevalent in the stochastic loading, while the CSD can describe the load correlation for MDOF systems. A cross-correlation matrix, containing ASDs on the diagonal terms and CSDs on the off-diagonal terms, can thereby provide a complete description of the stochastic loading on an MDOF system. Using a system with two degrees of freedom, y and x , as an example, the cross-correlation matrix, or load spectra, is read

$$\mathbf{S}_q(\omega) = \begin{bmatrix} S_{yy} & S_{yx} \\ S_{xy} & S_{xx} \end{bmatrix} \quad (2.19)$$

The FRF was introduced in Equation (2.40), describing the structural systems sensitivity to loads with different frequencies [9] [7]. It can be derived that the response spectra can be calculated as

$$\mathbf{S}_r(\omega) = \mathbf{H}(\omega) * \mathbf{S}_q(\omega) \mathbf{H}(\omega)^T \quad (2.20)$$

where $*$ denotes the complex conjugated. The variance of the response may be found by integrating S_r along the frequency axis [11].

2.4 Wind induced response

When a line-like and deformable structure is exposed to wind, a rather complex load situation will occur [12]. Wind does most often have a time-varying presence, such that the pressure generated from the wind gives a dynamic load effect. For a deformable structure, this will induce motions that again affect the relative wind velocity and the wind pressure. The wind flow around the structure is also disturbed by the structure, and phenomena like vortex shedding may also produce a significant load contribution. Generally, the effects of wind loading can be sorted into four categories:

- Mean wind that can be considered as a static load
- Turbulence that generates a fluctuating wind pressure often named buffeting load
- Self-excited forces that are generated from the motion in the structure
- Load effects due to vortex shedding

2.4.1 Buffeting theory

For a line-like structure, such as a bridge girder, it is reasonable to assume that the deformations in the longitudinal direction are negligible, such that the motion can be described by the continuous DOFs $r_y(x, t)$, $r_z(x, t)$ and $r_\theta(x, t)$ as illustrated in Figure 2.2 [12]. For a defined time-period the wind is assumed to be stationary, such that the mean wind can be considered constant, generating a time-independent static load. This results in a time-independent mean displacement.

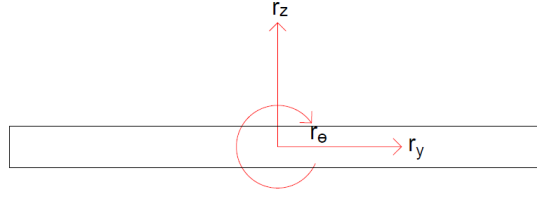


Figure 2.2: The continuous DOFs of a line-like structure

$$\mathbf{q}_{tot}(x, t) = \bar{\mathbf{q}}(x) + \mathbf{q}(x, t, \ddot{\mathbf{r}}, \dot{\mathbf{r}}, \mathbf{r}) \quad (2.21) \quad \mathbf{q}_{tot}(x, t) = [q_y \quad q_z \quad q_\theta]^T \quad (2.22)$$

$$\mathbf{r}_{tot}(x, t) = \bar{\mathbf{r}}(x) + \mathbf{r}(x, t) \quad (2.23) \quad \mathbf{r}_{tot}(x, t) = [r_y \quad r_z \quad r_\theta]^T \quad (2.24)$$

The wind fluctuations from the constant mean wind is then the turbulence. The turbulence can be decomposed to obtain a direct relation to the active DOFs [12]. The lateral turbulence component, $u(x, t)$, works parallel with the y-axis and the vertical turbulence component, $w(x, t)$, works parallel with the z-axis. The relative wind velocity is what generates pressure and hence, the buffeting load on the structure. With reference to Figure 2.3, the following relations can be established.

$$\begin{bmatrix} q_D(x, t) \\ q_L(x, t) \\ q_\theta(x, t) \end{bmatrix} = \frac{1}{2} \rho V_{rel}^2 \begin{bmatrix} D \cdot C_D(\alpha) \\ B \cdot C_L(\alpha) \\ B^2 \cdot C_M(\alpha) \end{bmatrix} \quad (2.25)$$

C_D, C_L and C_M are load coefficients that are dependent on the shape of the section of the structure [12].

The loads can be transferred to the directions of the DOFs using

$$\mathbf{q}_{tot}(x, t) = \begin{bmatrix} q_y \\ q_z \\ q_\theta \end{bmatrix}_{tot} = \begin{bmatrix} \cos \beta & -\sin \beta & 0 \\ \sin \beta & \cos \beta & 0 \\ 0 & 0 & 1 \end{bmatrix} \cdot \begin{bmatrix} q_D \\ q_L \\ q_\theta \end{bmatrix} \quad (2.26)$$

The relative wind velocity has a horizontal component ($\bar{V}(x) + u(x, t) - \dot{r}_y(x, t)$) and a vertical component ($w(x, t) - \dot{r}_z(x, t)$). A fair assumption is that the turbulence components and the structural velocity are much smaller in magnitude than the mean wind [12]. As a simplification, higher order terms of $u(x, t), w(x, t), \dot{r}_y(x, t)$ and $\dot{r}_z(x, t)$ are therefore neglected. The wind pressure and its angle can then be expressed as

$$\frac{1}{2} \rho V_{rel}^2 = \frac{1}{2} \rho [(\bar{V}(x) + u(x, t) - \dot{r}_y(x, t))^2 + (w(x, t) - \dot{r}_z(x, t))^2] \approx \rho \bar{V} \left(\frac{\bar{V}}{2} + u(x, t) - \dot{r}_y(x, t) \right) \quad (2.27)$$

$$\beta \approx \tan \beta = \frac{w(x, t) - \dot{r}_z(x, t)}{\bar{V} + u(x, t) - \dot{r}_y(x, t)} \approx \frac{w(x, t) - \dot{r}_z(x, t)}{\bar{V}} \quad (2.28)$$

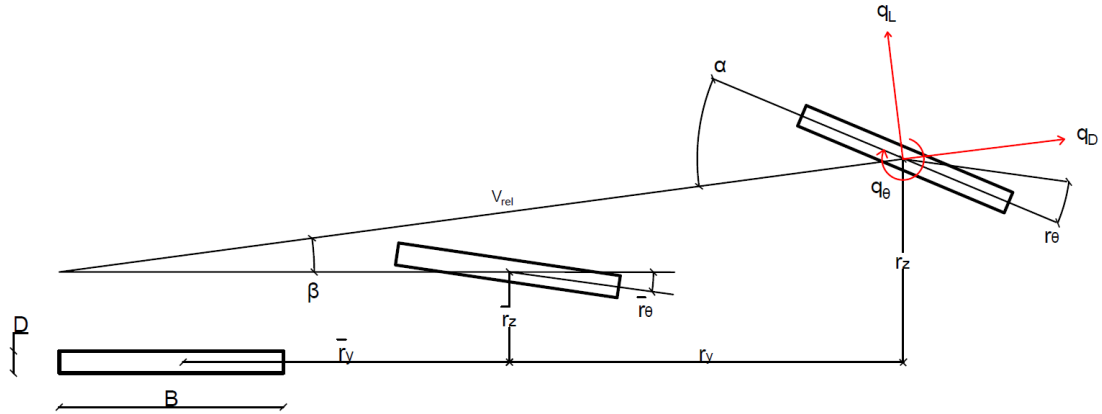


Figure 2.3: Illustration of a line-like structure exposed to buffeting load

The load coefficients are dependent on the angle of attack, α . It can be seen from Figure 2.3 that this can be expressed as

$$\alpha = \bar{r}_\theta + r_\theta + \beta \approx \bar{r}_\theta + r_\theta + \frac{w(x, t) - \dot{r}_z(x, t)}{\bar{V}} \quad (2.29)$$

The load coefficients are most often non-linear with respect to α . However, for small angle variations, a linearization around the mean angle gives a fair approximation [12]. The load coefficients can then be expressed as

$$\begin{bmatrix} C_D(\alpha) \\ C_L(\alpha) \\ C_M(\alpha) \end{bmatrix} = \begin{bmatrix} C_D(\bar{\alpha}) \\ C_L(\bar{\alpha}) \\ C_M(\bar{\alpha}) \end{bmatrix} + \alpha_f \begin{bmatrix} C'_D(\bar{\alpha}) \\ C'_L(\bar{\alpha}) \\ C'_M(\bar{\alpha}) \end{bmatrix} \quad (2.30)$$

Denoting

$$\begin{bmatrix} C_D(\bar{\alpha}) \\ C_L(\bar{\alpha}) \\ C_M(\bar{\alpha}) \end{bmatrix} = \begin{bmatrix} \bar{C}_D \\ \bar{C}_L \\ \bar{C}_M \end{bmatrix} \quad (2.31) \quad \begin{bmatrix} C'_D(\bar{\alpha}) \\ C'_L(\bar{\alpha}) \\ C'_M(\bar{\alpha}) \end{bmatrix} = \begin{bmatrix} C'_D \\ C'_L \\ C'_M \end{bmatrix} \quad (2.32)$$

Combining this with Equation (2.34) and (2.26), and utilizing the simplification done in Equation (2.27) the expression for the total load on the line-like structure is obtained [12].

$$\begin{bmatrix} q_y \\ q_z \\ q_\theta \end{bmatrix} = \rho \bar{V} \left(\frac{\bar{V}}{2} + u - \dot{r}_y \right) \begin{bmatrix} D\bar{C}_D \\ B\bar{C}_L \\ B^2\bar{C}_M \end{bmatrix} + \left(r_\theta + \frac{w - \dot{r}_z}{\bar{V}} \right) \begin{bmatrix} DC'_D \\ BC'_L \\ B^2C'_M \end{bmatrix} + \frac{w - \dot{r}_z}{\bar{V}} \begin{bmatrix} -B\bar{C}_L \\ D\bar{C}_D \\ 0 \end{bmatrix} \quad (2.33)$$

This expression consists of static terms, turbulence dependent terms and motion induced terms [12]. With some sorting, this can be simplified to

$$\mathbf{q}_{tot}(x, t) = \bar{\mathbf{q}}(x) + \mathbf{B}_q \mathbf{v}(x, t) + \mathbf{C}_{ae} \dot{\mathbf{r}}(x, t) + \mathbf{K}_{ae} \mathbf{r}(x, t) \quad (2.34)$$

where

$$\mathbf{v}(x, t) = [u \quad w]^T \quad (2.35) \quad \mathbf{r}(x, t) = [r_y \quad r_z \quad r_\theta]^T \quad (2.36)$$

and

$$\mathbf{B}_q = \frac{\rho \bar{V} B}{2} \begin{bmatrix} 2(D/B)\bar{C}_D & ((D/B)C'_D - \bar{C}_L) \\ 2\bar{C}_L & (C'_L + (D/B)\bar{C}_D) \\ 2B\bar{C}_M & B\bar{C}_M \end{bmatrix} \quad (2.37)$$

$$\mathbf{C}_{ae}(x) = -\frac{\rho \bar{V} B}{2} \begin{bmatrix} 2(D/B)\bar{C}_D & ((D/B)C'_D - \bar{C}_L) & 0 \\ 2\bar{C}_L & (C'_L + (D/B)\bar{C}_D) & 0 \\ 2B\bar{C}_M & B\bar{C}'_M & 0 \end{bmatrix} \quad (2.38)$$

$$\mathbf{K}_{ae}(x) = \frac{\rho \bar{V}^2 B}{2} \begin{bmatrix} 0 & 0 & (D/B)C'_D \\ 0 & 0 & C'_L \\ 0 & 0 & B\bar{C}'_M \end{bmatrix} \quad (2.39)$$

Here, \mathbf{C}_{ae} and \mathbf{K}_{ae} are denoted as aerodynamic damping and stiffness, respectively. Analogous to structural damping and stiffness, these are proportional to the structural velocity and displacement. Including these terms, the FRF in Equation (2.11) may now be expanded to

$$\mathbf{H}(\omega) = [-\omega^2 \mathbf{M} + i\omega(\mathbf{C} - \mathbf{C}_{ae}) + (\mathbf{K} - \mathbf{K}_{ae})]^{-1} \quad (2.40)$$

This illustrates that the structural properties are changed in the presence of fluctuating wind.

2.4.2 Aerodynamic derivatives

By Fourier transforming Equation (2.34), the buffeting theory can also be applicable in frequency domain analysis [12]. The transformation introduces a frequency dependency of the content in \mathbf{C}_{ae} and \mathbf{K}_{ae} , which in fact improves the representation, while the buffeting theory only represents a quasi-static case. The content of \mathbf{C}_{ae} and \mathbf{K}_{ae} is now replaced with the so-called aerodynamic derivatives. These are coefficients that are dependent on the frequency of motion, the mean wind velocity and the cross-section geometry.

$$\mathbf{C}_{ae} = \begin{bmatrix} P_1 & P_5 & P_2 \\ H_5 & H_1 & H_2 \\ A_5 & A_1 & A_2 \end{bmatrix} \quad (2.41) \quad \mathbf{K}_{ae} = \begin{bmatrix} P_4 & P_6 & P_3 \\ H_6 & H_4 & H_3 \\ A_6 & A_4 & A_3 \end{bmatrix} \quad (2.42)$$

The coefficients are most often experimentally determined in wind tunnel testing of scaled cross-section models [12]. The coefficients may be normalized by introducing

$$\mathbf{C}_{ae} = \frac{\rho B^2}{2} \omega_n(\bar{V}) \cdot \hat{\mathbf{C}}_{ae} \quad (2.43)$$

$$\mathbf{K}_{ae} = \frac{\rho B^2}{2} [\omega_n(\bar{V})]^2 \cdot \hat{\mathbf{K}}_{ae} \quad (2.44)$$

where ω_n is the resonance frequency corresponding to mode n and $\hat{\mathbf{C}}_{ae}$ and $\hat{\mathbf{K}}_{ae}$ are the non-dimensional coefficients

$$\hat{\mathbf{C}}_{ae} = \begin{bmatrix} P_1^* & P_5^* & BP_2^* \\ H_5^* & H_1^* & BH_2^* \\ BA_5^* & BA_1^* & B^2A_2^* \end{bmatrix} \quad (2.45)$$

$$\hat{\mathbf{K}}_{ae} = \begin{bmatrix} P_4^* & P_6^* & BP_3^* \\ H_6^* & H_4^* & BH_3^* \\ BA_6^* & BA_4^* & B^2A_3^* \end{bmatrix} \quad (2.46)$$

Their relation to the buffeting theory can be seen by

$$\begin{bmatrix} P_1^* & H_1^* & A_1^* \\ P_2^* & H_2^* & A_2^* \\ P_3^* & H_3^* & A_3^* \\ P_4^* & H_4^* & A_4^* \\ P_5^* & H_5^* & A_5^* \\ P_6^* & H_6^* & A_6^* \end{bmatrix} = \begin{bmatrix} -2\bar{C}_D \frac{D}{B} \left(\frac{\bar{V}}{B\omega_n(\bar{V})}\right) & -(C'_L + C_D \frac{D}{B}) \left(\frac{\bar{V}}{B\omega_n(\bar{V})}\right) & -C'_M \left(\frac{\bar{V}}{B\omega_n(\bar{V})}\right) \\ 0 & 0 & 0 \\ C'_D \frac{D}{B} \left(\frac{\bar{V}}{B\omega_n(\bar{V})}\right)^2 & C'_L \left(\frac{\bar{V}}{B\omega_n(\bar{V})}\right)^2 & C'_M \left(\frac{\bar{V}}{B\omega_n(\bar{V})}\right)^2 \\ 0 & 0 & 0 \\ (\bar{C}_L - C'_D \frac{D}{B}) \left(\frac{\bar{V}}{B\omega_n(\bar{V})}\right) & -2\bar{C}_L \left(\frac{\bar{V}}{B\omega_n(\bar{V})}\right) & -2\bar{C}_M \left(\frac{\bar{V}}{B\omega_n(\bar{V})}\right) \\ 0 & 0 & 0 \end{bmatrix} \quad (2.47)$$

The term $\left(\frac{\bar{V}}{B\omega_n(\bar{V})}\right)$ is called the reduced wind velocity, V_{red} , and $K = V_{red}^{-1}$ is the reduced frequency of motion [13]. The self-excited forces in the DOFs can then be expressed as

$$q_y^{Se} = \frac{1}{2} \rho \bar{V}^{-2} B (KP_1^* \frac{\dot{r}_y}{V} + KP_2^* \frac{B\dot{r}_\theta}{V} + K^2 P_3^* r_\theta + K^2 P_4^* \frac{r_y}{B} + KP_5^* \frac{\dot{r}_z}{V} + K^2 P_6^* \frac{r_z}{B}) \quad (2.48)$$

$$q_z^{Se} = \frac{1}{2} \rho \bar{V}^{-2} B (KH_1^* \frac{\dot{r}_z}{V} + KH_2^* \frac{B\dot{r}_\theta}{V} + K^2 H_3^* r_\theta + K^2 H_4^* \frac{r_z}{B} + KH_5^* \frac{\dot{r}_y}{V} + K^2 H_6^* \frac{r_y}{B}) \quad (2.49)$$

$$q_\theta^{Se} = \frac{1}{2} \rho \bar{V}^{-2} B^2 (KA_1^* \frac{\dot{r}_z}{V} + KA_2^* \frac{B\dot{r}_\theta}{V} + K^2 A_3^* r_\theta + K^2 A_4^* \frac{r_z}{B} + KA_5^* \frac{\dot{r}_y}{V} + K^2 A_6^* \frac{r_y}{B}) \quad (2.50)$$

By recording the self-excited forces for a defined motion at a certain wind velocity, the AD coefficients can be determined by minimizing the sum of squares [13]. By running the forced vibration test at different frequencies of motion, a curve for the AD coefficients can be fitted to a plot against frequency.

2.4.3 Vortex shedding

When an airflow meets a line-like structure, the flow will separate and vortices will be created as the airflow is released behind the structure section [12]. This vortex shedding appears to alternate on each side of the structure section, which again gives rise to alternating vertical

forces, q_z on the structure. As the forces normally have an eccentricity with regards to the cross-section center, the forces also generate an alternating pitching moment, q_θ . These forces can cause displacement and rotation, which again affects the motion induced forces presented in the earlier chapters. However, the vortex induced vibrations (VIV) are mainly significant only in the case of resonance with an eigenfrequency for the particular structure.

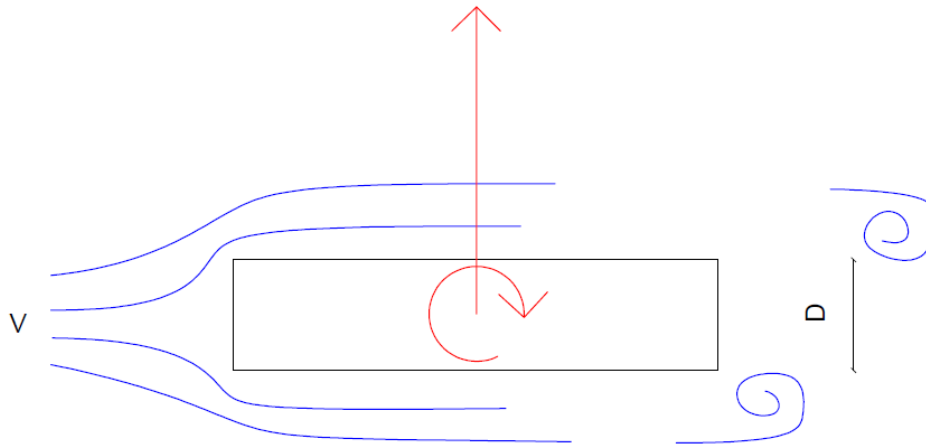


Figure 2.4: An illustration of how vortex shedding appears on the cross-section of a line-like structure

The pattern of the flow separation and thus, vortex shedding is characteristic to the cross-section of the line-like structure [12]. The typical frequency of the alternating forces can be calculated as

$$f_s = St \cdot \frac{\bar{V}}{D} \quad (2.51)$$

where \bar{V} is the mean wind velocity and D is the cross-section height. St is the so-called Strouhal number, which is characteristic for the cross-section. The alternating forces appear as a narrow-banded process around this wind velocity dependent frequency. In the case of a bridge girder as the line-like structure, the load appears to be more or less randomly distributed in the span direction.

As can be seen from Equation (2.51), the frequency of the load induced by vortex shedding is assumed to be proportional to the mean wind velocity [12]. Increasing the mean wind from zero, the frequency of shedding will coincide with the natural frequencies of the structure, mode by mode. Experiments also show that the structure can get caught in a resonant state for wind velocities well above the theoretical resonance shedding frequency. This is called lock-in, and has some unfavourable effects on the structure. Firstly, it can result in a higher correlation of the vortex shedding load in the span-wise direction. Secondly, the motion resulting from the vortex shedding load can induce additional unfavourable load. These effects are, however, self destructive from a certain limit of displacements, such that the structure does not become unstable. To prevent fatal consequences from vortex shedding, structural damping is effective in the sense of reducing the motion.

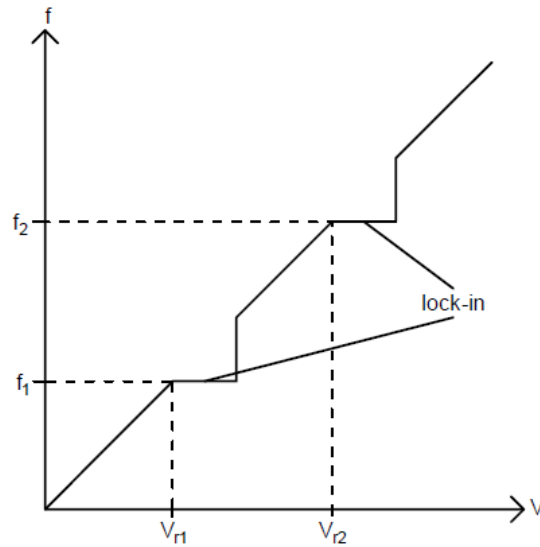


Figure 2.5: A plot of the vortex shedding frequency in interaction with a structural system

2.5 Motion induced instabilities

Structural instability is defined as a condition where a minor increase in loading results in a rapid increase in response [12]. For long span suspension bridges, it is common to differentiate between four different types of unstable behavior:

- Static divergence
- Galloping
- Dynamic instability in torsion
- Flutter (bi- and multi-modal)

The lowest mean wind speed at which one of these behaviors arises is referred to as the critical wind speed V_{cr} . The critical wind speed marks the stability limit and can be found by studying the components of the impedance matrix. The impedance matrix is defined as the inverse of the frequency response matrix defined in Equation (2.40), and is expressed as

$$\hat{\mathbf{E}}_{\eta}(\omega, V) = \hat{\mathbf{H}}_{\eta}(\omega, V)^{-1} = \mathbf{I} - \kappa_{ae} - \left(\omega \cdot \begin{bmatrix} \frac{1}{\omega_i} & & \\ & \ddots & \\ & & \frac{1}{\omega_i} \end{bmatrix} \right)^2 + 2i\omega \cdot \begin{bmatrix} \frac{1}{\omega_i} & & \\ & \ddots & \\ & & \frac{1}{\omega_i} \end{bmatrix} \cdot (\zeta - \zeta_{ae}) \quad (2.52)$$

The normalized modal quantities of aerodynamic stiffness and damping, κ_{ae} and ζ_{ae} , are the components that cause the unstable behavior. \mathbf{I} is the identity matrix and ζ is a diagonal

matrix containing structural damping ratios [12]. The entries of κ_{ae} and ζ_{ae} are defined as

$$\kappa_{aeij} = \frac{\tilde{K}_{aeij}}{\omega_i^2 \tilde{M}_i} = \frac{\rho B^2}{2\tilde{m}_i} \cdot \left[\frac{\omega_i(V)}{\omega_i} \right]^2 \cdot \frac{\int_{L_{exp}} (\varphi_i^T \cdot \tilde{\mathbf{K}}_{ae} \cdot \varphi_j) dx}{\int_L (\varphi_i^T \cdot \varphi_i) dx} \quad (2.53)$$

$$\zeta_{aeij} = \frac{\omega_i \tilde{C}_{aeij}}{2\omega_i^2 \tilde{M}_i} = \frac{\rho B^2}{4\tilde{m}_i} \cdot \frac{\omega_i(V)}{\omega_i} \cdot \frac{\int_{L_{exp}} (\varphi_i^T \cdot \tilde{\mathbf{C}}_{ae} \cdot \varphi_j) dx}{\int_L (\varphi_i^T \cdot \varphi_i) dx} \quad (2.54)$$

where $\omega_i(V)$ is the mean wind frequency associated with mode i . $\omega_i = \omega_i(V=0)$ is the still-wind frequency. The stability limit is determined when the determinant of Equation (2.52) reaches zero. This condition is defined in Equation (2.55), and will theoretically yield an infinite response in the system. Since the impedance matrix is complex, the conditions in Equation (2.56) and (2.57) have to be fulfilled.

$$|\det(\hat{\mathbf{E}}_\eta(\omega, V))| = 0 \quad (2.55)$$

$$Re(\det(\hat{\mathbf{E}})) = 0 \quad (2.56) \quad Im(\det(\hat{\mathbf{E}})) = 0 \quad (2.57)$$

The eigenvalue problem has N_{modes} roots [12]. Each root consist a pair of ω and V , and represents a stability limit for its corresponding mode shape, φ_i . However, its the root that yields the lowest mean wind speed that marks the stability limit, and that will be referred to as the critical wind speed V_{cr} , which is associated with the resonance frequency ω_r .

For suspension bridges, the girder is most prone to motion induced instabilities and thus the unstable behaviours listed in the start of this chapter [12]. The convention for the response quantities, $\mathbf{r}(x, t) = [r_y, r_z, r_\theta]$, described throughout this chapter is according to Figure 2.2.

2.5.1 Static divergence

Static divergence is a instability behavior in pure torsion [12]. When the mean wind frequency $\omega_\theta(V) = 0$, the problem is static and occurs when the system suddenly loses stiffness in the torsional direction due to the effect of wind flow. Implementing the torsional mode shape

$$\varphi_\theta = [0, 0, \varphi_\theta]^T \quad (2.58)$$

into Equation (2.52) the impedance matrix is reduced to

$$\hat{\mathbf{E}}_\eta(\omega_\theta(V) = 0, V_{cr}) = 1 - \kappa_{ae\theta\theta} \quad (2.59)$$

where its seen that the system goes unstable when $\kappa_{ae\theta\theta} = 1$. The normalized aerodynamic stiffness term is defined as

$$\kappa_{ae\theta\theta} = \frac{\rho B^4}{2\tilde{m}_\theta} \left[\frac{\omega_\theta(V)}{\omega_\theta} \right]^2 A_3^* \frac{\int_{L_{exp}} \varphi_\theta^2 dx}{\int_L \varphi_\theta^2 dx} \quad (2.60)$$

and can then be used to obtain the critical mean wind velocity for static divergence

$$V_{cr} = B \cdot \omega_\theta \left(\frac{2\tilde{m}_\theta}{\rho B^4 \dot{C}_M} \cdot \frac{\int_L \varphi_\theta^2 dx}{\int_{L_{exp}} \varphi_\theta^2 dx} \right)^{1/2} \quad (2.61)$$

2.5.2 Galloping

Galloping is a dynamic unstable behavior in which the bridge girder is put into oscillating vertical motion [12]. The mode shape for galloping is defined as

$$\varphi_z = [0, \varphi_z, 0]^T \quad (2.62)$$

which contain only the vertical component with the corresponding frequency $\omega_z(V)$. Due to the isolated motion, Equation (2.52) is reduced to

$$\hat{\mathbf{E}}_\eta(\omega_z(V), V_{cr}) = 1 - \kappa_{ae_{zz}} - (\omega_z(V)/\omega_z)^2 + 2i(\zeta_z - \zeta_{ae_{zz}})(\omega_z(V)/\omega_z) \quad (2.63)$$

whereas the aerodynamic stiffness and damping terms are given as

$$\kappa_{ae_{zz}} = \frac{\rho B^2}{2\tilde{m}_z} \left[\frac{\omega_z(V)}{\omega_z} \right]^2 H_4^* \frac{\int_{L_{exp}} \varphi_z^2 dx}{\int_L \varphi_z^2 dx} \quad (2.64)$$

$$\zeta_{ae_{zz}} = \frac{\rho B^2}{4\tilde{m}_z} \frac{\omega_z(V)}{\omega_z} H_1^* \frac{\int_{L_{exp}} \varphi_z^2 dx}{\int_L \varphi_z^2 dx} \quad (2.65)$$

Furthermore, the stability limit can be found by setting both the real and imaginary part of Equation (2.63) equal to zero [12]. Using the values for the aerodynamic derivatives presented in Equation (2.47) where H_4^* is equal to zero, we see that galloping can only occur if H_1^* is positive. The quasi-static critical wind speed can then be obtained by

$$V_{cr} = B\omega_z \left(\frac{\zeta_z}{-(\dot{C}_L + \bar{C}_D \cdot D/B) \rho B^2 \int_{L_{exp}} \varphi_z^2 dx} \frac{4\tilde{m}_z \int_L \varphi_z^2 dx}{\int_{L_{exp}} \varphi_z^2 dx} \right) \quad (2.66)$$

2.5.3 Dynamic instability in torsion

Like galloping, dynamic instability in torsion is dominated by a SDOF-motion. The mode shape is defined in Equation (2.58) and have the the associated frequency $\omega_\theta(V)$ [12]. Again, the impedance matrix is reduced to

$$\hat{\mathbf{E}}_\eta(\omega_\theta(V), V_{cr}) = 1 - \kappa_{ae_{\theta\theta}} - (\omega_\theta(V)/\omega_\theta)^2 + 2i(\zeta_\theta - \zeta_{ae_{\theta\theta}})(\omega_\theta(V)/\omega_\theta) \quad (2.67)$$

whereas the aerodynamic stiffness and damping terms are given as

$$\kappa_{ae_{\theta\theta}} = \frac{\rho B^4}{2\tilde{m}_\theta} \left[\frac{\omega_\theta(V)}{\omega_\theta} \right]^2 A_3^* \frac{\int_{L_{exp}} \varphi_\theta^2 dx}{\int_L \varphi_\theta^2 dx} \quad (2.68)$$

$$\zeta_{ae_{\theta\theta}} = \frac{\rho B^4}{4\tilde{m}_\theta} \frac{\omega_\theta(V)}{\omega_\theta} A_2^* \frac{\int_{L_{exp}} \varphi_\theta^2 dx}{\int_L \varphi_\theta^2 dx} \quad (2.69)$$

Evaluating Equation (2.67), it is then seen that dynamic instability in torsion can only occur if A_2^* is positive. Since Equation (2.47) yield zero value for A_2^* , quasi-static theory cannot be applied to obtain the stability limit.

2.5.4 Multi-modal flutter

Flutter is an instability phenomenon where two or more modes with different motion components couple and acts simultaneously [12][14]. Due to the fact that flutter is most likely to occur with r_z and r_θ , one can simplify calculations by excluding the horizontal component in a so-called two-DOF analysis. However, with the ever-increasing computational power, there is little reason not to include the horizontal component and perform multi-DOF analyses. The additional horizontal contribution may both have stabilizing and destabilizing effect on the aerodynamic stability, depending on how the coupling occurs. The multi-DOF approach is considered to have a slightly more accurate prediction of the critical wind speed than the two-DOF approach. For multi-modal flutter analysis, all modeshapes are assumed to have motion consisting of three components, and the notation now reads

$$\boldsymbol{\phi}_i = [\phi_y, \phi_z, \phi_\theta] \quad (2.70)$$

Coupling is only possible for shape-wise similar modes, and happens through the off-diagonal terms in the aerodynamic stiffness and damping matrices, which entries are defined on modal form in Equation (2.71) and (2.72), respectively [15]. For simplicity, it is now assumed that $L \approx L_{exp}$.

$$\tilde{\mathbf{K}}_{aeij} = \frac{\rho B^2}{2} \left[\frac{\omega_i(V)}{\omega_i} \right]^2 \int_L \left(\boldsymbol{\phi}_i \begin{bmatrix} P_4^* & P_6^* & BP_3^* \\ H_6^* & H_4^* & BH_3^* \\ BA_6^* & BA_4^* & B^2A_3^* \end{bmatrix} \boldsymbol{\phi}_j^T \right) dx \quad (2.71)$$

$$\tilde{\mathbf{C}}_{aeij} = \frac{\rho B^2}{2} \left[\frac{\omega_i(V)}{\omega_i} \right] \int_L \left(\boldsymbol{\phi}_i \begin{bmatrix} P_1^* & P_5^* & BP_2^* \\ H_5^* & H_1^* & BH_2^* \\ BA_5^* & BA_1^* & B^2A_2^* \end{bmatrix} \boldsymbol{\phi}_j^T \right) dx \quad (2.72)$$

The eigenvalue problem can then be assembled to calculate the critical wind speed [14]. Due to non-linearity introduced by the aerodynamic contributions described above, the process now demands iterations. This process is described in Section 2.5.5

2.5.5 Eigenvalue problem

The equation of motion with aerodynamic stiffness and damping contributions is defined on modal form as [14]

$$\tilde{\mathbf{M}}\ddot{\boldsymbol{\eta}} + (\tilde{\mathbf{C}} - \tilde{\mathbf{C}}_{ae}(\bar{V}))\dot{\boldsymbol{\eta}} + (\tilde{\mathbf{K}} - \tilde{\mathbf{K}}_{ae}(\bar{V}))\boldsymbol{\eta} = \mathbf{0} \quad (2.73)$$

Since damping is of great relevance in-wind, the damping terms cannot be neglected as one normally would do at this point. Assuming the homogeneous solution to be on the form $r = \boldsymbol{\psi}e^{\lambda t}$ and substituting this into Equation (2.73), the complex and quadratic eigenvalue problem is obtained as

$$(\lambda^2 \tilde{\mathbf{M}} + \lambda(\tilde{\mathbf{C}} - \tilde{\mathbf{C}}_{ae}(\bar{V})) + (\tilde{\mathbf{K}} - \tilde{\mathbf{K}}_{ae}(\bar{V})))\boldsymbol{\psi} = \mathbf{0} \quad (2.74)$$

where λ denotes the eigenvalues and $\boldsymbol{\psi}$ the corresponding eigenvectors. The non-linear effects are caused by the reduced velocity dependency in $\tilde{\mathbf{C}}_{ae}$ and $\tilde{\mathbf{K}}_{ae}$ [16][14]. There are several approaches to this problem, however this thesis will concentrate on state-space transformation followed by an iterative solving process. The state space transformation is convenient since it transforms the system from a second- to first-order system of differential equations. Disregarding the reduced frequency dependency, the state space transformation reads

$$\begin{bmatrix} \dot{\mathbf{r}} \\ \ddot{\mathbf{r}} \end{bmatrix} + \begin{bmatrix} \mathbf{0} & -\mathbf{I} \\ \tilde{\mathbf{M}}^{-1}(\tilde{\mathbf{K}} - \tilde{\mathbf{K}}_{ae}) & \tilde{\mathbf{M}}^{-1}(\tilde{\mathbf{C}} - \tilde{\mathbf{C}}_{ae}) \end{bmatrix} \begin{bmatrix} \mathbf{r} \\ \dot{\mathbf{r}} \end{bmatrix} = \begin{bmatrix} \mathbf{0} \\ \mathbf{0} \end{bmatrix} \quad (2.75)$$

\mathbf{I} is the identity matrix. In condensed form, the transformation can be written as

$$\dot{\mathbf{y}} + \mathbf{A}\mathbf{y} = \mathbf{0} \quad (2.76)$$

The eigenvalue problem now reads

$$(\mathbf{A} - \mathbf{I}\lambda)\boldsymbol{\psi} = \mathbf{0} \quad (2.77)$$

After the iterative solving, the complex eigenvalue for solution (mode) n of Equation (2.77) results in:

$$\lambda_n = \zeta_n \omega_n \pm i \omega_n \sqrt{1 - \zeta_n^2} \quad (2.78)$$

The in-wind frequency and in-wind damping ratio can then be extracted, and has the following relations

$$\omega_n = |\lambda_n| \quad (2.79) \quad \zeta_n = -\frac{\text{Re}(\lambda_n)}{|\lambda_n|} \quad (2.80)$$

As can be seen in Equation (2.80) the system loses damping and becomes unstable when $\text{Re}(\lambda_n) > 0$ [17]. This defines the theoretical stability limit. Figure 2.6 show how the system is affected by the result in eigenvalues.

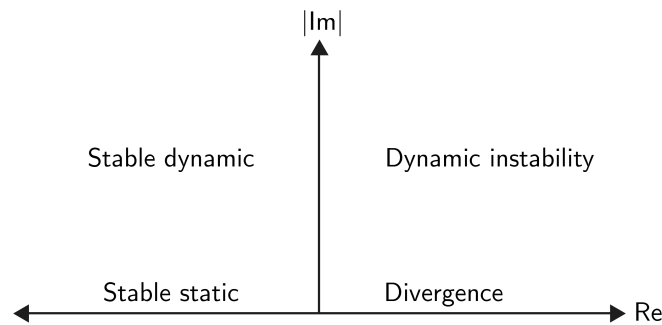


Figure 2.6: Illustration of how the system is affected by the change in eigenvalues

2.6 Gaussian Processes Regression

Regression models are used to predict the relationship between one or more variables and are a commonly used technique to derive forecasts in the medical, financial, and engineering industries [18]. The way its simplest form, linear regression, differs from interpolation is demonstrated in Figure 2.7

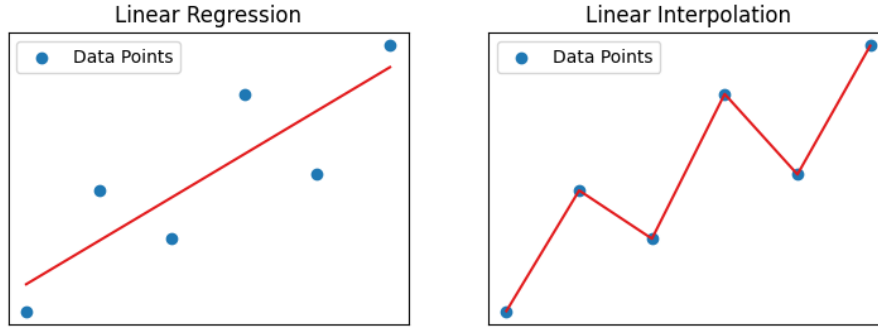


Figure 2.7: Illustration of the difference between linear regression and linear interpolation

The interpolation is required to pass through all points, whereas the main goal of a regression model is to be as close to all points as possible. The regression model therefore has to account for all the data points when obtaining the mean function. The way regression models process information about previous data points into their predictions is the reason why GPR is making its way into machine learning [18].

2.6.1 Gaussian Processes

Gaussian processes are distributions over functions and are fully defined by a mean function m and a positive definite covariance function k , commonly referred to as the kernel [19][18]. These functions are defined as

$$m(\mathbf{x}) = E[f(\mathbf{x})] \quad (2.81)$$

$$k(\mathbf{x}_i, \mathbf{x}_j) = E[(f(\mathbf{x}_i) - m(\mathbf{x}_i))(f(\mathbf{x}_j) - m(\mathbf{x}_j))] \quad (2.82)$$

Using the formulas above, the prior Gaussian distribution of $f(\mathbf{x})$ is defined

$$f(\mathbf{x}) \sim \mathcal{GP}(m(\mathbf{x}), k(\mathbf{x}_i, \mathbf{x}_j)) \quad (2.83)$$

A fundamental component of the Gaussian processes are multivariate Gaussian distributions [19]. Given a set of points $\mathbf{X} = [x_1, \dots, x_n]$, we can define its multivariate Gaussian distributions as

$$\mathbf{X} \sim \mathcal{N}_n(\boldsymbol{\mu}, \mathbf{K}) \quad (2.84)$$

where $\boldsymbol{\mu}$ is the n -dimensional mean vector

$$\boldsymbol{\mu} = E[\mathbf{X}] = [E[X_1], \dots, E[X_n]] \quad (2.85)$$

and \mathbf{K} is the $n \times n$ covariance matrix, with entries

$$K_{i,j} = E[(X_i - \mu_i)(X_j - \mu_j)] = \text{Cov}[X_i, X_j] \quad (2.86)$$

Normally, the multivariate Gaussian is limited to a finite number of jointly distributed Gaussian's, but since the covariance (kernel) of Gaussian processes is defined by a function, each input variable is correlated with the other variables in the input domain [19]. Hence, a Gaussian process can be thought of as an infinite dimensional Gaussian distribution.

2.6.2 Kernels

The kernel is a covariance function that describes the covariance of the Gaussian process random variables [20]. As mentioned above, the kernel together with the mean function fully defines the Gaussian process. A valid kernel function should be positive definite, which implies that the kernel matrix is symmetric and invertible. Typically, predefined kernels are used and selected based on knowledge of the collected data points.

Among the wide variety of kernels, the squared-exponential kernel (SE) is one of the most common and has the form [18][21]

$$k(x_i, x_j) = \exp\left(\frac{d(x_i, x_j)^2}{2l^2}\right) \quad (2.87)$$

where l is the characteristic length scale that determines the correlation distance between input points, and d is the Euclidean distance between input points x_i and x_j . The SE kernel is infinitely differentiable and thus very smooth. Stein (1999) argues that the SE kernel is too smooth and unrealistic for many physical processes [22]. Hence, the Matern kernel is recommended due to its smoothness parameter ν [23]. The Matern kernel is defined as

$$k(x_i, x_j) = \frac{1}{\Gamma(\nu)2^{\nu-1}} \left(\frac{\sqrt{2\nu}}{l}d(x_i, x_j)\right)^2 K_\nu\left(\frac{\sqrt{2\nu}}{l}d(x_i, x_j)\right) \quad (2.88)$$

where K_ν is a modified Bessel function and $\Gamma(\nu)$ is the gamma function. As ν decreases, the approximation becomes less smooth, and if $\nu \rightarrow \infty$, the Matern kernel becomes equivalent to the Squared-exponential kernel.

2.6.3 Regression predictions

For any regression, the goal is to model the function \mathbf{f} based on observed data points [18][19]. The prior distribution defined in Equation (2.83) represents all the possible outputs of \mathbf{f} , and is usually not interesting to sample from due to its infinite number of functions and hence large uncertainty. Updating the prior with the observed data points yields a joint distribution of the known values \mathbf{f} and the unknown values \mathbf{f}_* , defined as

$$\begin{bmatrix} \mathbf{f} \\ \mathbf{f}_* \end{bmatrix} \sim \mathcal{N}\left(\begin{bmatrix} m(\mathbf{X}) \\ m(\mathbf{X}_*) \end{bmatrix}, \begin{bmatrix} K(\mathbf{X}, \mathbf{X}) + \sigma_n^2 \mathbf{I} & K(\mathbf{X}, \mathbf{X}_*) \\ K(\mathbf{X}_*, \mathbf{X}) & K(\mathbf{X}_*, \mathbf{X}_*) \end{bmatrix}\right) \quad (2.89)$$

where $\sigma_n^2 \mathbf{I}$ is the noise variance for equally distributed Gaussian noise. When the observed data is implemented, the posterior distribution is derived from the conditional distribution over \mathbf{f}_* , resulting in

$$\mathbf{f}_* | \mathbf{X}, \mathbf{f}, \mathbf{X}_* \sim \mathcal{N}(\bar{\mathbf{f}}_*, \text{cov}(\mathbf{f}_*)) \quad (2.90)$$

where the predictive mean, $\bar{\mathbf{f}}_*$, and covariance matrix and $\text{cov}(\mathbf{f}_*)$ are defined as

$$\bar{\mathbf{f}}_* = K(\mathbf{X}_*, \mathbf{X})[K(\mathbf{X}, \mathbf{X}) + \sigma_n^2 \mathbf{I}]^{-1} \cdot \mathbf{f} \quad (2.91)$$

$$\text{cov}(\mathbf{f}_*) = K(\mathbf{X}_*, \mathbf{X}_*) - K(\mathbf{X}_*, \mathbf{X})[K(\mathbf{X}, \mathbf{X}) + \sigma_n^2 \mathbf{I}]^{-1} K(\mathbf{X}, \mathbf{X}_*) \quad (2.92)$$

The predicted mean drawn both from the prior and posterior distribution is shown in Figure 2.8, where the Matern kernel is used. The posterior distribution contains only the functions that fit the observed data points.

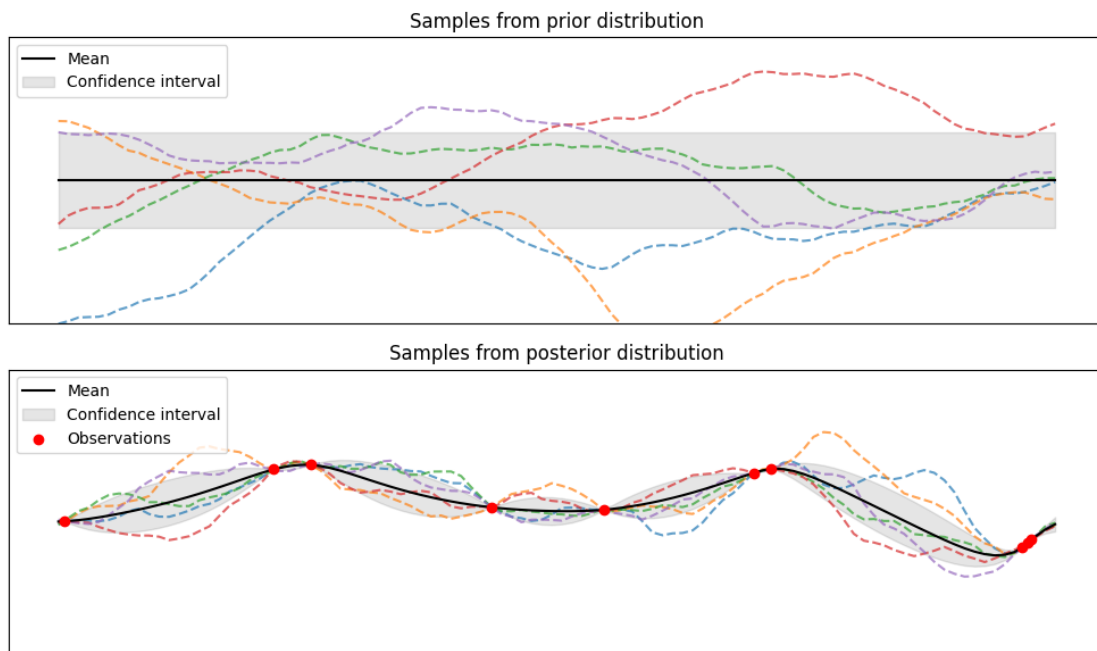


Figure 2.8: Illustration of the predicted mean drawn both from the prior and posterior distribution

2.7 Optimization

2.7.1 SciPy Optimize

The Python library Scientific Python (SciPy) offers modules for minimizing and maximizing objective functions [24]. `Scipy.minimize` is a commonly used function that enables minimizing scalar single or multivariate functions. The `minimize`-function includes several methods for approaching the minimum of the objective function, where one commonly used method, BFGS, can be mentioned. BFGS handles both linear and non-linear constraints, as well as bounds. The method uses a quasi-Newton approach to suggest new parameters, and may therefore be considered as a gradient-based method [25]. This means that it gains and utilizes information about the gradient (Jacobian matrix) and the curvature (Hessian matrix) of the objective function to approach its minimum. The method is, however, only able to locate local minimums. A remedy to obtain the global optimum could then be to run the algorithm over a space of initial guesses. However, this will further increase the number of iterations, which is a drawback for computationally expensive objective and constraint functions.

2.7.2 Bayesian Optimization

Bayesian Optimization is especially appropriate for costly objective functions, where lowering the number of iterations is a priority [26]. The method is based on creating and updating a surrogate model for the objective function, and may therefore be considered as a derivative-free method. While a surrogate model is created for the whole search space, the global optimum can be found. It handles multivariate problems, and is considered well-suited up to 20 dimensions. A drawback is the difficulty of implementing expensive-to-handle constraint functions.

The surrogate models are made by utilizing Gaussian Process Regression on a number of pre-samples [26]. The surrogate model is then improved iteration by iteration by adding samples to the regression. The sampling points are carefully chosen with an acquisition function to obtain the best possible surrogate model with, theoretically, as few iterations as possible. There are several types of acquisition functions, of which the Expected Improvement, denoted $EI(x_1, x_2, \dots, x_n)$, is one commonly used. This utilizes the fact that the GPR returns a confidence interval on the predicted objective function which can be seen from Figure 2.8. Where $\mu_f(x)$ is the mean value of the GPR over x , $\sigma_f(x)$ is the standard deviation of the GPR, the expected improvement is found by

$$EI(x) = \begin{cases} (\mu_f(x) - f(x^+) - \xi)\Phi(Z) + \sigma_f(x)\phi(Z) & \text{if } \sigma_f > 0 \\ 0 & \text{if } \sigma_f = 0 \end{cases} \quad (2.93)$$

$$Z = \frac{\mu_f(x) - f(x^+) - \xi}{\sigma_f(x)} \quad (2.94)$$

where $f(x^+)$ is the current objective function optimum, judged from the previous GPR, Φ and ϕ are the cumulative- and normal probability distributions, respectively. The parameter ξ weights how much the algorithm should prioritize to explore regions with high uncertainty. So basically, the algorithm will sample in areas where the surrogate model is promising or where the uncertainty is high. The expected improvement function is then a scalar function that can be maximized to find the next sampling point, with the use of i.e. the BFGS method. Figure 2.9 shows an example on how an expected improvement function is found from a GPR of samples. It illustrates how the algorithms seeks areas where the surrogate model is promising, but avoids the previous sampling points where the confidence interval is equal to zero.

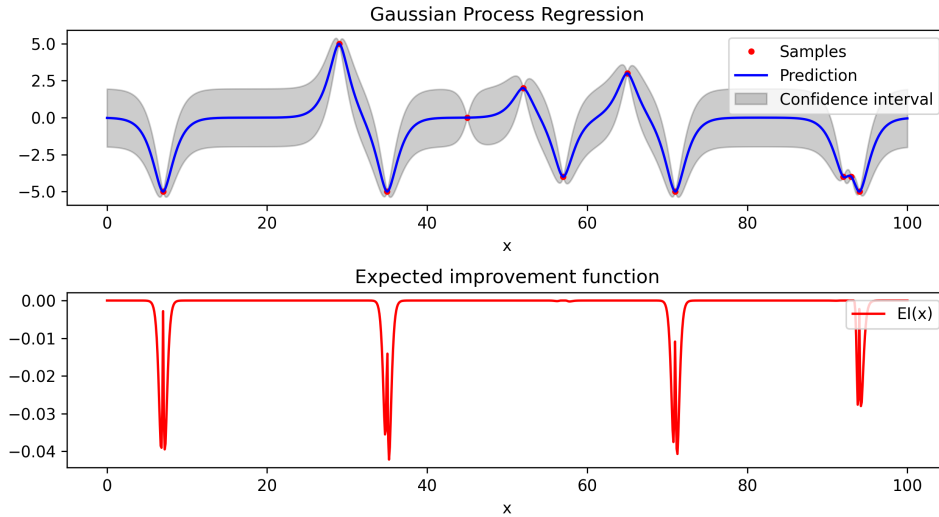


Figure 2.9: Plots showing one iteration of the Bayesian Optimization algorithm

Chapter 3

Methodology

3.1 General workflow

The general objective of this project was to develop a program that can be useful in choosing the optimal design when considering the aerodynamic stability of a suspension bridge. The program will initially be made for the Langenuen crossing as a case study, but should also be adaptable to other projects. This is done by running an optimisation function on a parametric study. The objective function that governs the optimisation algorithm is a material cost function. A requirement for the design is to overcome the design criterion for the critical wind speed at 76 m/s [27]. The aerodynamic stability limit is accessed by studying the interaction between modal properties and aerodynamic design. This is then regarded as a constraint in the optimisation function.

To simplify the process, it was decided to limit the parameter study to two main parameters. The tower height, together with the girder cross-section was regarded as the most important parameters for the aerodynamic properties and the total material use. The girder cross-section parametrisation was restrained to one parameter, namely the girder height, which was then the second main parameter in the optimisation. The main idea of the project was to develop a fully automatic and efficient optimisation program, that could be expanded to include additional parameters, constraints, and objectives.

The program was developed in a workspace in the code editor Visual Studio Code [28], using the programming language Python. The idea was to build it as a loop where the optimisation function generated appropriate input parameters for each iteration. Looping through a global modal analysis in Abaqus and surrogate models for AD-data, the critical wind speed could be calculated and controlled in the constraint function. Using the geometry generated with the input parameters, the material cost could also be calculated by multiplying the material quantities with price functions. The optimisation function then iterates to minimize the objective function, resulting in the assumed cheapest alternative. The initial idea of how to structure the optimisation is illustrated in Figure 3.1.

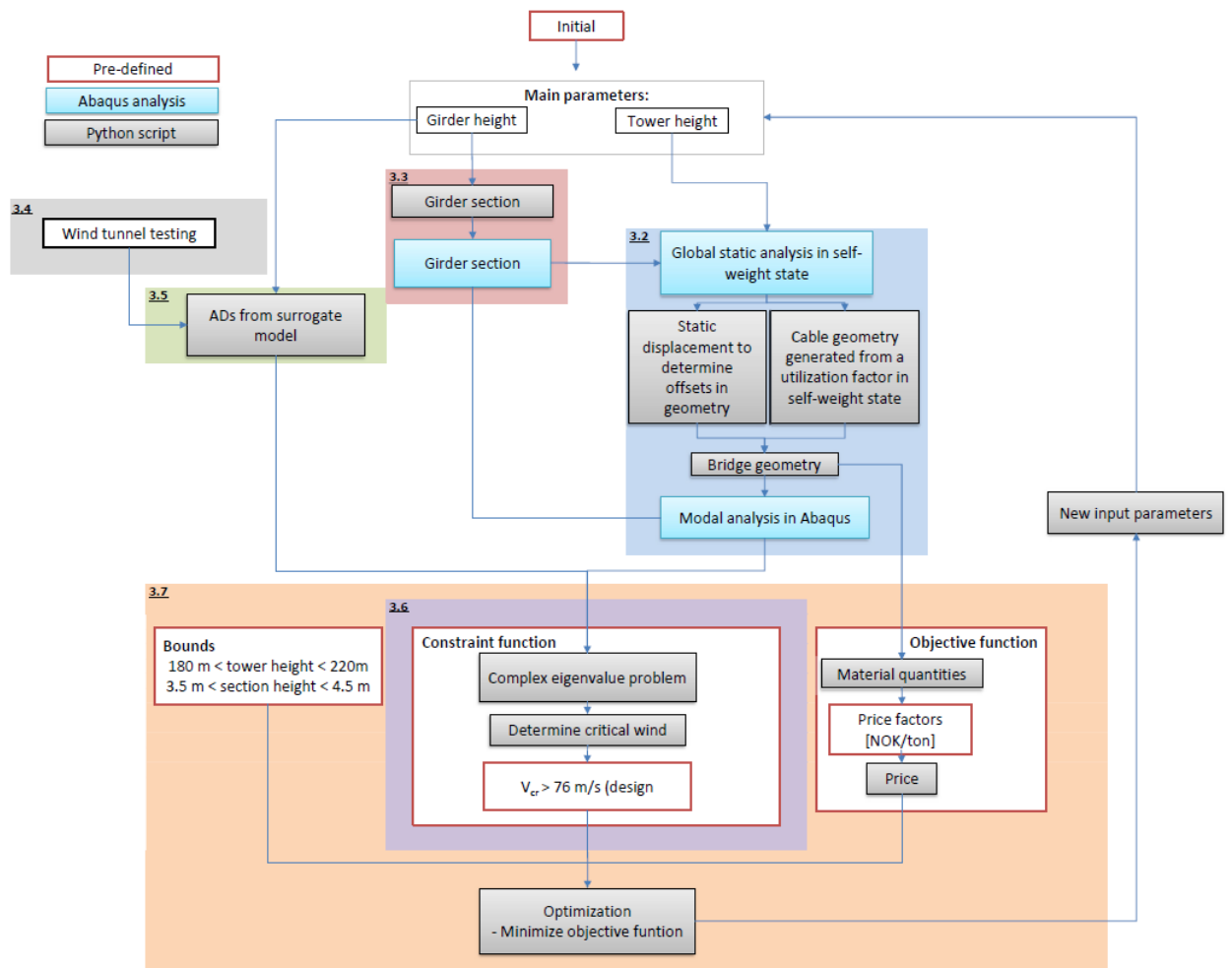


Figure 3.1: Flowchart illustrating the initial idea of the program. The section references indicates where each part is described.

It was desired to keep the program efficient in order to debug and improve it in a more practical manner. One could also imagine that expanding the program with additional parameters would make it even more time-demanding, so keeping the running time as low as possible was a priority. It was quickly identified that running Abaqus within the loop was the most time-demanding part of each iteration. Cross-section properties and statical displacement in the global model looked to behave quite linearly with respect to the two main parameters. It was then decided to carry out preliminary studies for a range of input parameters and save the results in csv-files. The optimisation loop was then made to extract cross-section parameters and geometry offsets using linear and bi-linear interpolation, respectively, on the csv-data. This is further explained in the following chapters. By using an interpolation approach on cross-section parameters as well as static displacement, the number of Abaqus analyses within each iteration of the optimization was reduced from three to one.

3.2 Global Abaqus model

The stability limit is dependent on the modal properties of the structure, and thus, a modal analysis had to be carried out for each iteration of the optimization loop. The program was therefore made to initiate the process of establishing an FE-model of the bridge based on the two main parameters, tower and girder height, and execute the modal analysis. Our supervisor, Øyvind Wiig Petersen has developed a parametric script for general suspension bridge models in Abaqus, which was very helpful in our work. This script takes key geometric parameters, distributes nodes and element, and writes this to an Abaqus INP-file. It also takes element type definitions and material parameters. Further, the script writes calculation steps, where it defines boundary conditions and assigns gravitational load. Lastly, an Abaqus job is submitted that generates an ODB-file, where the requested output can be read. This was very helpful to our work, and we are very grateful for Øyvinds work on this.

Through step definitions, the model is established in the same way as a suspension bridge is typically built in real life. The steps are illustrated in Figure 3.2. The steps 1-4 are static steps, where gravitational load is added along with the element establishment. Non-linear effects are accounted for, mainly to include the significant geometrical stiffness that occurs in the cables. Static equilibrium must then be found iteratively.

Step 1: Towers

- 2-node bi-linear beam elements (B31) [29]
- Element length of 5 meters. The last (top) element of each tower has a length of $Towerheight \equiv 5m$.
- Tower box cross section from $7.5 \times 7.5 \times 1.0m$ at tower base to $5.0 \times 4.0 \times 0.6m$ at tower top
- Tower legs are fixed at their base
- Tower leg spacing of 40.0 m at base and 3.0 m at top
- Crossbeam elements are defined at elevations $60m$ and $Towerheight - 1m$
- Crossbeam section of $6.0 \times 4.0 \times 0.6m$
- Pullback forces are assigned to the tower tops to compensate for the forces from the cables when the rest of the bridge self-weight is applied.

Step 2: Main cables

- 2-node cubic beam elements (B33) [29]
- The main cables has a parabolic shape defined from the elevation at the tower tops and the elevation at mid-span of 88.8 meters.
- The mesh discretization is defined from the hanger spacing, i.e 12 meters, and 50 elements in the side-spans.
- The cable anchors are defined with BC's, constraining translation as well as rotation around the x-axis. The cables are connected to the tower top nodes.
- The cables do also have a sideways parabolic shape. To maintain this when gravitational load is applied, 11 temporary supporting beam elements are placed between the cables. These are removed in the later steps.

Step 3: Girder and hanger

- Girder is 2-node bi-linear beam elements (B31) [29]
- The girder length (span length) is 1235 meters.
- The girder is defined with a so-called Beam General Section, such that the girder cross-section is not geometrically defined in the model, it is only assigned mass and stiffness properties.
- The girder has a parabolic shape defined by the elevation of 69 meters at its ends and an elevation of 76.6 meters at mid-span.
- Since the girder is modelled as a spine beam, connection elements are added to define the width of the bridgedeck.
- The hangers are single 2-node bi-linear beam elements (B31)[29].
- Connected to cable node at top and girder connection element at bottom

Step 4: Bearing elements

- Bearing elements are added to the lower tower crossbeam to model the girder boundary conditions more accurately.
- These are pendulums constraining rotation around the x-axis, as well as springs that connects the bridgedeck center to the crossbeam, restraining translations.
- The springs have stiffness $3e7, 1e12, 1e6$ N/m in the coordinate directions X,Y and Z, respectively.
- Plates are added to visualize the bridgedeck, however, these have no structural role.

Step 5: Modal analysis

- Requesting the 100 first eigenfrequencies, with corresponding mode shape vectors.
- Abaqus here uses the Lanczos method for eigenvalue extraction [29].

The material properties assigned to the elements are summed up in Table 3.1.

Table 3.1: Material properties used in the Abaqus model

Part	ρ [kg/m ³]	E [MPa]	ν	G [MPa]
Concrete towers	2500	35	0.2	14.6
Cable steel	7850	200	0.25	80
Girder aluminium	2700	70	0.35	26
Hanger steel	7850	160	0.33	60

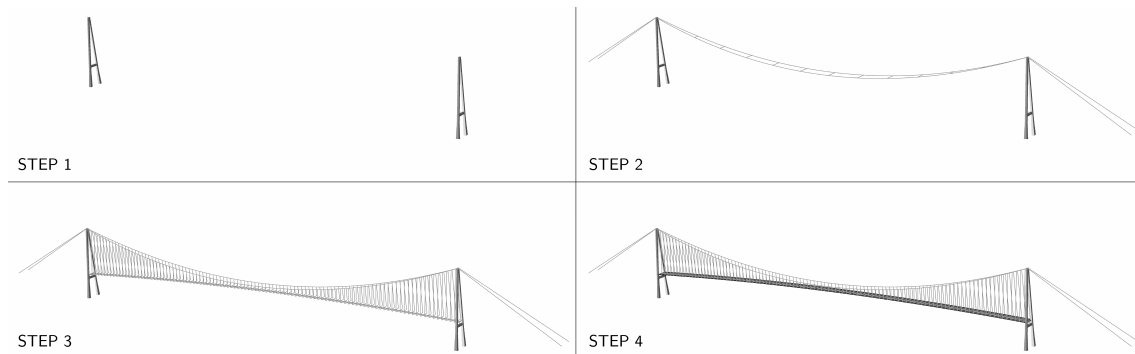


Figure 3.2: The steps illustrating the establishment of the global Abaqus model

The parameters that were set to generate the input for the model in our program are listed in Table 3.2. The tower height is, as mentioned in Section 3.1 one of the main parameters. The girder properties are functions of the girder height, which is calculated in a separate Abaqus analysis, described in the next chapter. The deflections as well as the maximum cable and hanger forces can be extracted from a static analysis in self-weight state. By setting a target maximum stress in the cables and hangers, the necessary section areas are calculated by utilizing the formula $\sigma_{max} = \frac{N_{max}}{A}$. The target stress in static self-weight state was set to 500 MPa for both the hanger and the main cable. This is in the upper range of what Dr. Techn. Olav Olsen have tested in their parametric study [27].

Static deflections and forces must be calculated in an iterative manner to get them correct. This because they are self-dependent and vary with the main parameters. This would require a separate analysis prior to the modal analysis, which would add another 30-60 seconds per iteration of the final optimization. It was discovered that the deflections and the cable and hanger forces had quite linear (bi-linear) behavior with respect to the main parameters. Therefore, a preliminary study was done, iterating through ranges of tower heights and girder heights, writing deflections and maximum forces to a csv-file. The input for each iteration was the result of the previous analysis of the most similar configuration, with tower height as the priority. In the modal analysis used in the optimization, deflections and max forces could be extracted by bi-linear interpolation of the content in the csv-file. This was considered to be sufficiently accurate as long as the steps in the ranges of input parameters for the static analysis were set small enough. The ranges were defined $h_t \in [180, 220]$ with steps of 5 m, and $h_g \in [3.5, 4.5]$ with steps of 0.25 m. Altogether, this means that all the parameters listed in Table 3.2 could be calculated as functions of the two main parameters. Parameters beyond the listed ones are kept constant through the optimization. Mostly, they are set equal to what has been used in previous studies on the Langenuen crossing.

Table 3.2: Variables in global Abaqus model

Parameter	Description
Tower height	Z-coordinate of top nodes
Girder cross-section area	Solid area of girder cross section
Girder second moment of inertia (I_{11})	Girder stiffness around weak axis (y)
Girder second moment of inertia (I_{22})	Girder stiffness around strong axis (z)
Girder torsional stiffness constant (I_t)	Stiffness towards roation around longitudinal axis (x)
Girder distributed mass	Mass per meter in longitudinal direction
Girder moment of inertia axis 11	Moment inertia around y-axis per meter x-direction
Girder moment of inertia axis 22	Moment inertia around z-axis per meter x-direction
Girder deflection (UZ) at midspan	Static self-weight deflection to define geometry offset
Girder deflection deflection (UZ) at south end	Static self-weight deflection to define geometry offset
Girder deflection (UZ) at north end	Static self-weight deflection to define geometry offset
Cable deflection (UZ) at midspan	Static self-weight deflection to define geometry offset
Tower deflection (UX) at top	Static self-weight deflection to define geometry offset
Max axial force in cables	Static self-weight force to calculate cable section area
Max axial force in hangers	Static self-weight force to calculate hanger section area

3.3 Cross-section parametrization

To approach the optimal solution for the Langenuen project, a range of cross-sections should be considered for the bridge girder. The choice of cross-section will determine the mass and stiffness properties of the girder and thus influence the modal properties of the bridge. Additionally, the shape will determine the wind flow around the girder and therefore its aerodynamic derivatives. The range of cross-sections included in the optimization must then be represented with wind-tunnel data, which becomes a time and cost consuming process as the range of cross-sections increases. It was therefore regarded as necessary to constrain some parameters in the girder parametrisation. All of the angles defining the cross-section shape were decided to be held constant. The bridge width is also constant at 31 meters, such that the girder height becomes the only variable in the cross-section parameterisation. Master projects from 2020 and 2021 have shown that the critical wind speed criteria can be met with cross-section heights as low as 4.9 meters, and that even lower cross-sections could be tested.

The transverse panel concept developed in a preliminary study by Dr. Techn. Olav Olsen is the concept further developed throughout this project [27]. Of the three different aluminium girder concepts that are suggested for the Langenuen crossing, the transverse panel concept is assumingly preferable due to its performance with regards to fatigue. In cooperation with NPRA, RWDI has done free vibration wind-tunnel tests on some cross-section types [30]. It was then interesting to include some of the same cross-section types in a forced vibration wind tunnel test, to get a good comparison of the methods, considering the resulting ADs. In consultation with our supervisors and Jungao Wang from NPRA, it was decided to go on with the LA12-16 section that has been tested by RWDI. This has a maximal height of 4.0 meters and an inclination of 16 degrees. In addition to this, cross-section heights of 3.5, 3.75, 4.25, and 4.5 meters with the same inclination angle were to be tested in the wind-tunnel in this project. Figure 3.3 shows the cross-sections that were to be tested in the wind-tunnel.

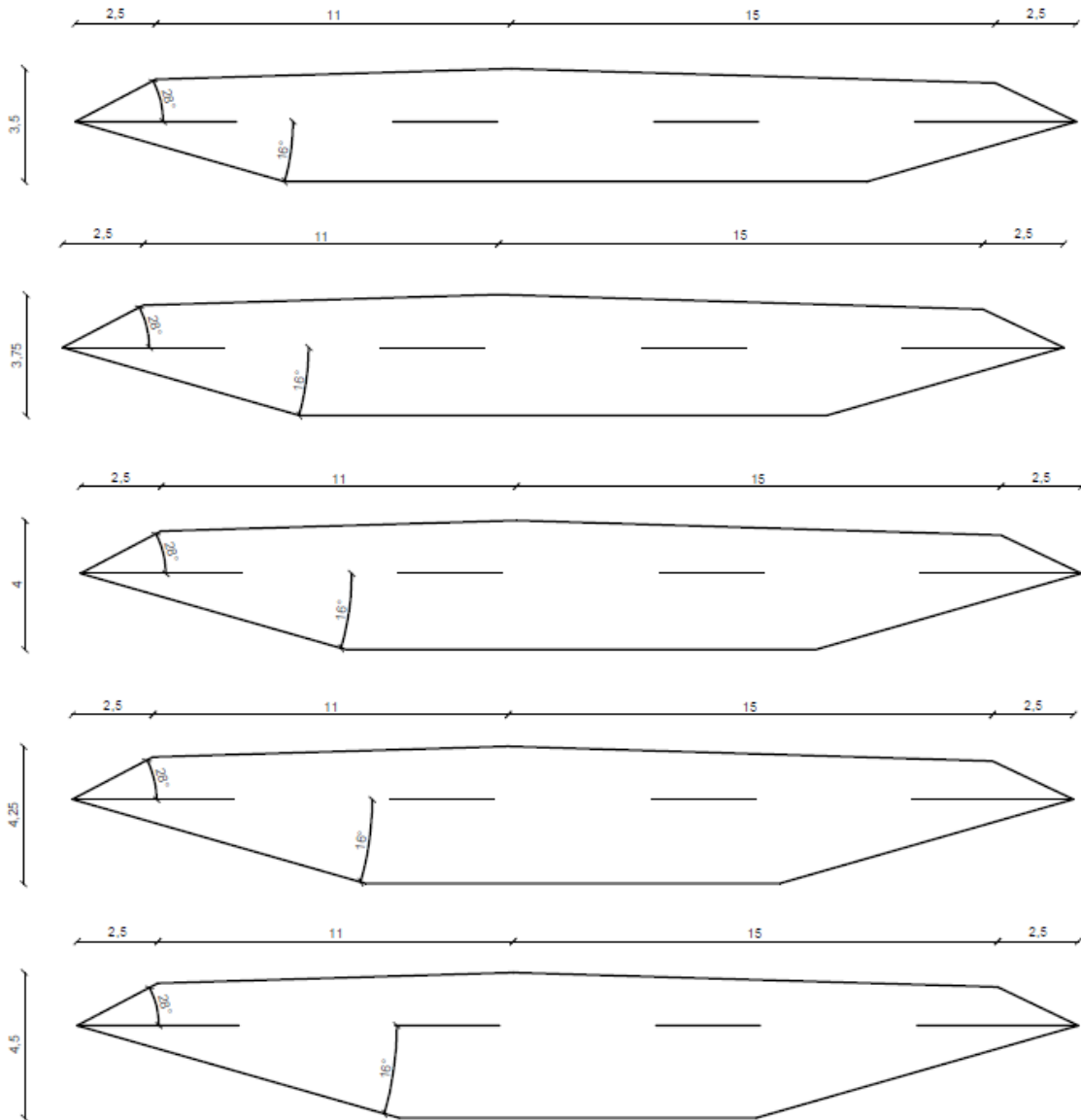


Figure 3.3: Illustrations of the cross-sections that are to be tested in the wind-tunnel

As can be seen from Figure 3.3, the cross-section is parameterized with height as the only varying parameter. To generate drawings of the cross-sections, a parametric script was developed in the software Autodesk Dynamo. From this script, the corner coordinates were defined for all the five cross-section shapes. The corner coordinates were saved to an excel sheet that was used to mill the section models with a CNC-machine. In addition to this, a parametric Python script was written to define the geometry that would be analyzed in Abaqus to generate the cross-section parameters.

The transverse panel concept consists of extruded aluminium panels that are friction stir welded together [27]. The panels are designed as illustrated in Figure 3.4, in order to prevent local plate buckling. The panels are compiled as illustrated in Figure 3.5, with the panels directed transverse to the girder span direction. Bulkhead panels are placed every 3.9 meters in the

longitudinal direction, assembled by panels directed vertically. Although the transverse panel concept has been shown to be beneficial with regard to fatigue, it complicates the calculation of the cross-section parameters, because the panels do not have a constant cross-section in the longitudinal direction. Therefore, some simplifications are made to prevent the cross-section analysis from taking too much time away from the actual scope of this project.

The main simplification is to represent the panels as massive plates, with a constant effective thickness. The calculation of the effective thickness is based on the properties that Dr. Techn. Olav Olsen has calculated for their version of a transverse panel cross-section. They have investigated a cross-section with a height of 5.5 meters and an inclination of 31.41 deg [27]. With an effective thickness of 35 mm, the torsional stiffness was calculated to 40.6 m^4 , utilizing Bredt's 2. formula for St. Venant torsion.

$$I_t = \frac{4A_m^2}{\oint \frac{ds}{t}} \quad (3.1)$$

The same effective thickness of 35 mm was used in the cross-section parametrisation, assuming that this was representative for the transverse panel concept.

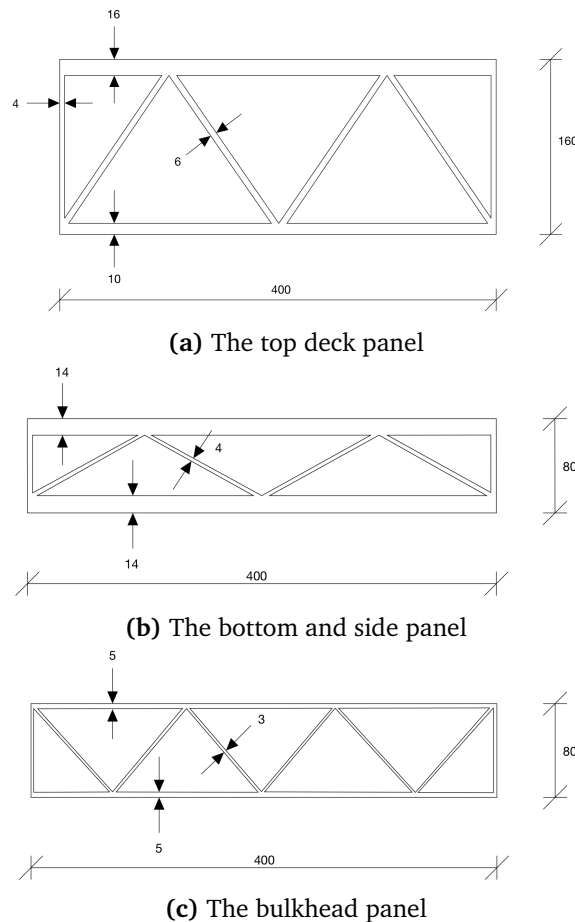


Figure 3.4: Illustrations of the geometries of the panels used in the transverse panel concept

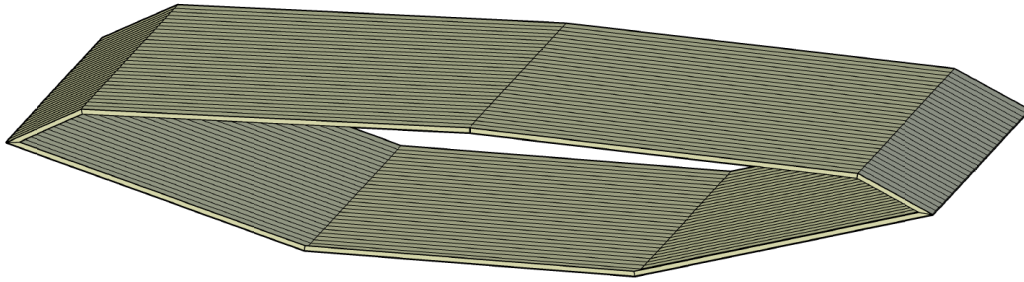


Figure 3.5: Illustration of the transverse panel concept developed by Dr. Techn Olav Olsen for NPRA. Bulkheads are not shown.

As was mentioned in Section 3.2, the girder in the Abaqus model is represented by a spine beam, only described by its mass and stiffness properties and not by its geometry. To run the global model with girder height as an input parameter, a separate process had to calculate the mass and stiffness properties for the girder geometry, determined by the girder height parameter. The analysis of the different sections was carried out using plates with thickness 35 mm. The girder shapes in Figure 3.3 represents the mid-lines, which were then offset 17.5 mm in and out to create a locked thin-walled cross-section sketch. This was sent to Abaqus to generate the section properties. Abaqus generated a mesh of WARP2D4 and WARP2D3 elements, which are 2D planar quadrilateral and triangular elements, respectively. These elements each have one DOF that represent the value of the warping function, which enables the calculation of the total torsional stiffness, as well as other stiffness, mass and inertia parameters [31]. A simple convergence study was done on the mesh size. The conclusion from this was that a mesh size of maximum 10 mm was sufficient for convergence on the section parameters. Submitting a *beam section generate* job in Abaqus generates a .bsp-file that contains the cross-section properties.

The particular properties that were collected from each .bsp-file were

- Solid area
- Second moment of inertia, I_{11} and I_{22}
- Torsional stiffness, I_t
- Distributed mass per meter
- Moment inertia, i_{11} and i_{22}

Additionally, the area within the box girder as well as the perimeter were calculated with a self-made Python script. Before the cross-section properties could be used in the global modal analysis, some extra mass and moment inertia had to be included, since weight from e.g asphalt and bulkheads will have a significant influence on the modal properties of the bridge. The extra weight was calculated under the following assumptions:

- 80 mm asphalt on the whole width of the traffic and pedestrian lanes. Asphalt density of $2500\text{kg}/\text{m}^3$. Moment inertia calculated as rectangle rotating around its center.
- Bulkhead with effective thickness of 16 mm every 3.9 meters. Moment inertia calculated as rectangle rotating around its center.
- Hanger heads with contribution of 30 kg/m on mass have negligible moment inertia

- Mass from other equipment is set to 400 kg/m. Moment inertia not calculated because of its unknown geometry.

The additional mass and inertia was added to the girder mass and inertia, and all the properties were written and stored to a .csv- file. The section analysis was carried out and the resulting properties were stored for all the cross-section ranges of interest. Properties for five of the sections are shown in Table 3.3.

Table 3.3: Summary of the section properties for the different girder heights.

Parameter	LN22_3500	LN22_3750	LN22_4000	LN22_4250	LN22_4500
Girder height [m]	3.50	3.75	4.0	4.25	4.50
Solid area [m ²]	2.397	2.399	2.402	2.404	2.407
I_{11} [m ⁴]	5.155	5.764	6.364	6.946	7.500
I_{22} [m ⁴]	186.213	186.394	186.541	186.656	186.743
I_t [m ⁴]	18.320	20.164	21.892	23.479	24.904
Girder mass [kg/m]	6471.900	6478.600	6485.200	6491.900	6498.500
Total mass [kg/m]	13056.398	13110.604	13169.881	13204.430	13244.050
i_{11} [kgm ² /m]	15327.717	17169.557	19009.242	20817.766	22566.823
i_{22} [kgm ² /m]	857625.220	861195.819	864359.191	867125.335	869503.251
Perimeter [m]	63.126	63.196	63.266	63.337	63.407
Inner area [m ²]	86.170	90.459	94.311	97.728	100.709

A function for linear interpolation of cross-section properties was made in order to extract the properties for arbitrary cross-section heights. This could have been carried out by a section analysis for each iteration of the optimization algorithm. However, this would add about 30 seconds to each iteration in the optimization. The interpolation seemed to be sufficiently accurate as long as the step size on the cross-section height was low enough. The step size was set to 0.125 m. Interpolated cross-section properties were then considered to be convenient to speed up the final optimization algorithm.

3.4 Wind-tunnel testing

The ADs that are later utilized in stability limit calculations are most accurately determined experimentally with wind-tunnel tests. By testing the cross-section range presented in Section 3.3, the idea was to create surrogate models such that ADs could later be extracted for arbitrary cross-section heights within the range. The wind-tunnel tests were executed in a forced vibration rig at the fluid mechanics laboratory at NTNU in Trondheim. Section models in scale 1:70 were fixed between two load cells, that are also able to move in an arbitrary motion described by three DOFs, r_y , r_z and r_θ , where θ is the rotation around the section model longitudinal axis, x . This is illustrated in Figure 3.6. The load is then recorded with the same DOF reference, as the wind flow approaches the nose of the cross-section. By recording the load for particular load patterns, the aerodynamic derivatives as well as the quasi-static coefficients can be extracted.

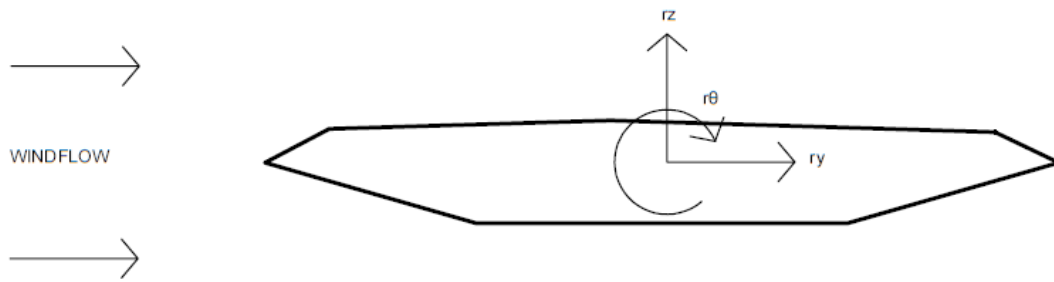


Figure 3.6: The reference system for the sections models in the wind-tunnel tests

To make the section models in 1:70 scale, two plates with thickness 40 mm were glued together with a $\text{Ø}40$ mm aluminium pipe between them. Along with providing stiffness to the section model, the pipe is the section models' connection to the force vibration rig. The section shapes were then milled out of Dyvincell material using a CNC-machine programmed with coordinates extracted from the drawings in Figure 3.3. Railings for both the traffic and the pedestrian lane, as well as railings for a maintenance trolley were modelled using the software Solidworks, and then 3D-printed. Drawings of the parts are shown in Figure 3.8. Unfortunately, the scale on the railing parts was set to 1:50 by a mistake. This was not noticed in time to change it. The effect this had on the results will be discussed later in the report. With some anchoring length, the plastic parts were stuck into the Dyvincell material like shown in Figure 3.7.

In order to isolate the effect of the self-excited forces there were milled out space at the mid-span of the section models to make room for a tuned mass damper (TMD). The TMD was a steel piece of approximately 100 grams, giving it a mass ratio of approximately 0.2 %. This was allowed to vibrate on an elastic timber stick that was stuck into the Dyvincell material. To cancel out vortex induced vibration (VIV), the mass on the stick could be pulled in and out to adjust the length of the elastic stick, adjusting also the natural frequency of the TMD.

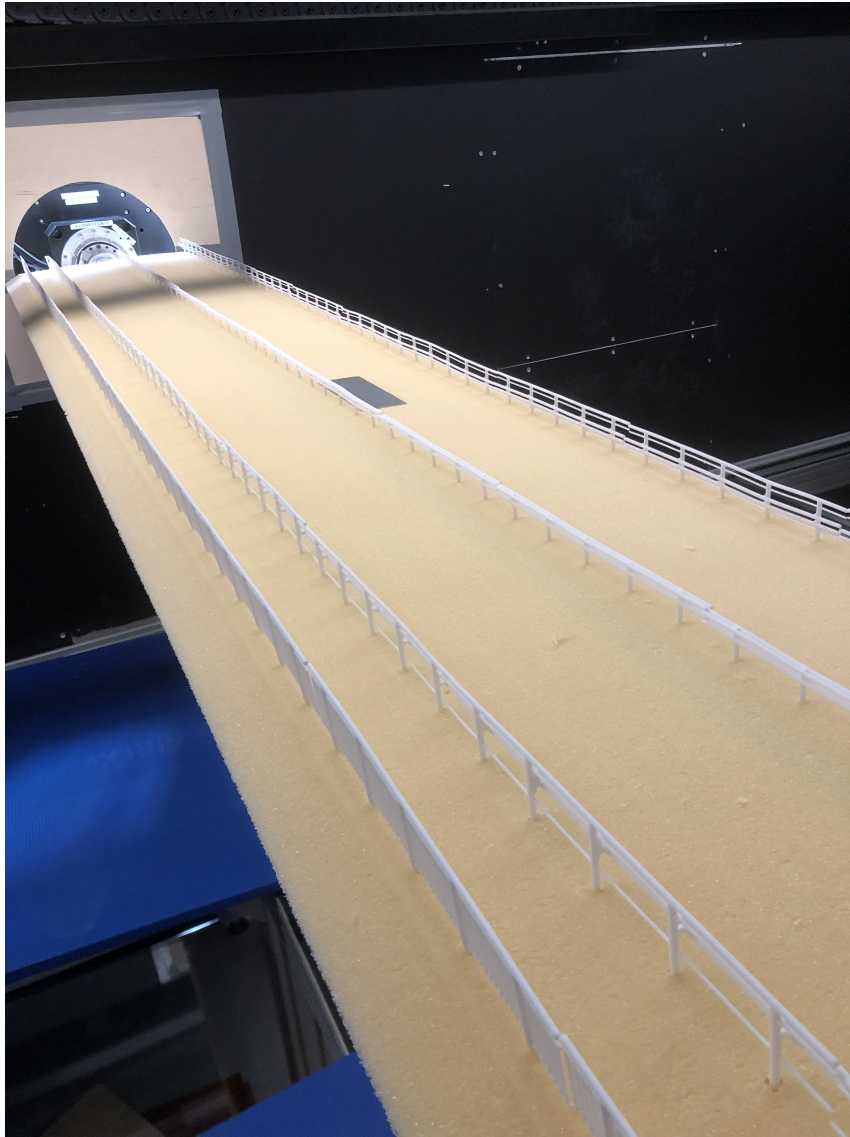


Figure 3.7: Photo of a section model with railing

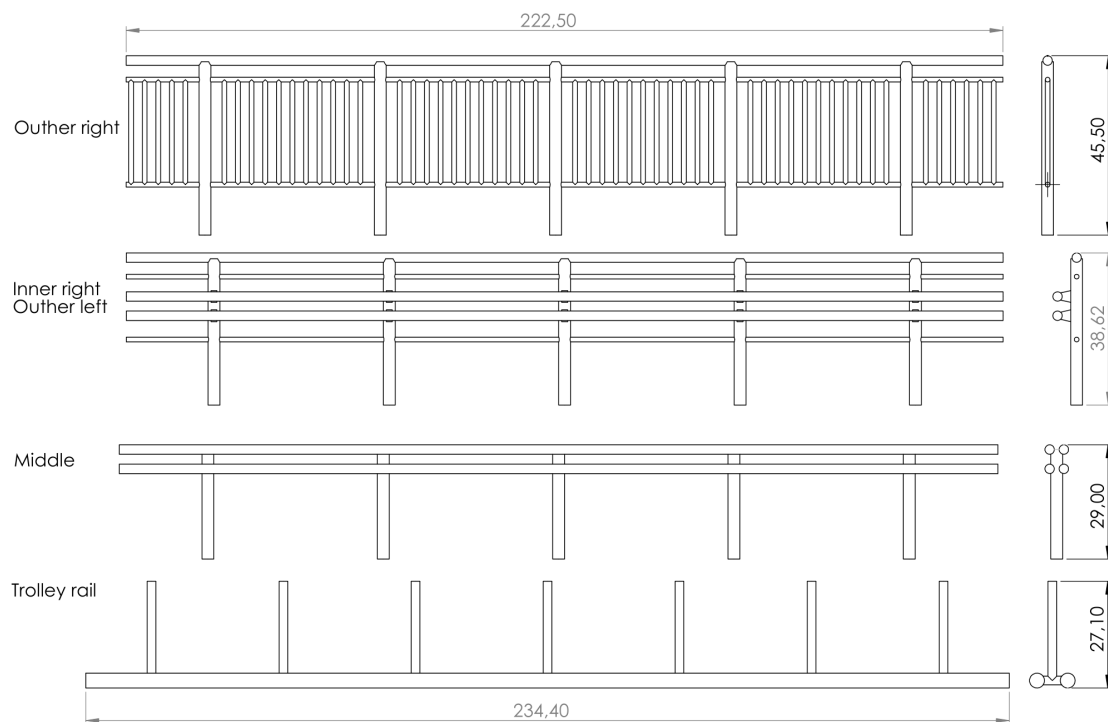


Figure 3.8: Railing drawings

Figure 3.9 shows a section model fixed up in the wind-tunnel. The testing area is 1.8 meters high, 2.7 meters wide, and 11.1 meters long. Each side of the section model is fixed with clamps attached to Gamma load cells supplied by ATI Industrial Automation [13]. The load cells are mounted on the 3-DOF actuators, which are controlled by a MC4U control system from ASC Motion Control.

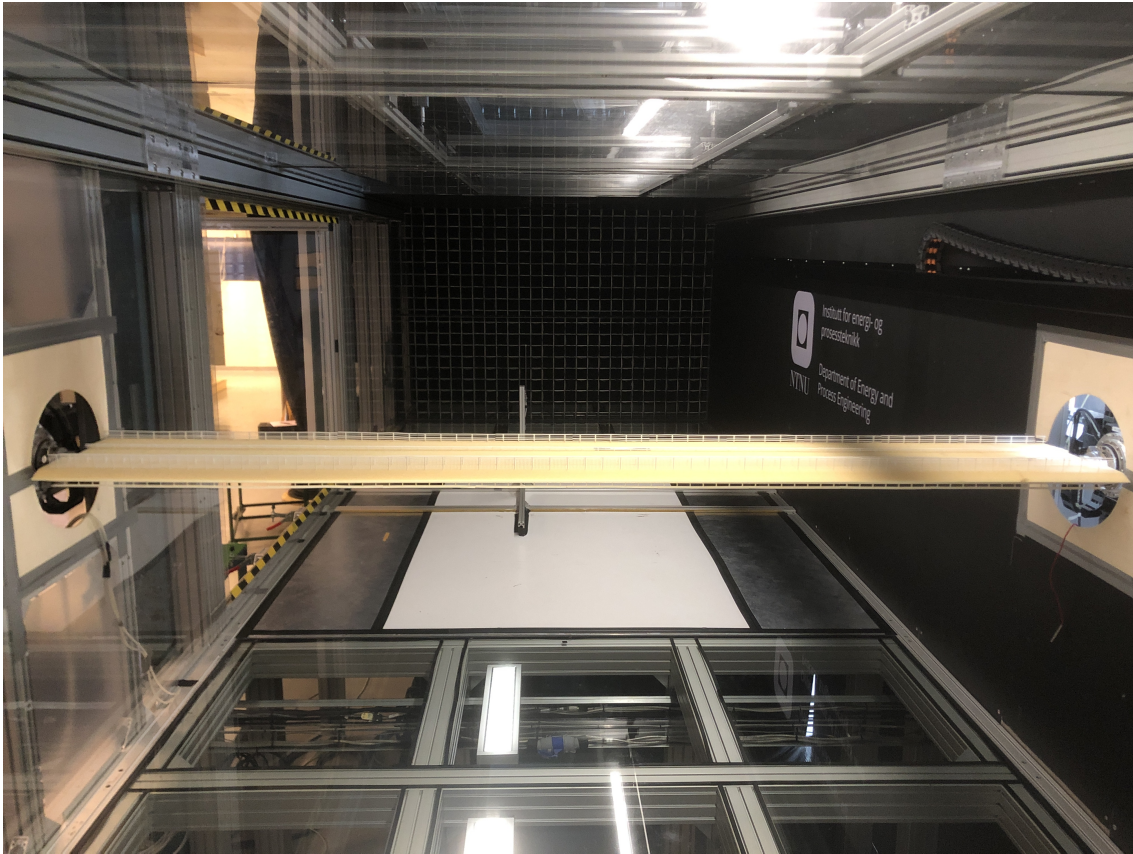


Figure 3.9: Photo of the section model fixed into the forced vibration rig

According to the test plan including tests for vortex shedding, static coefficients and aerodynamic derivatives, the section models were tested one by one. An overview of the test plan for each section-model is shown in Table 3.4.

Table 3.4: Summary of the tests ran in the wind-tunnel.

Test	Wind speed [m/s]	Motion	Amplitude	Purpose
Vortex shedding	10	None	None	Observe VIV effects
Static tests	0, 6, 8, 10	Angular steps	8° (max)	Static coefficients
Single harmonic	0, 8, 10	Horizontal harmonic	20 mm	Horizontal ADs
	0, 8, 10	Vertical harmonic	10 mm	Vertical ADs
	0, 8, 10	Torsion harmonic	1°	Torsion ADs

The section models were fixed in the rig with the pedestrian lane downwind, and the load cells were reset to cancel out the self-weight before the recording was started. For the first VIV test, the TMD was deactivated (pushed all the way in), and the wind speed was increased from 0 to 10 m/s, observing potential load fluctuations from vortex shedding. If there was any significant VIV, the TMD was activated (pulled out), and the VIV test was redone.

Then, predefined motion patterns were loaded onto the control system. Static tests were first carried out. The section models were rotated as the plot in Figure 3.10 shows. While

the angular velocity here is very low, the motion induced effects are negligible. The drag, lift, and pitching moment coefficients can then be extracted in a static manner as functions of the attacking angle, θ . The motion pattern is performed for still air, 6, 8, and 10 m/s. The still-air tests are to determine the effects of inertia forces from the motion pattern. These are later to be subtracted to isolate the load from the drag, lift and pitching moment caused by the wind-flow on the section models.

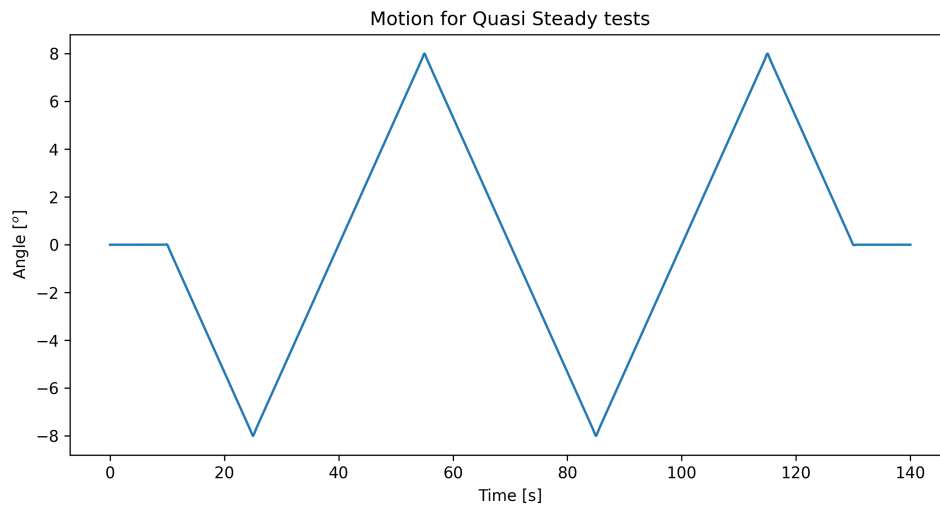


Figure 3.10: Motion plot for quasi steady test

At wind-speeds of 0, 8, 10 the section models were vibrated as the motion patterns described in Figure 3.11. These are harmonic motions corresponding to frequencies of 0.25, 0.50, 0.77, 1.1, 1.4, 1.7, 2.0 and 2.5 Hz.

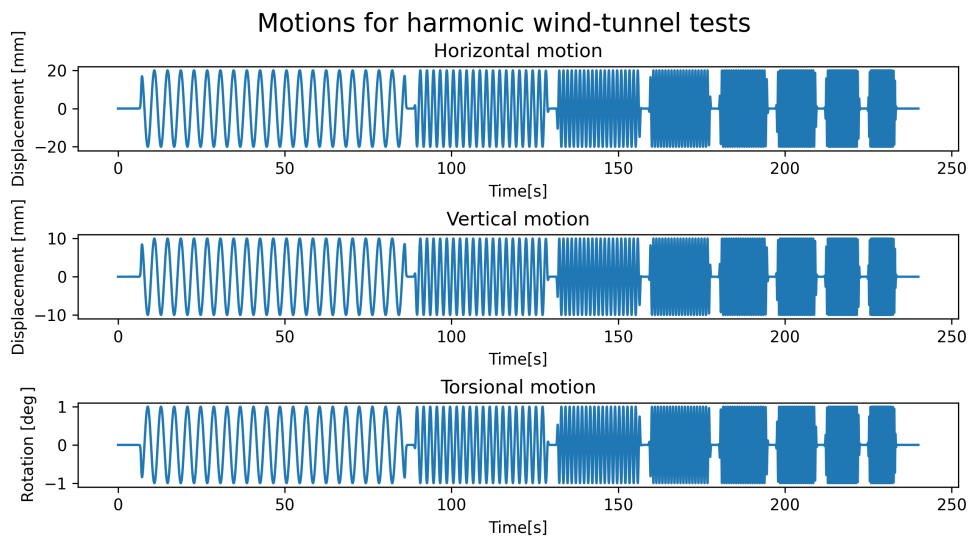


Figure 3.11: Motion plots for harmonic tests

Again, the wind-induced forces could be isolated by subtracting the forces recorded in still-air. What is left is then the self-excited forces that can be seen on the left hand side of the Equation (2.48), (2.49) and (2.50). The self excited forces are recorded at two non-zero wind velocities and eight different vibrations frequencies. This gives a total of 16 data points, while the reduced frequency and the reduced wind velocity are dependent on each other. With a least squares fit approach, the reduced velocity dependent ADs was extracted. This post-processing part was done, by our supervisor Ole Øiseth, with use of his self-made Python library.

3.5 AD surrogate models

Surrogate models were made in order to extract the AD-values which were necessary to calculate the stability limits. Assuming that the surrogate models were representable within the cross-section range, the stability limits could be calculated for arbitrary cross-section heights. The Python library scikit-learn offers a comprehensive module for Gaussian Process Regression (GPR) which is used to create the models [32]. Figure 3.12 shows an example model illustrating how the GPR predicts AD-data between the measured data points which are functions of girder height, H and reduced velocity \hat{V} .

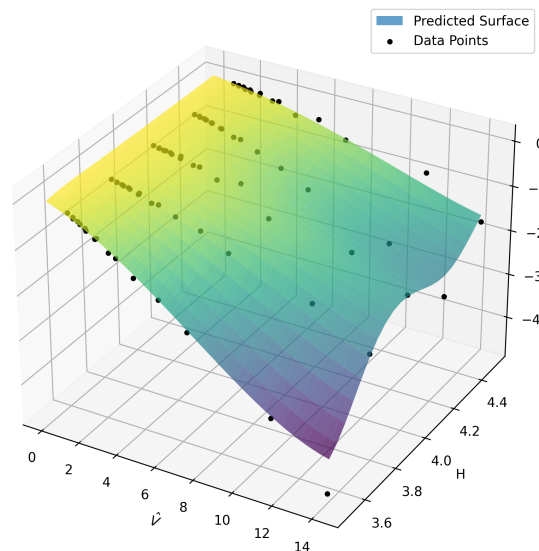


Figure 3.12: Illustration of a surrogate model

The module also comes with a wide variety of pre-defined kernel functions. Considering Stein (1999), Matern is selected as the kernel function for the Gaussian process [22][23]. This is to accommodate the amount of scatter and occasionally sparse measuring density in the test data and the desire to develop relatively smooth models. The length scale parameter is set to 0.5 for the height axis and 4.5 for the reduced velocity axis based on the maximum measurement spacing in the wind-tunnel data. The smoothness parameter, ν , is set to 2.5. Global noise is added to the model through the alpha parameter, which is set to 0.13. The alpha parameter is set based on trial-and-error to obtain sufficiently smooth models.

3.6 Calculation of critical wind speed

With modal properties calculated with the parametric Abaqus model and ADs for arbitrary cross-section height extracted from the surrogate models, the stability limits could be calculated as a function of the two main parameters, tower and girder height. Calculation of the critical wind speed at which dynamic instability occurs is done numerically in a Python script. The script was developed with great help from Jungao Wang from the NPRA, and is based on the Ge and Tanaka (2000) approach [17]. The assembly of M, C and K with aerodynamic stiffness and damping contributions is done according to Chapter 9 in Strømmen (2010) at discrete reduced velocity steps [12]. The initial structural damping ratio is set to 0.2 % in accordance with *N400 Bruprosjektering* [3]. The script automatically generates the necessary modal data from the global Abaqus analysis and pull ADs from the surrogate models. The pseudocode for the iterative and highly computational process is presented below.

Algorithm 1 Calculation of critical wind speed, V_{cr}

Input

- Modal properties: $\tilde{M}, \phi, \omega_n$
- Aerodynamic derivatives from surrogate models

Output

- Critical wind speed, V_{cr} [m/s]

```

1: for  $U$  in  $U_{range}$  do
2:   for  $\omega_n$  in  $\omega$  do
3:     - Assemble  $M, C$  and  $K$  with  $C_{ae}$  and  $K_{ae}$  contributions wrt.  $(U, \omega)$ 
4:     - Solve complex eigenvalue problem on state space form  $\rightarrow eigvals$ 
5:        $Re(eigvals) = \zeta_n \omega_n$ 
6:        $Im(eigvals) = \omega_n \sqrt{1 - \zeta_n^2} = \omega_D$ 
7:       while  $|(\omega_D - \omega_n)| > tol$  do
8:          $\omega_n = \omega_D$ 
9:         - Assemble  $M, C$  and  $K$  with  $C_{ae}$  and  $K_{ae}$  contributions wrt.  $(U, \omega)$ 
10:        - Solve complex eigenvalue problem on state space form  $\rightarrow eigvals$ 
11:        if  $\zeta_n \omega_n = 0$  then
12:           $V_{cr} = U$ 
13:           $\omega_{cr} = \omega_D$  ▷ Which is used to extract the instability mode shape
14:          break

```

The process terminates (breaks) when the real part of the complex eigenvalue becomes zero. This defines the instability limit, as the in-wind damping ratio defined in Equation (2.80) now becomes negative. The current mean wind speed and frequency are then returned as critical values. The eigenvector corresponding to the critical frequency is also extracted to investigate the mode-participation in the critical mode.

3.7 Optimization

An optimization algorithm was developed with the goal of returning the optimal configuration with respect to the main parameters; tower and girder height. The optimization algorithm con-

sists of two main components, a constraint function and an objective function. The constraint function is described in Section 3.6. According to the *N400 Bruprosjektering* motion induced instabilities shall be controlled towards a design criterion of

$$V_{cr} \geq V_m \cdot \gamma_{V_{crit}} \quad (3.2)$$

where $\gamma_{V_{crit}} = 1.6$ and V_m is the site wind velocity measured at the height of the bridge deck for a return period of 500 years [3]. V_{cr} is calculated to 76 m/s for the Langenuen crossing [27], such that the inequality constraint function reads

$$V_{cr}(h_t, h_g) - 76 \geq 0 \quad (3.3)$$

where h_t and h_g are the tower and the girder height, respectively.

The bridge concept is proposed to be optimized with the objective of minimizing material costs. The objective function is then simply the material quantities for the different bridge parts, multiplied with price factors. Denoting the different parts

- t: towers
- g: girder
- c: main cables
- h: hangers

the objective function is defined

$$Obj(h_t, h_g) = \sum_n Q_n(h_t, h_g) \cdot P_n \quad (3.4)$$

for $n \in [t, g, c, h]$, where Q_n is the quantity for the part for the current configuration of h_t and h_g in unit m^3 , and P_n is the price factor for the part in unit NOK/m^3 . The quantities are calculated numerically in dedicated Python-scripts, which are based on the geometry of the different parts.

The price factors are set based on Dr. Techn. Olav Olsens report from the preliminary study of the Langenuen crossing [27]. The report includes cost estimations to compare the total cost of the different concepts. By dividing the total cost of each bridge part by its quantity, the unit cost price factor is found for the concrete tower, the main cables, the steel hangers, and the aluminium girder. These are summed up in Table 3.5.

Table 3.5: Price factors used for the objective function.

Bridge part	Cost [NOK/m^3]
Concrete tower	326948
Main cables	86535
Steel hangers	691358
Aluminium girder	1543210

Dr. Techn. Olav Olsens price estimations are quite detailed for the aluminium girder, including cost for material, welding, handling and facility and installation. The price estimations on the cables, hangers, and towers are not described in detail. One would probably not expect

the price functions to be linear, so assuming this is a very rough simplification. Detailed price estimations were not part of the primary scope of this project. Therefore, this part was given less attention.

Several sub-algorithms were considered to generate new input parameters h_t and h_g to approach the minimum of the objective function. The SciPy library provides optimization algorithms in Python, such as `scipy.minimize` that can be used to minimize objective functions in a gradient-based sense [24]. Our inequality constraint could easily be implemented, but the `scipy`-algorithm seemed to use too many iterations considering our time-demanding inequality function. It should also be noted that the `scipy.minimize` algorithm only finds the local minimum, and thus comes with the risk of missing the actual optimum.

Bayesian Optimization was also considered to minimize the objective function. This is an expansion of Gaussian Process Regression (GPR) that includes an algorithm to suggest the next sampling point based on a probability of improvement (reduction) of the objective function [26]. For each iteration, the function will improve a surrogate model, providing higher accuracy in the areas near the assumed lower extremes. This function seemed appropriate to get a good prediction of the objective function with fewer iterations than `scipy.minimize`. With little prior knowledge on the topic, the inequality constraint appeared to be difficult to implement without drastically increasing the computational time. Still, one could use the algorithm to create a surrogate model for the critical wind velocity, but because of the acquisition function the surrogate would then become more accurate in some regions than other.

The conclusion was to carry out the optimization more manually by a grid search, iterating over a pre-defined grid for the tower and girder height. Surrogate models for the objective and constraint functions could then be generated separately utilizing GPR. All of the configurations that meet the wind-speed criteria could be saved, and the objective function could be minimized with respect to these configurations. One can imagine that both surrogate models for the material cost and the critical wind will be quite smooth surfaces within the search space. This justifies that a GPR of a grid search with a reasonable grid mesh size can create representative models for cost and critical wind speeds. However, it might require some testing and engineering judgement in the choice of a sufficiently fine grid mesh, as well as the GPR-parameters.

The bounds of the main parameters were set to $h_t \in [180, 220]$ and $h_g \in [3.5, 4.5]$ with sampling steps of 2 meters and 0.25 meters for tower and girder height, respectively. The covariance function for creating the GPR is the Matern-kernel. The length scale is set equal to the sampling steps in the corresponding parameter dimension, while the smoothness parameter ν is set to 2.5. The α -parameter is set very low, which means that the GPR does not account for any significant noise in the sampling data. The resulting GPR-models were visually examined and considered to give a representative model for the whole search space.

Other than just returning the optimal configuration of the input parameters, a grid search provides models that should be representative for the whole search space. This can give valuable understanding of general aerodynamic design of suspension bridges. It can also be useful if other objectives, such as environmental impact, are added in the bridge design decision making.

3.8 Buffeting response

The calculation of buffeting response is currently not implemented in the optimization, due to the fact that this was not within the initial scope of this project. However, to assure that the response was within reasonable limits, a separate calculation on the configuration returned from the optimisation algorithm was conducted. Previous studies of the Langenuen crossing have shown that the aluminium girder concepts are vulnerable with regards to fatigue. Thus, the buffeting response is highly relevant in the design of such a bridge.

By utilizing relations presented in the theory chapter, the buffeting response spectrum could be calculated with the use of modal coordinates. This approach was first presented by Scanlan (1978), and has been commonly used since [33][34]. Utilizing the results from the global Abaqus analysis, the modal properties of the structure was extracted. Including the aerodynamic contributions that could be defined with use the of the surrogate models explained in Section 3.5, the equation of motion with modal coordinates could be determined as

$$\tilde{\mathbf{M}}\ddot{\eta}(t) + (\tilde{\mathbf{C}} - \tilde{\mathbf{C}}_{ae})\dot{\eta}(t) + (\tilde{\mathbf{K}} - \tilde{\mathbf{K}}_{ae})\eta(t) = \tilde{\mathbf{Q}} \quad (3.5)$$

leading to the modal frequency response matrix

$$\tilde{\mathbf{H}} = [-\omega^2\tilde{\mathbf{M}} + i\omega(\tilde{\mathbf{C}} - \tilde{\mathbf{C}}_{ae}) + (\tilde{\mathbf{K}} - \tilde{\mathbf{K}}_{ae})]^{-1} \quad (3.6)$$

From Equation (2.34), only the buffeting load $\mathbf{B}_q\mathbf{v}(x, t)$ is considered, while this is what causes the fluctuating response. The force coefficients that assemble the B_q -matrix were extracted from the static test wind-tunnel data. The data was a bit noisy, especially for the drag coefficient, which made it difficult to calculate the static coefficients' derivatives. To get representative values of the force coefficients, the wind-tunnel data was smoothed using a moving average function with a time window of 400. An example of this is shown in Figure 3.13. As a simplification, the buffeting response is calculated by picking the static coefficients for a mean attacking angle, $\bar{\alpha}$ of zero. However, a study of the buffeting responses sensitivity to the mean attacking angle was conducted.

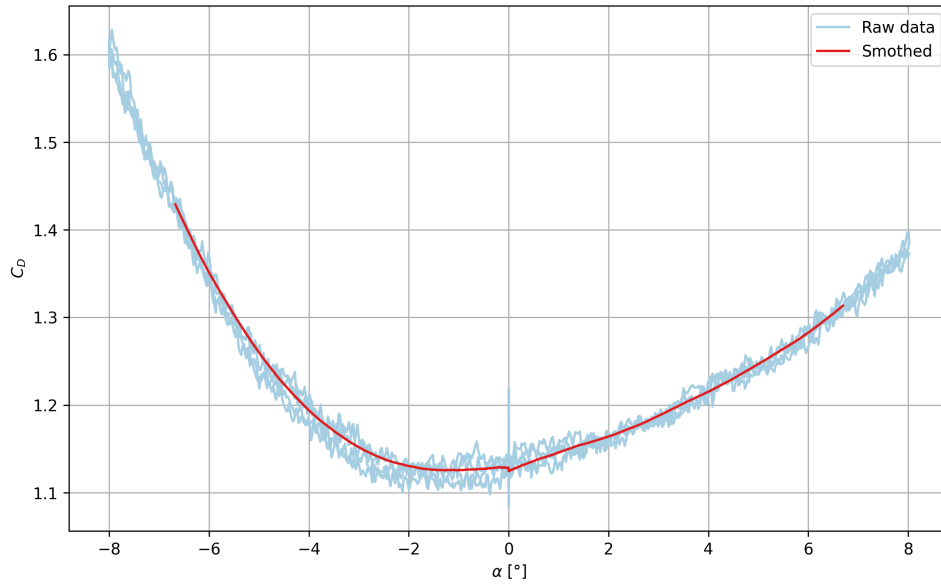


Figure 3.13: Plot illustrating the smoothing of the force coefficients

Referring to Equation (2.10) the modal load can be expressed as

$$\tilde{\mathbf{Q}} = \int_0^L \boldsymbol{\phi}(x) \mathbf{B}_q \mathbf{v}(x, t) dx \quad (3.7)$$

It can be convenient to work in the frequency domain to utilize the relation derived in e.g Newland (2005) [11]

$$\mathbf{S}_\eta(\omega) = \tilde{\mathbf{H}}^*(\omega) \mathbf{S}_{\tilde{\mathbf{Q}}}(\omega) \tilde{\mathbf{H}}^T(\omega) \quad (3.8)$$

where * denotes the complex conjugated. The modal frequency response matrix is already presented, but the modal load has to be transferred to the frequency domain. Using the cross-correlation function presented in Equation (2.17), the cross-correlation matrix of the modal load can be derived as

$$\mathbf{S}_{\tilde{\mathbf{Q}}}(\omega) = \int_0^L \int_0^L \boldsymbol{\phi}^T(x_1) \mathbf{B}_q(x_1) \mathbf{S}_v(\omega, \delta x) \mathbf{B}_q^T(x_2) \boldsymbol{\phi}(x_2) dx_1 dx_2 \quad (3.9)$$

The wind turbulence matrix $\mathbf{v}(x, t)$ is then replaced by the cross spectral density (CSD)

$$\mathbf{S}_v = \begin{bmatrix} \mathbf{S}_{uu} & \mathbf{S}_{uv} & \mathbf{S}_{uw} \\ \mathbf{S}_{vu} & \mathbf{S}_{vv} & \mathbf{S}_{vw} \\ \mathbf{S}_{wu} & \mathbf{S}_{wv} & \mathbf{S}_{ww} \end{bmatrix} \quad (3.10)$$

with the turbulent components u, v, w parallel to the bridge coordinate axes y, x, z , respectively.

Since site measurements of the wind were not available, the CSD is defined according to the guidelines in *N400 Bruprosjektering* [3]. The handbook use a Kaimal spectrum to describe the turbulence [35], such that the single point spectrum is defined as

$$S_i(\omega) = \frac{A_i \hat{\omega} \sigma_i^2}{\omega(1 + 1.5A_i \hat{\omega})^{5/3}} \quad (3.11)$$

for $i = u, v, w$ where

$$\hat{\omega} = \frac{\omega^x L_i(z)}{2\pi v_m(z)} \quad (3.12)$$

$$A_u = 6.8, A_v = 9.4, A_w = 9.4 \quad (3.13)$$

The turbulence length scale, which describes the average size of the wind eddies, is given by

$${}^x L_u = \begin{cases} L_1(z/z_1)^{0.3} & \text{if } z > z_{min} \\ L_1(z_{min}/z_1)^{0.3} & \text{if } z \leq z_{min} \end{cases} \quad (3.14)$$

and can be transferred to other directions as

$$\begin{bmatrix} {}^y L_u \\ {}^z L_u \\ {}^x L_v \\ {}^y L_v \\ {}^z L_v \\ {}^x L_w \\ {}^y L_w \\ {}^z L_w \end{bmatrix} = {}^x L_u \begin{bmatrix} 1/3 \\ 1/5 \\ 1/4 \\ 1/4 \\ 1/12 \\ 1/12 \\ 1/18 \\ 1/18 \end{bmatrix} \quad (3.15)$$

The term σ_i denotes the standard deviation of the turbulence component, v_m is the mean along wind velocity, z is the height above the terrain at the site, L_1 is the reference length equal to 100 meters and z_1 is the reference height equal to 10 meters. The frequency axis, ω , is here in unit [rad/s].

Further, the co-spectra is given by

$$S_{i1i2}(\omega, \Delta s_j) = \sqrt{S_{i1}(\omega)S_{i2}(\omega)} \cdot e^{-C_{ij} \frac{\omega \Delta s_j}{v_m(z)}} \quad (3.16)$$

where Δs_j is the spacing between the two points along the considered coordinate axis, j , and C_{ij} is the decay factor defined as

$$C_{uy} = C_{uz} = 10, C_{vy} = C_{vz} = C_{wy} = 6.5, C_{wz} = 3.0 \quad (3.17)$$

The buffeting response in the longitudinal direction is considered as negligible, such that the v-components can be disregarded. For simplicity, the cross-correlation of u- and w-components is set to zero such that

$$\mathbf{S}_v = \begin{bmatrix} \mathbf{S}_{uu} & \mathbf{0} \\ \mathbf{0} & \mathbf{S}_{ww} \end{bmatrix} \quad (3.18)$$

In any case, this correlation is expected to be small, which justifies the simplification.

By defining the turbulence intensities I_u and I_w in accordance to the guidelines from *N400* and *NS-EN-1991-1-4*, the CSD of the turbulence could be defined for any mean along wind velocity [3][36].

$$I_u = \frac{\sigma_u}{v_m} = 0.10, I_w = \frac{\sigma_w}{v_m} = \frac{1}{4}I_u \quad (3.19)$$

As the response spectrum was found for the modal coordinates it was transferred back to the physical coordinates with the relation [12]

$$\mathbf{S}_r = \boldsymbol{\phi} \mathbf{S}_\eta \boldsymbol{\phi} \quad (3.20)$$

It can be shown that the variance of a process can be found by integrating its auto-spectral density (ASD), such that [11]

$$\sigma_r = \sqrt{\int_{-\infty}^{\infty} S_r(\omega) d\omega} \quad (3.21)$$

This sums up the script that was written in Python, enabling the calculation of standard deviations of the buffeting response for any configuration of the tower height and girder height, for an arbitrary mean wind velocity.

Chapter 4

Optimization program

4.1 Objective and structure

An optimization program was developed with the objective of finding the optimal aerodynamic design for single-span suspension bridges with respect to cost. The program operates with the two geometric parameters, tower and girder height, and an algorithm eventually returns the most economical design that also satisfies the design criteria for critical wind. From the very beginning, it has been a priority to make the program as automatic, general, and time-effective as possible. The idea of further development and expansion has also been kept in mind when developing the program. This is the reason why the authors decided to keep the components of the program separate and not combine them into a main control script. By keeping the components separate, the program becomes more transparent and easier to debug with the implementation of new data and further expansions.

The program consists of two components: Python and Abaqus. Python has a very versatile application area in the program and makes up everything from heavy numerical computations to folder and file management. Abaqus is used for its FEM-solver, which offers parametric modeling. Abaqus is also compatible with Python, and allows the program to be controlled solely from a Python IDE. Therefore, one can perform Abaqus analyses without ever having to open the Abaqus GUI. The program is built around the Langenuen crossing as an example, and is still indented to be in the development phase. It does not have a single script to control the whole program, but rather several sub-scripts that build on each other and can be run independently. The program is presented in a digital appendix and Figure 4.1 shows the folder structure in the program. The most time-consuming part of the program is the generation of sample data for the optimization algorithm, which for the Langenuen example takes about 1.5 hours and includes 105 Abaqus analyses, flutter, and cost calculations. As can be seen in the figure, the program therefore has active and preliminary components. The purpose of the preliminary components is to save time in the active components. Once the parametric model is defined and the tower and girder height parameter-range is set, one can calculate the cross-section parameters along with the static deflections. These values are needed in advance before every global modal analysis and save the active components for two additional Abaqus analyses per iteration in the data generation.

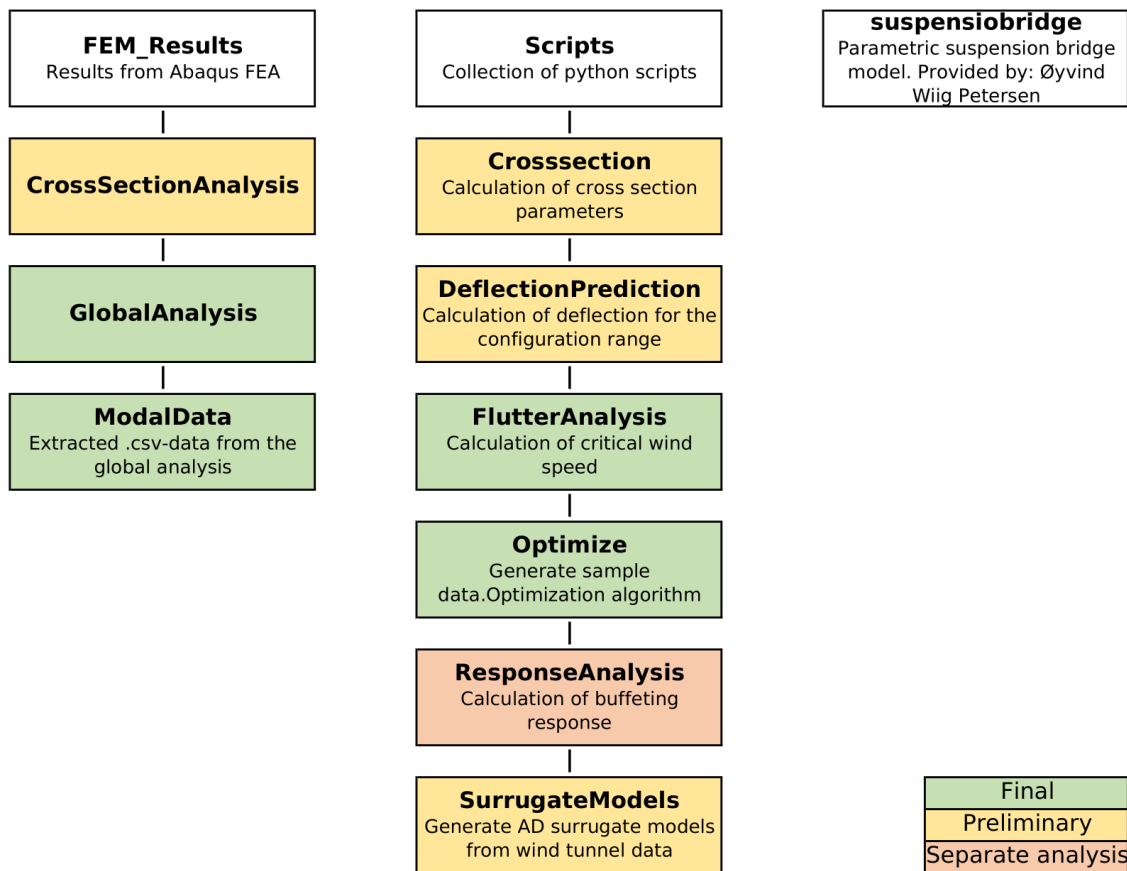


Figure 4.1: Folder structure for the optimization program

The program is also equipped with a separate buffeting response analysis that can be used to calculate the buffeting response for arbitrary design configurations. All the scripts and functions in the program are commented to ease understanding and debugging.

4.2 Quick run with Langenuen example

The program is developed and executed throughout this report in the IDE Virtual Studio Code, also referred to as just VS Code. The integrated terminal in VS Code operates with a fixed path and does not require the user to specify a path for each script. It is therefore recommended to use VS Code's integrated terminal to simplify exploration and testing of the program.

The attached code comes with all the preliminary components executed for the Langenuen crossing, that is:

- Cross-section parameters for the LN22 test range
- Deflection prediction for the LN22 parameter range
- Surrogate models for the aerodynamic derivatives from the wind tunnel testing

If the reader has access to an Abaqus license, one can generate data using the *GenerateData.py* script, followed by the *OptimizeMain.py* script. All the active components will then be ex-

ecuted. If one do not have an Abaqus license, the example data in *SampleDataExample* can be used and one only has to run the *OptimizeMain.py* script to execute the optimization algorithm. The program also includes data to run with cross-sections and ADs from previous master theses (2020, and 2021). Further information and a more detailed user manual may be read in Appendix A.

Chapter 5

Langenuen case study

5.1 Modal analysis

The modal analyses were performed in Abaqus, described comprehensively in Section 3.2. For each analysis, the modal step yields 100 modes, where eigenfrequencies, generalized masses, and modeshapes are extracted from the .odb-file and stored as .csv-files. For the stability and buffeting response analysis, the bridge girder is the main interest. Modeshapes are therefore only extracted for the center nodes of the girder. The modal properties for an example analysis from LN22 with $h_g = 4.0m$ and $h_t = 206m$ are shown in Table 5.1. The table shows the horizontal, vertical and torsional modes among the 40 first Abaqus modes, cable modes are excluded. S and A denotes symmetrical or asymmetrical modes, respectively. Additional illustrations of the mode shapes, as well as modal properties may be found in Appendix B.

Table 5.1: Modal properties for $h_g = 4.0m$ and $h_t = 206m$

Mode	Abaqus no.	Generalized mass \bar{M}_i [kg]	Frequency [Hz]	Horizontal	Vertical	Torsional
HS1	1	10506732	0.0573			
VA1	2	11494151	0.1088			
HA1	3	9054356	0.1411			
VS1	4	5816110	0.1433			
VS2	5	9838898	0.1964			
VA2	8	11391811	0.2195			
HS2	12	11027748	0.2857			
VS3	13	9845412	0.2875			
VA3	16	11143108	0.3545			
TS1	19	4536014	0.3775			
TA1	30	6282704	0.4216			
VS4	31	10412174	0.4330			
HA2	35	8608725	0.5107			
VA4	37	10717055	0.5174			

The first five modes are vertical and horizontal modes. From here on out, cable modes start to occur. The girder modes have more or less sinusoidal appearances, as was predicted from Section 2.2. The first torsional symmetrical mode, TS1, occurs at Abaqus mode no. 19.

A study was conducted to investigate how the natural frequencies are influenced by the change in tower and girder height. The first symmetrical vertical (VS1) and torsional (TS1) modes are picked out as examples since they are normally most likely to couple into flutter [14]. Since VS1 is not perfectly shape-wise similar to TS1, the coupling also depends on contributions from a set of other VS-modes in order to occur. The main cable geometry prevents a vertical eigenmode with only one wave to occur. Figure 5.1 shows surface plots for the eigenfrequencies of the first symmetrical vertical and torsional modes and their frequency ratio.

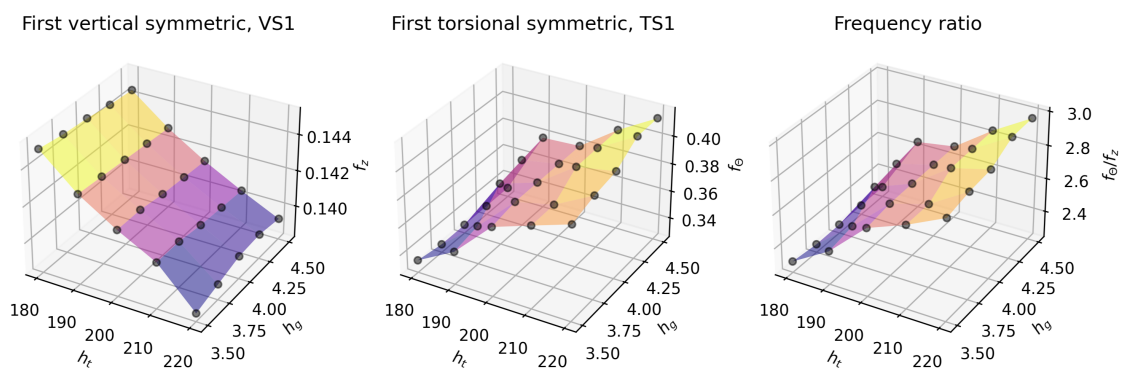


Figure 5.1: Surface plots of the eigenfrequencies for first asymmetric vertical and torsional mode

As shown in the plots, the driving parameter for both frequencies is the tower height, at which the frequencies behave opposite to each other. Table 5.2 displays the maximum and minimum frequencies for VS1 and TS1, as well as the respective configuration and relative difference. The torsional frequency is much more influenced by the change in parameters, and has a 19.9% difference between the max. and min. frequency. The verticals only differ 3.6%, and are less influenced by the change in parameters.

Table 5.2: Maximum and minimum frequency for VS1 and TS1 along with the respective configuration and difference in percent

Vertical	min. [Hz]	Config. [h_t, h_g]	max. [Hz]	Config. [h_t, h_g]	Difference [%]
	0.1397	220,4.0	0.1447	180,4.5	3.6
Torsional	min. [Hz]	Config. [h_t, h_g]	max. [Hz]	Config. [h_t, h_g]	Difference [%]
	0.3319	180,3.75	0.4143	220,4.5	19.9

The change in tower height introduces rather complex changes to the global geometry, which again change the distribution of forces throughout the system. This affects each of the modal stiffnesses, and thus their corresponding natural frequencies. Shifting to the girder height axis in Figure 5.1, the torsional frequency increases with a considerable slope proportional to the increase in torsional stiffness as shown in Table 3.2. The VS1 frequency also increases with the girder height, but with a smaller slope. The frequency ratio between VS1 and TS1 is an

important factor when investigating flutter coupling and will be further discussed later.

5.2 Vortex shedding

VIV was controlled by exposing the fixed section model to an increasing wind velocity, from 0 m/s to approximately 10 m/s. This was to identify potential lock-in phases where resonance between the VIV and the section model eigenfrequency (mainly vertical modes) occurred. There was no observed VIV effect for any of the sections within the wind speed range in the tunnel. Therefore, there is no reason to believe that VIV has affected the results in the other tests in a significant sense. Some VIV was observed when the 4.0 meter section was tested without railing and details. This was at wind speeds in the range 9-10 m/s. Judging from this, the model scale railing was proven effective in disturbing the formation of vortices along the streamlined section. However, it is hard to judge the sections performance with regards to VIV in full scale at higher wind velocities.

5.3 Static coefficients

The trends in the static coefficients were generally the same for all of the five section models that were tested. While the drag coefficient, C_D , had a quadratic looking shape with respect to the attacking angle, α , the lifting and pitching coefficient, C_L and C_M , behaved more linearly with respect to the attacking angle. This is seen from Figure 5.2. The lifting and pitching moment coefficients seemed relatively independent of the wind speed. For the drag coefficient, a slight dependency was observed, especially for some of the models. The highest dependency was found for girder height 3.5 meters, while it was almost negligible for girder height 4.0 meters. This can be seen from Figure 5.2. Any dependency showed a lower drag coefficient for the highest wind speed. For some of the tests it was observed some extra noise around $\alpha = 0$. This appeared as narrow spikes in the plots of the raw data, and was especially present in the data for 4.5 meter model. This noise is assumed to come from disturbance in the test rig, and is therefore disregarded when the static coefficients was extracted for the buffeting response analysis.

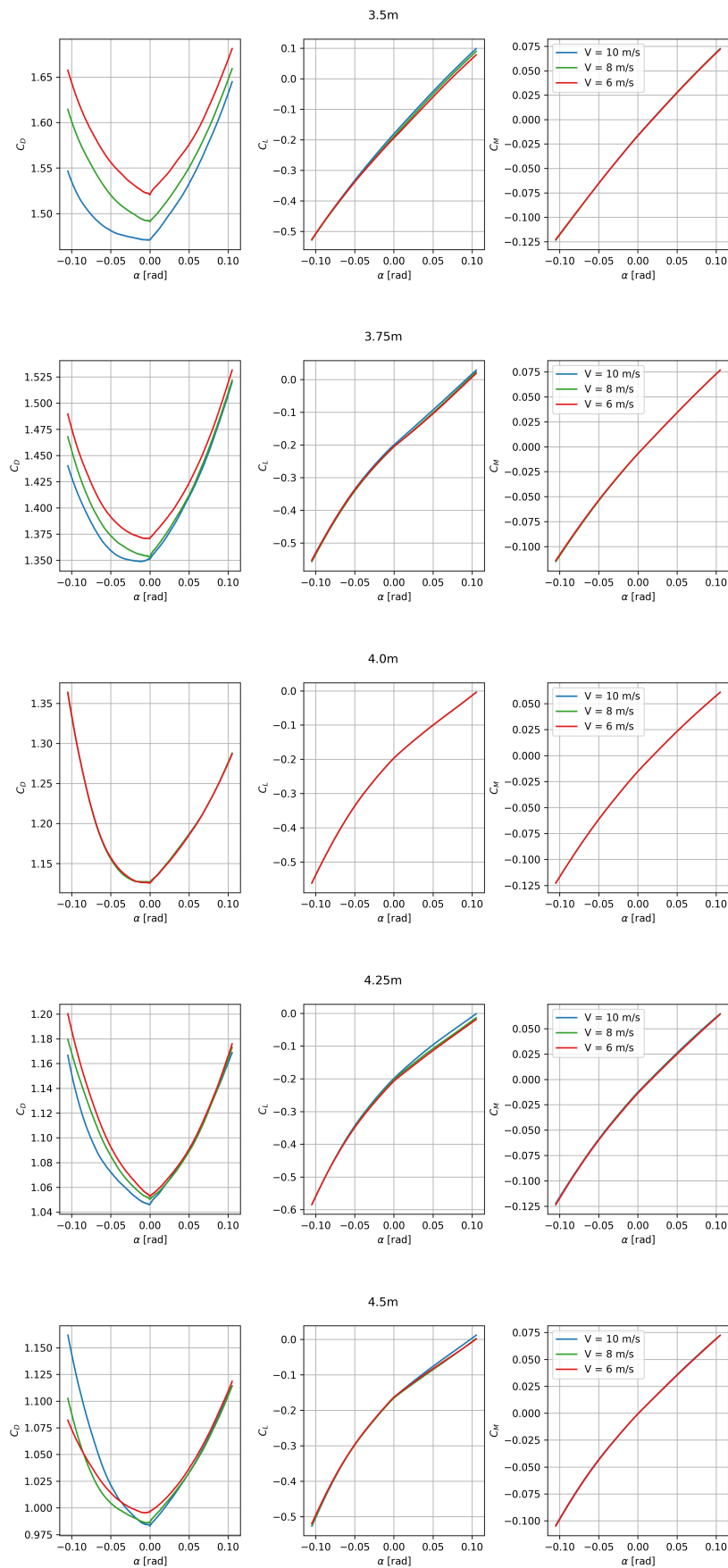


Figure 5.2: Static coefficients resulting from wind-tunnel tests of all section models

A general overview of the static coefficients for the different section models, at $\bar{\alpha} = 0$ and $V = 10.0\text{m/s}$ are shown in Table 5.3. The lower rows show the coefficients for the 4.0 meter girder with no railing, and pedestrian lane flipped upwinds, respectively. These tests are made to isolate the effect of the railing and the asymmetry of the girder. Generally, one can observe a drag coefficient that decreases with the girder height, while the lifting and pitching coefficients are quite stable. The orders of magnitude are quite as expected, judging from previous wind-tunnel testing in other projects, except maybe for the drag coefficients. Compared to tests made by RWDI for NPRA of a similar 4.0 meter girder, the drag coefficients are increased with approximately 25 % [30]. The test without the railing illustrates that the railing significantly increases the drag force. However, the lift force and the pitching moment remain in the same order of magnitude. The asymmetry of the girder section affects the drag force, but not very drastically.

Table 5.3: Summary of the results of the static coefficient tests.

Girder height	$C_D(0)$	$C_L(0)$	$C_M(0)$	$C'_D(0)[rad]^{-1}$	$C'_L(0)[rad]^{-1}$	$C'_M(0)[rad]^{-1}$
3.50	1.49	-0.19	-0.02	0.02	2.82	0.93
3.75	1.35	-0.21	-0.01	0.61	2.23	0.86
4.00	1.13	-0.20	-0.02	0.22	2.40	0.85
4.25	1.05	-0.2	-0.01	-0.33	2.43	0.84
4.50	0.99	-0.17	0.00	-0.01	2.30	0.78
4.00 (No railing)	0.36	-0.21	0.01	-0.95	2.98	1.10
4.00 (Reverse)	1.06	-0.21	-0.01	-0.97	2.61	0.87

The static coefficients are mainly made to calculate the buffeting response. The results are also useful for getting a physical interpretation of the wind-induced forces in a more intuitive manner than by studying the aerodynamic derivatives. For example the results illustrates the effect of railing, with a drag-force increase of about 200 % from the test without railing to the tests with railing. This reveals that the scaling mistake on the railing, as explained in Section 3.4, had a significant effect on both the static coefficients and the aerodynamic derivatives. The C'_M , which participates in the control toward static divergence, is generally low. Based on estimates from some configuration samples, static divergence is considered very unlikely.

The observed wind-speed dependency which was particularly present for the 3.5 meter section, may be due to a Reynolds number dependency because of some turbulence in the wind-flow around the sections. The resulting maximum deviation of approximately 3.3 % indicates that the wind-induced forces on the section is not linear with respect to the wind speed. Matsuda et. al. (2001), however, conclude that conventional wind-tunnel tests in the low Reynolds-number region is on the conservative side for the purpose of bridge deck designing [37]. Nevertheless, one might argue that the data for the 4.0 meter section has the lowest uncertainty.

5.4 Aerodynamic derivatives

By least square fitting, ADs were extracted from the load time series from the wind-tunnel with the use of Equation (2.48), (2.49) and (2.50). The resulting data points for all 18 ADs for the median girder height 4.0 meters are shown in Figure 5.3. The data points are plotted with different colors to indicate which wind tunnel speed the data point was recorded from.

Similar plots for all the section models may be found in Appendix C.

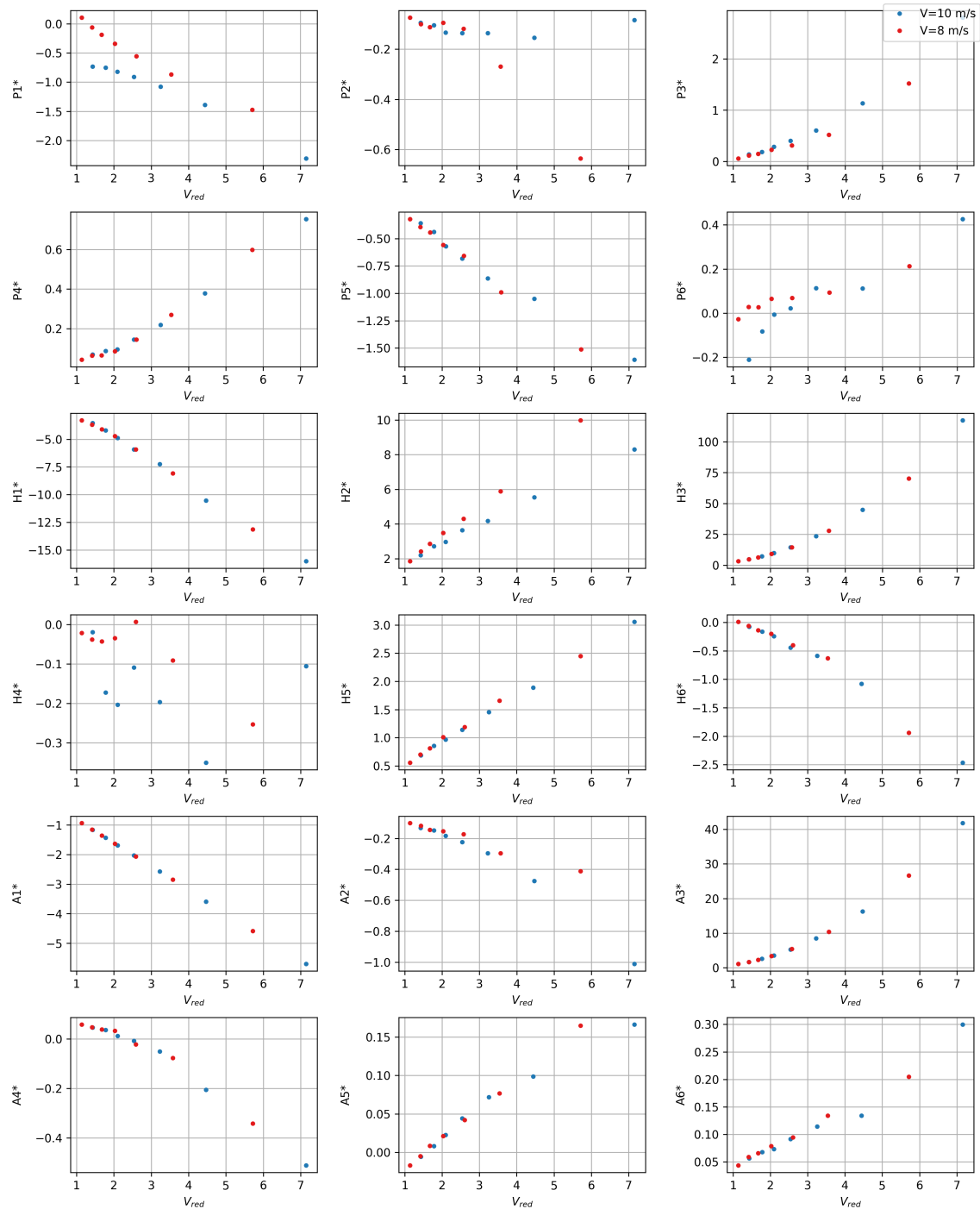


Figure 5.3: Plots of ADs resulting from wind-tunnel tests of the 4.0 meter girder

For each AD, the plots were extended with one dimension, enabling a visualization of the ADs dependency on the girder height. Surrogate models were made using Gaussian Process Regression on the data points in 3D. The surrogate models are shown in Figure 5.4. The sampling

points are also shown in this plot. Up-scaled versions of these plots are shown in Appendix C.

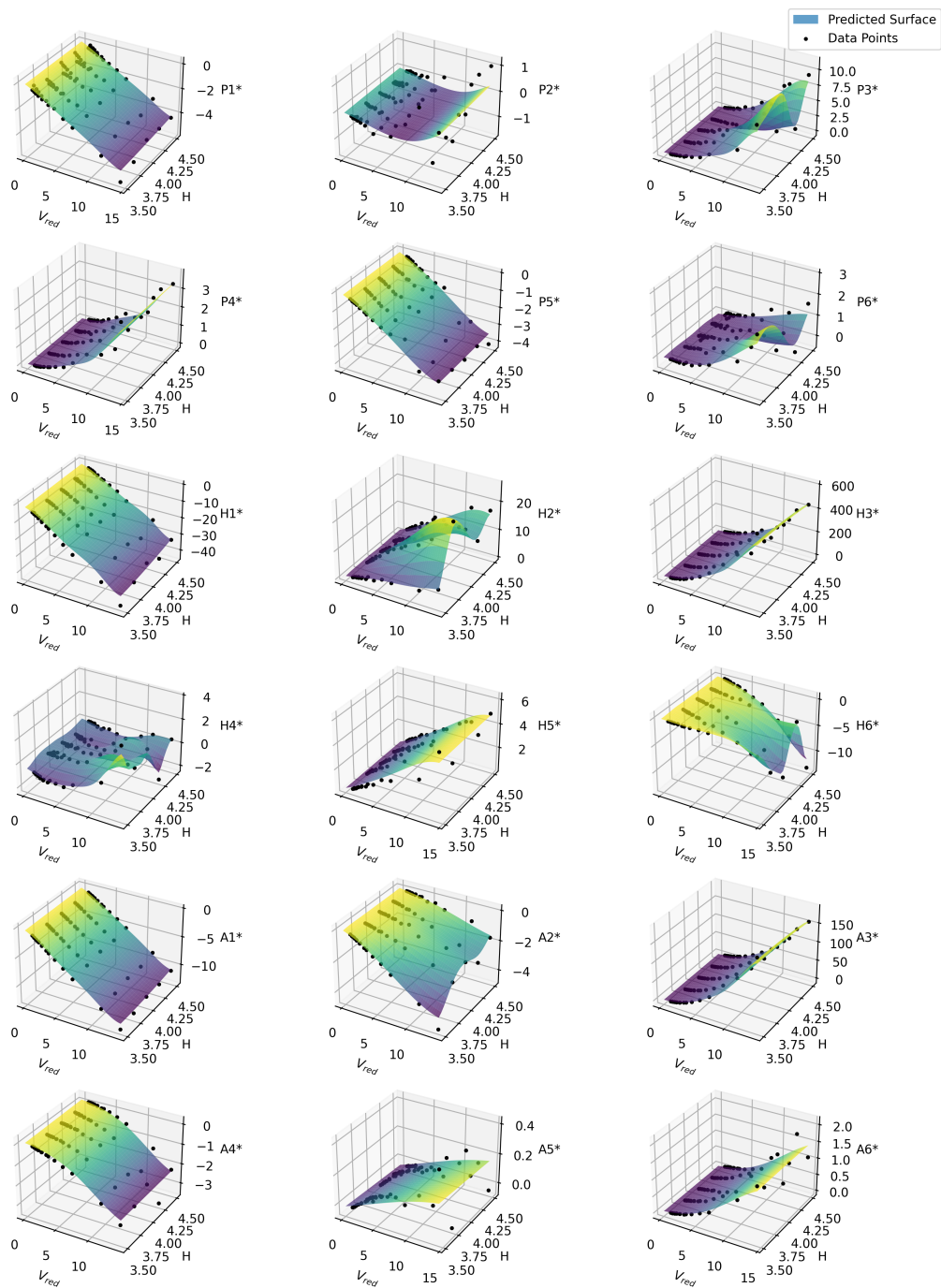


Figure 5.4: Surrogate models for all the ADs

As for static coefficient data, some wind speed dependency can be observed for the aerodynamic derivatives. This is clearly illustrated in the data-points for P1*, P2* and H3* in Figure 5.3. This is again assumed to result from a Reynolds number dependency. In the surrog-

ate models, the spread from the wind-dependency is more or less averaged. This is because of the parameters chosen for the GPR. More specifically, the length-scale parameter and the alpha(noise)-parameter. The parameters are determined by trial-and-error to obtain smooth surfaces, and only account for the variance that is assumed to be reasonable for the behaviour of the ADs. The variance in the girder height direction is generally low, which has resulted in surfaces that are mostly linear in this direction. In the reduced velocity direction, the surfaces capture the trend for the different ADs quite well with the current GPR-parameters. It can, however, be discussed how much scatter the surfaces should "collect". This is hard to judge, while a physical interpretation of each AD is challenging, making it difficult to evaluate the surfaces validity for a particular choice of GPR-parameters. Regardless of the GPR-parameters, $A2^*$ seems to remain negative within the bounds of the surrogate model. Referring to Section 2.5.3, it can be concluded that dynamic instability in torsion will not occur for any of the configurations. Additionally, $H2^*$ is mostly negative, such that galloping can be judged unlikely to happen, except for the low girder height configurations. This is, referring to Section 2.5.2. Judging from the AD surrogate models, the most likely instability phenomenon is then flutter.

5.5 Optimization

The grid search, as described in section Section 3.7, was carried out to generate data for the optimization function. The generated data, displayed as sampling points in Figure 5.5, represents critical wind speed and total cost for 105 different configurations. The generated data is presented in table form in Appendix D. After the time-consuming process of generating data was completed, the optimization algorithm could be performed in a matter of seconds. A surrogate model was fitted to the sampling points with use of GPR. This resulted in predicted data for 2500 configurations, evenly distributed within the parameter ranges. The algorithm returns the optimal configuration with respect to the objective function, defined in Equation (3.4), passing its constraint, defined in Equation (3.3). As shown in Figure 5.5, the optimal design for the LN22 test range is $h_t = 220m$ and $h_g = 3.68m$, with *total cost* ≈ 2001 MNOK and $V_{cr} = 76.43$ m/s.

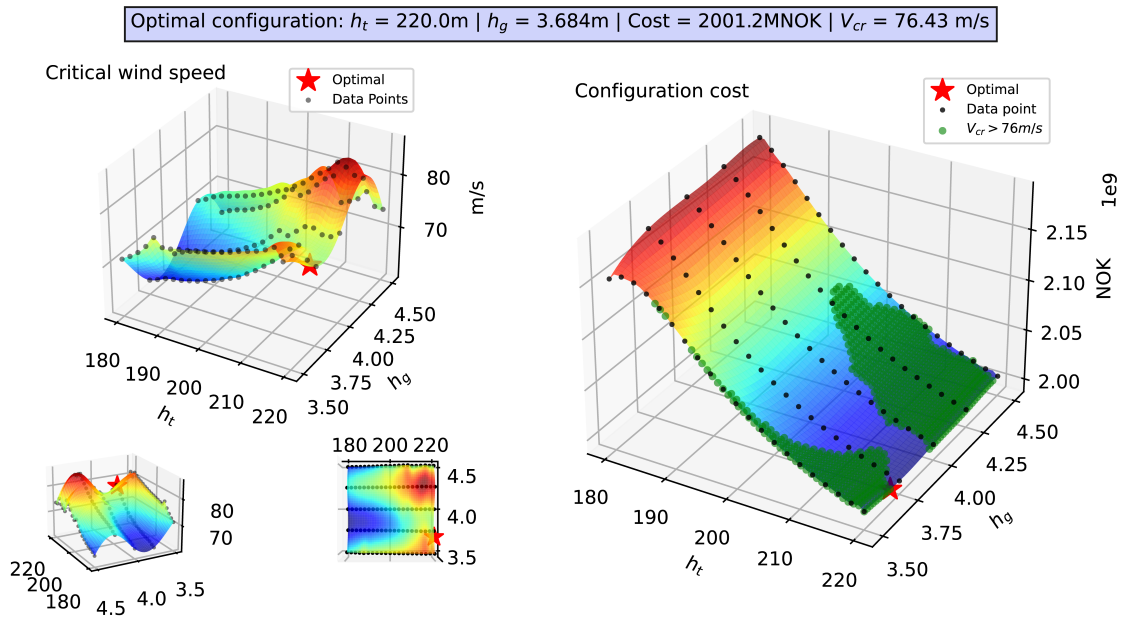


Figure 5.5: 3D-plots for the critical wind speed and configuration cost as function of tower and girder height. The green scatter plot depicts the configurations where $V_{cr} > 76\text{m/s}$.

Further investigation of the stability limit calculation confirmed what the AD data indicated; the instability phenomena determining the stability limit was flutter. Figure 5.6 is an Argand diagram showing the most contributing modes to the failure mode for $h_g = 3.68\text{m}$ and $h_t = 220\text{m}$. The length of each vector indicates the corresponding mode's relative contribution to the failure mode. The first symmetric torsional mode is the main contributor. The first, second, and third vertical symmetric modes are also significant contributors, as well as the first symmetric horizontal mode. It is to be expected that asymmetric modes will not couple when the main mode is symmetric while coupling is more likely when the mode shapes have a shape-wise similarity [12]. The instability can be concluded to be caused by multi-modal flutter.

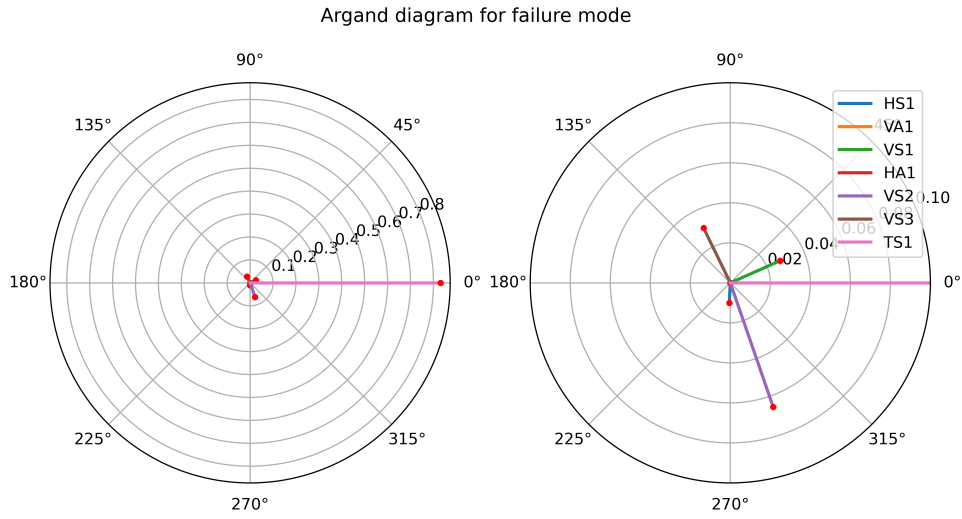


Figure 5.6: Argand diagram illustrating coupled the failure mode for $h_g = 3.68m$ and $h_t = 220m$. The plot to the right is an up-scaled version of the plot to the left.

For the total configuration cost, the main driving parameter is the tower height, whereas there is relatively little change in the total price as the girder height changes. Figure 5.7 shows the main cable force as a function of tower height. Lower tower height results in higher tensile forces in the main cables, which requires a bigger cable cross-section to limit the stress.

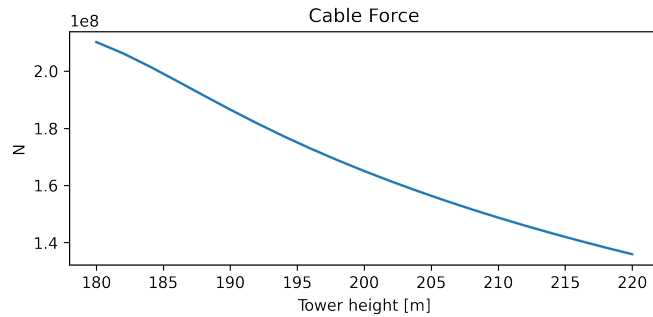


Figure 5.7: Cable force as function of tower height. Girder height = 4.0

Figure 5.8 shows the cost functions for each part within the parameter bounds. The aluminium girder is the main contributor to the total price. However, the girder cost function shows a negligible slope along the girder height axis, relative to the cable and tower cost along the tower height axis. The cable cost has a bigger slope than the tower cost and is therefore the factor controlling the total price slope in Figure 5.5. The hanger cost also shows little change with the parameters relative to the cable and tower cost.

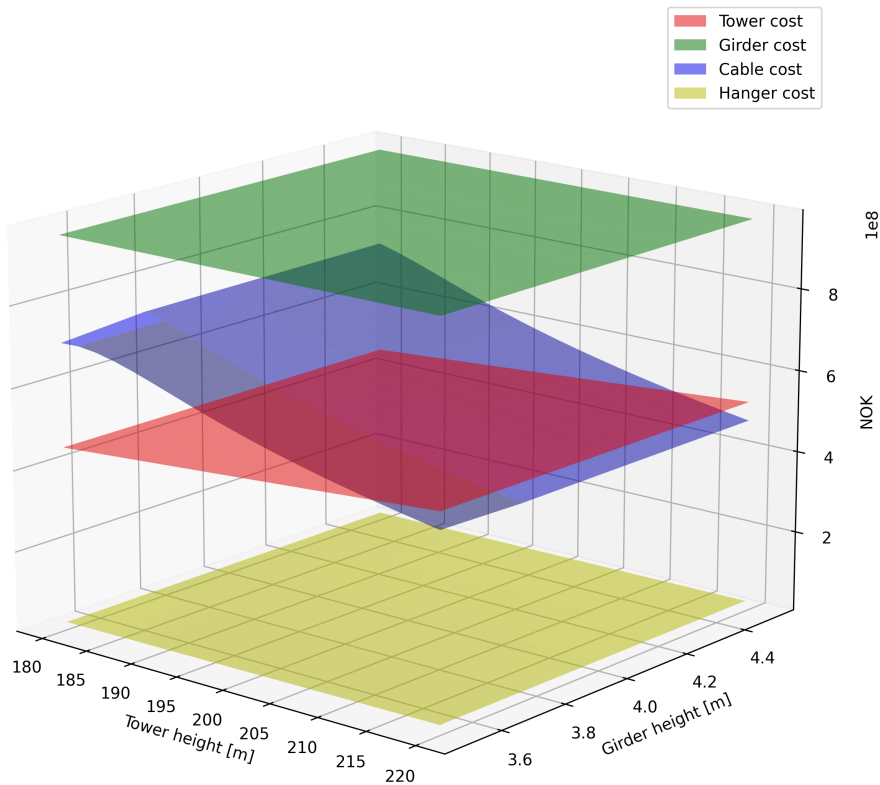


Figure 5.8: 3D-plot showing the cost per part for the Langenuen suspension bridge

Based on the surrogate models displayed in Figure 5.5, the optimization algorithm will seek configurations along the upper tower height bound. These configurations are preferable, both with regards to cost and stability limit. An argument is to be made that the upper tower height bound should be increased. Based on a study of the generated data, the slope of the configuration cost tends to flatten out towards the upper tower height bound. As does the slope of the critical wind speed. However, it appears likely that extending the tower height range by 10–20 meters will result in an even more optimal design configuration. Henceforth, it should be mentioned that an extension of the tower height range will bring even more uncertainty and unknown variables. For example, the optimization algorithm is not yet designed to include design changes when the towers reach higher.

5.6 Buffeting response

The buffeting response analysis was carried out for the optimal design configuration returned from the optimization. That is, $h_t = 220m$ and $h_g = 3.68m$. Plots of the corresponding frequency response functions, modal load spectra, and modal coordinate spectra is shown in Figure 5.9, 5.10 and 5.11, respectively. Note that they are plotted towards a logarithmic y-axis. The plots are generated at a mean along wind speed of 30 m/s, a turbulence intensity, I_u , of 0.10 and a mean attacking angle, $\bar{\alpha}$, of zero. These plots illustrate the modal contributions to the buffeting response.

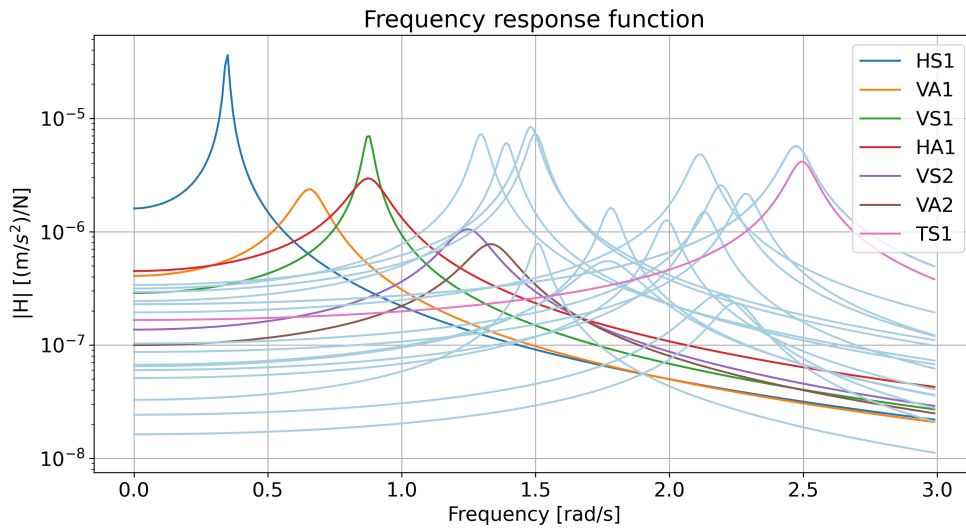


Figure 5.9: Plots of the modal frequency response function for $U = 30$ m/s

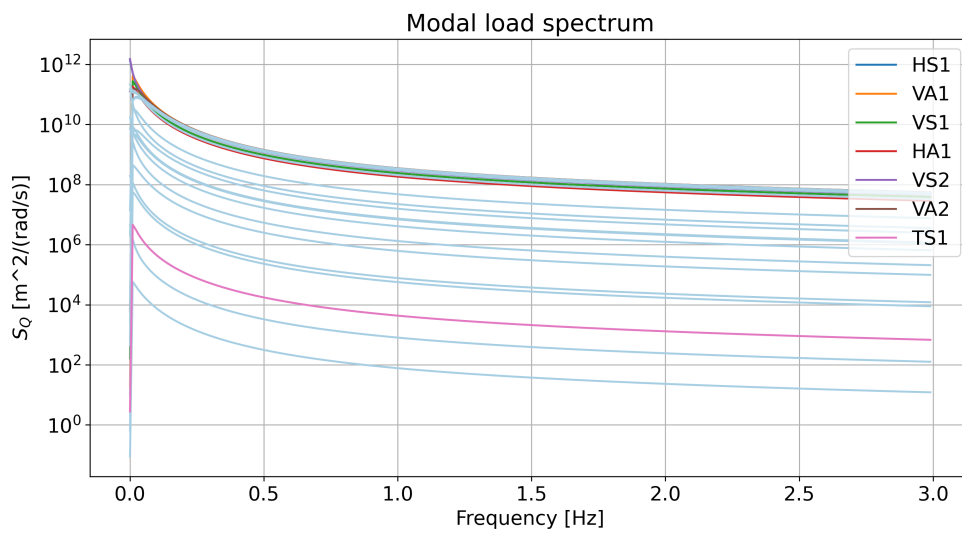


Figure 5.10: Plots of the modal load spectra for $U = 30$ m/s

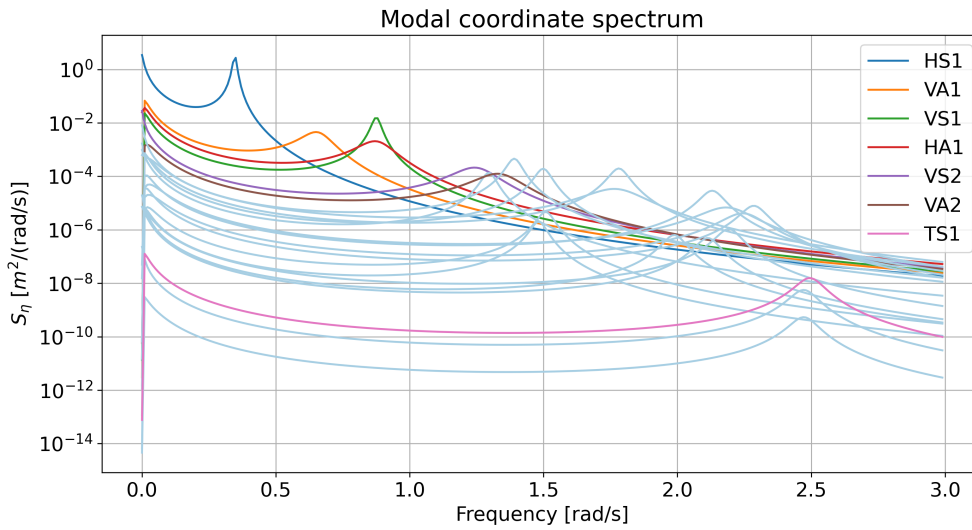


Figure 5.11: Plots of the modal coordinate spectra for $U = 30$ m/s

The root mean squared (RMS) of the modal contributions to the standard deviation are plotted towards the bridge longitudinal axis in Figure 5.12. This shows the expected standard deviations of the buffeting response for the three considered DOF-directions for a mean along wind velocity of 30 m/s. This does also give an indication of the mode shapes of the dominating modes.

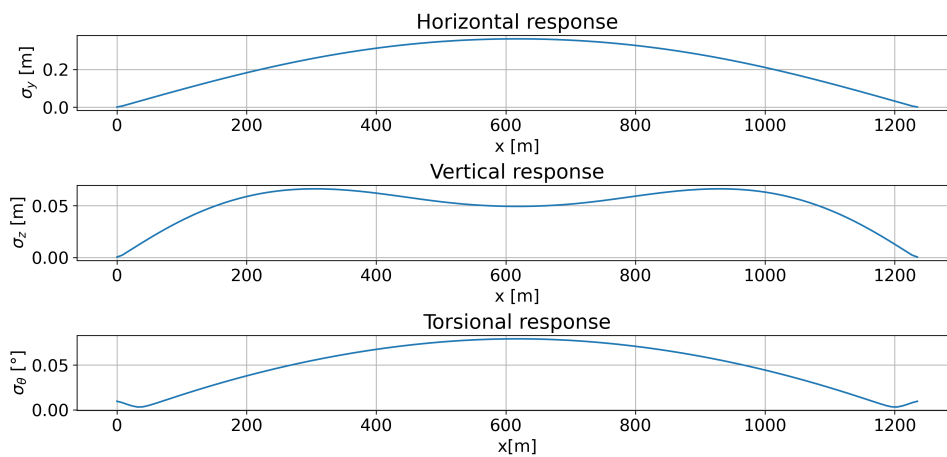


Figure 5.12: Plots of the maximum response along the bridge length for $U = 30$ m/s

Figure 5.13 shows the RMS standard deviations sensitivity to increasing mean wind velocity, turbulence intensity and mean attacking angle, respectively.

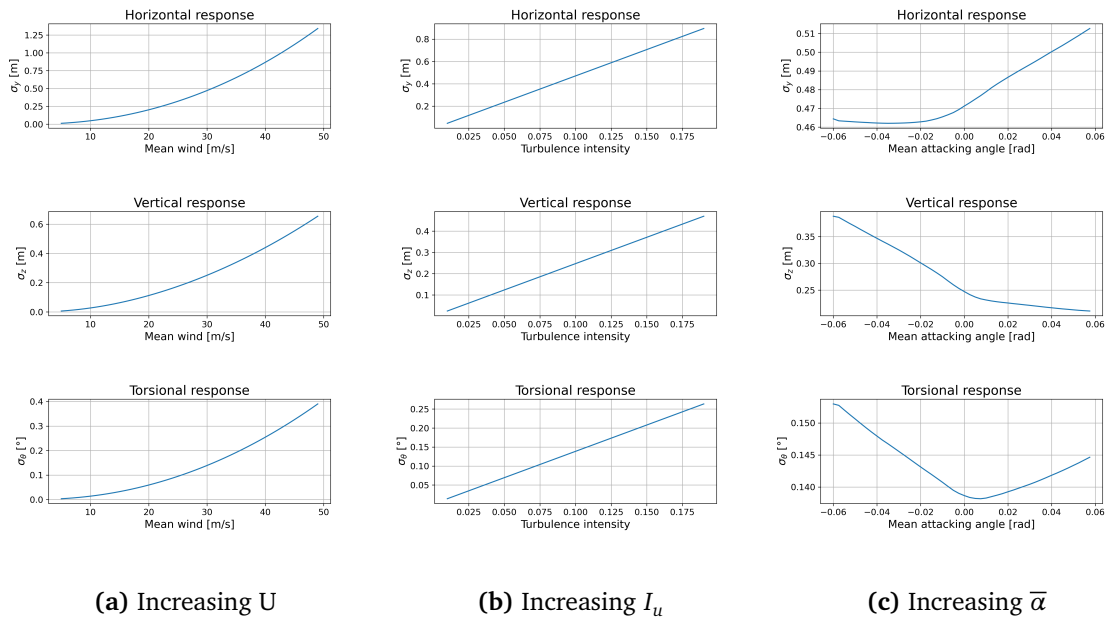


Figure 5.13: Sensitivity study of the spatial maximum standard deviation of the buffeting response

The horizontal buffeting response is dominated by the first mode, i.e. mode 1HS, with a maximum standard deviation of approximately 0.5 meters. The vertical buffeting response mainly results from modes VA1 and VS1, adding up to a standard deviation of about 0.07 meters. The torsional response is also dominated by the first horizontal mode, HS1. It can be seen from the mode visualizations in Appendix B that the horizontal modes also excite the torsional DOF's, in a shape-wise similar way, except for a counteraction near the supports of the girder. Looking at Figure 5.11, it is clear that the torsional mode, TS1, has a very small contribution to the response, keeping in mind that the y-axis is logarithmic. The torsional standard deviation is about 0.11° at its maximum. This information may be utilized to reveal where the girder is most vulnerable with regard to fatigue. The bending moment is at its maximum, where the curvature is largest [8]. High standard deviations together with large curvature in the dominating modeshape vectors indicate high bending moments, and thus bending stress variations.

In Figure 5.9, it can also be remarked that some of the modes have more rounded peaks, such as VA1, VS1, VA2, VS2, and to some extent TS1. This is due to the aerodynamic contributions, C_{ae} and K_{ae} to the total C and K matrices. The aerodynamic derivatives, that are dependent on the reduced velocity, change the structural properties and thus, the resonance frequencies. Therefore, the peaks in the FRF get smoothed out when plotted towards a frequency axis. It can also indicate coupling of modes, while C and K get significant contributions at the off-diagonal terms. However, it is still reasonable to believe that the original mode shapes are most dominant in the coupled mode shapes. Regardless, it is clear from the FRF-plots that the aerodynamic contributions are more significant for the vertical and torsional modes than for the horizontal modes.

5.7 Further discussions

In the Langenuen case study, there are some uncertainties in the cost and critical wind speed calculations for the various configurations. These are related to both the modal analysis in Abaqus and the data that is used to describe the aerodynamic properties of the different sections. Additionally, the cost estimations are quite simplified.

The critical wind speed calculation utilizes the eigenfrequencies, mode shapes, and modal masses which are extracted from the modal analysis. Multi-modal flutter is regarded as the most likely instability phenomenon, determining the stability limit for the configurations. As shown in Figure 5.6, the symmetrical torsional and vertical modes are the main participants in the flutter mode. Uncertainties in the stability limits should then mainly be related to the properties of these modes. In the calculation of cross-section properties, the panel geometry has been simplified. This may affect the stiffness properties I_{11} , I_{22} and I_t , as well as the girder's distributed mass. In particular, the torsional stiffness, I_t has been seen to influence the frequency of the torsional modes significantly. Looking at both Figure 5.5 and 5.1, there is a clear correlation between the increase in critical wind speed and the increase in ω_θ/ω_z -ratio. The tower height is the driving parameter for both frequencies. This is believed due to the big impact the tower height has on the force distribution, which again seems to have a great influence on the global stiffness. When changing the girder height parameter, the torsional frequency displays a small slope, whereas the vertical frequency seems to be relatively unaffected. To maximize the ω_θ/ω_z -ratio, increasing both tower and girder height seems beneficial within the defined bounds. The critical wind speed plot in Figure 5.5 follow more or less the same trend as the frequency ratio plot in Figure 5.1, and substantiates that a high ω_θ/ω_z -ratio is good for aerodynamic stability for suspension bridges [12].

The parametric cross-section model described in Section 3.3, is modeled as a thin-walled cross-section with an effective stiffness of 35 mm. Compared to Bredt's 2. formula, Abaqus calculates approximately 12 % higher torsional stiffnesses. While Bredt's 2 formula is referring to St. Venant torsion, the warping elements in Abaqus include a warping DOF, accounting also for warping torsion [31]. The torsional stiffness is not investigated in detail while the cross-section is, nevertheless, simplified as a thin-walled section. An accurate estimation of the section parameters of a transverse panel cross-section is a rather complicated exercise, and not the objective of this project. It is, however, revealed that a study of the torsional stiffness of a transverse panel cross-section is necessary to improve the accuracy of the calculation of the stability limit for the Langenuen concept.

Another topic of discussion is the system's structural damping. This can stem, for example, from strain or friction in the motion of the various modes, and will thus vary for each mode. In the Langenuen case study, the damping ratio was chosen to $\zeta = \frac{C_n}{C_{n,cr}} = 0.2\%$ for all modes, n. This is in accordance with the recommendations from *N400 Bruprosjektering* [3]. The system will turn unstable as the total damping $\zeta_n - \zeta_{n,ae}$ turns negative, and thus, the structural damping has a direct influence on the stability limit. The significance is dependent on whether the flutter, is so-called hard or soft, meaning if the absolute slope of the total damping is large or small in the area where it approaches zero. Since the structural damping appears as an offset on the y-axis at $V = 0$, this has a large influence on the stability limit if the flutter is soft. Figure 5.14 shows how the eigenfrequencies and total damping ratios typically develop with increasing wind speed. The plot summarizes the flutter analysis for a tower height of 220

meters and a girder height of 3.68 meters. Figure 5.15 illustrates the corresponding failure modes sensitivity to decreasing structural damping. Increasing the structural damping from 0.2 % to 0.5 % increases the calculated critical wind speed from 74 m/s to 80 m/s. Note that the mode combination here is only vertical symmetric modes, VS1, VS2 and VS3, as well as the first torsional mode, TS1. This results in a slightly lower stability limit than by combining all modes.

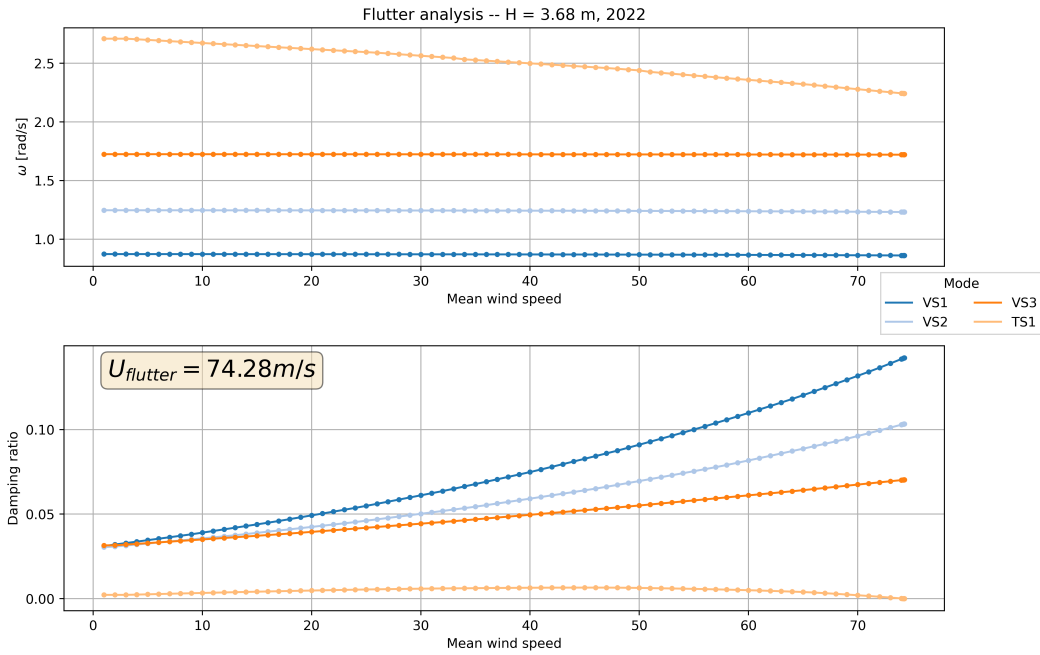


Figure 5.14: Total damping ratio and eigenfrequency for symmetric vertical and torsional modes

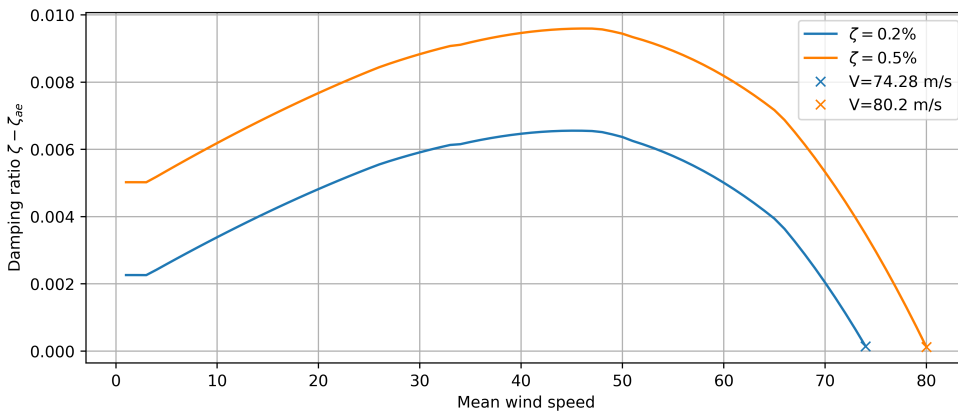


Figure 5.15: Total damping ratio plotted towards increasing mean wind speed

The structural damping is difficult to estimate analytically without response measurements

from the actual bridge. As a result, the stability limit is subject to significant uncertainty.

Uncertainty is also present in the wind-tunnel results that may have affected the stability limits. Even though there are no signs of systematic mistakes leading to errors during the testing, some general thoughts are made on this.

- Some wind speed dependency was observed, indicating that the forces are not completely linear with the wind speed.
- The least-square-fit approach that is used to extract the ADs from the load recording leaves some room for error. This is illustrated, e.g., by the scatter in some of the AD-data, which indicates that the method "struggles" to determine some of the AD values. However, this also indicates that these particular ADs have a small contribution to the measured load.
- Some general uncertainty can be expected from the test setup. This is illustrated by, e.g., the noise seen in the recordings, such as in Figure 3.10. However, this uncertainty seems to be relatively small.

From the wind-tunnel results, surrogate models for each AD were made, enabling the extraction of AD values for arbitrary reduced velocities and girder heights. This surface-fitting comes with an uncertainty that increases with the spacing of the data points. It can be seen from Figure 5.3 the sampling spacing with respect to reduced velocity is lowest in the range of approximately $V_{red} \in [0.9, 3.5]$. The flutter failure mode appears to be TS1 in the in-wind frequency range of $\omega_r \in [1.9, 2.3]$ for velocities between 63 m/s and 86 m/s. With $V_{red} = \frac{\bar{V}}{B\omega_r}$ it can be shown that this corresponds to approximately $V_{red} \in [1.0, 1.5]$ for certain configurations. The algorithm then occasionally picks ADs outside the test range of V_{red} , which introduces a little uncertainty. The other most contributing modes, VS1, VS2 and VS3, have in-wind frequencies down to approximately 0.9 rad/s, which corresponds to a reduced velocity beneath 3.0. The AD surrogate models have good accuracy in the most critical area, but it should be considered to add some higher frequencies in the forced vibration tests to get more data points in the lowest V_{red} -area. On the girder height axis, there is data in steps of 0.25 meters, leaving some uncertainty in the AD-values in-between. However, the figure also shows a lower variance along this axis, such that a relatively low confidence interval may be expected for the surrogate model in this dimension.

Figure 5.16 show three 2D-slices from the critical wind speed plot in Figure 5.5. For this example, it can be seen that girder heights around 3.85 m yield the lowest V_{cr} , and girder height at 3.5 m yields the highest critical wind speed for the lower and middle tower height range. For the upper tower height range, it's the girder heights of around 4.3 m that yield the highest critical wind speed. It is observed that the lower and middle tower heights share the same tendency, whereas a slight change is observed for the upper tower height range. It is also observed that both parameters can be changed to significantly affect the critical wind speed.

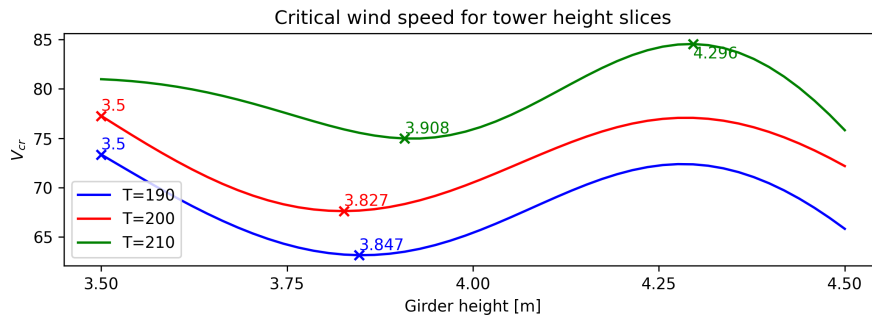


Figure 5.16: Plot showing 2D-slices for the critical wind speed taken at three different tower heights. The girder height with the highest and lowest V_{cr} are annotated

The tendencies in the critical wind speeds along the girder height axis in Figure 5.5 and Figure 5.16 cannot solely be explained by the change in cross-section parameters. These changes manifest themselves in Figure 5.1 and are observed to be linear and of relatively little significance. Therefore, the tendencies must stem from the ADs. A_2^* is considered as a potential contributor to this tendency. As shown in Equation (2.72), the AD is connected to torsional motion, which by Figure 5.6 is shown to be the main component in the flutter mode. Also, comparing the surrogate model and Figure 5.16, a shape-wise similarity with a negative correlation is to be observed. The same argument can be applied to H_2^* , which is shown to be connected to vertical motion.

Another phenomenon in the critical wind speed plot that cannot be explained by the changes in modal data, is the increasingly undulating tendency towards the uppermost bound in the tower heights. The reason behind this phenomenon could be many since it manifests itself over both axis. One thought is that the consistent increase in critical wind speed results in ADs being picked further up the reduced velocity axis. Here, the data points are more sparse and the discrepancies in AD-values are greater.

One can imagine that the approach of scaling down a bridge deck while exposing it to harmonic motion and reduced wind velocity comes with some uncertainty. The wind flow in the tunnel can to some extent be considered idealized. The turbulence intensity in the inlet is assumably about 0.2 %, which is quite low compared to the regulations for design that state a turbulence intensity of 10 % at the Langenuen site [13] [36]. One can expect a layer of the flow near the supporting points to be affected by the walls, but except for this, the flow can be considered as spatially constant along the section model. This is very unlikely in reality, judging from the turbulence co-spectra described in *N400 Bruprosjektering*. The roughness of the section model surface can influence the flow separation as well as the turbulence and vortex creation. However, this is rather complicated to perfectly reproduce on a model scale. Siedziako et.al. (2017) also address the interest in implementing some noise in the forced motion to approach a more realistic situation [13]. Wind-tunnel testing is all about determining the ADs and static coefficients, which is easier in more idealized conditions. It could, however, be interesting to investigate if more realistic conditions could provoke unexpected effects regarding the aerodynamic behavior.

By a mistake, the railing was scaled to 1:50, while the section models were scaled to 1:70. Provably, the railing has a very significant effect, especially on the drag force. How this appears

in the resulting stability limits is difficult to interpret directly from the results. However, it is known that the drag force is described by P_i^* for $i \in [1, 6]$ primarily influencing aerodynamic contributions on the horizontal modes, which are minor contributors to the failure modes. Nevertheless, the buffeting response is certainly affected by the increased drag force due to the scaling mistake. Even though the scaling mistake jeopardized the accuracy of the Langenuen case study, it emphasizes the significance of cross-sectional details in wind-tunnel testing and is consistent with the findings made by Siedziako et al. (2017) [38]. There is a potential in railing optimization regarding aerodynamic design.

The objective function, including the price functions, is highly simplified, leaving room for discussion regarding the result of the optimization. The price functions are based on estimations from a previous study on Langenuen by Dr. Techn Olav Olsen (2020) [27]. The estimations seem quite detailed on the girder, while more rough regarding the tower, cable, and hanger cost. One can also imagine these price functions being non-linear with respect to the material quantities, considering the complicated installation process. Nevertheless, it might be reasonable to consider them to be relatively linear within a certain range of the main parameters. Further investigations into the price functions should be prioritized to increase the credibility of the result from the optimization program.

Even though there are uncertainties in the results from the optimization of the Langenuen concept, the trends seen from Figure 5.5 are clear. Because of the expensive cable steel, one should consider a higher tower to lower the static forces in the main cables. A higher tower also tends to be beneficial considering aerodynamic stability. Throughout master projects at NTNU the later years, the suggestions have been to test lower and lower girders to reduce material use. The optimization program recommends a girder height of 3.68 meters, even though the stability criteria can be fulfilled down to 3.5 meters. This might indicate that a further reduction in the girder height might not be so interesting from a cost perspective.

Chapter 6

Conclusions

A program for suspension bridge concept optimization with respect to material cost and aerodynamic stability was successfully developed throughout this project. The program performs a grid search on configurations of the two main parameters, tower and girder height. Combining numerical calculations in Python and modal properties calculated with a parametric FE-model in Abaqus, the stability limits are obtained for the configurations. With an objective function representing the material cost, the optimal design is returned as the configuration corresponding to the minimum of the objective function, which simultaneously passes the stability criteria.

Aerodynamic optimization of suspension bridge concepts is traditionally regarded as a demanding exercise, while the aerodynamic properties of the cross-sections are most accurately found experimentally. This becomes a time- and cost-consuming process in a wind-tunnel as all the considered cross-section alternatives must be tested. By testing a range of sample sections, surrogate models of the aerodynamic derivatives were made with the use of Gaussian Process Regression. These were utilized in the optimization program to enable extraction of ADs for arbitrary girder heights within the sampling range.

The program performed successfully on a case study conducted on the Langenuen crossing; potentially the world's first suspension bridge with an aluminium girder. The returned cost-optimum showed a tower height of 220 meters and a girder height of 3.68 meters, which gave a critical wind speed of 76.4 m/s. Resulting plots shows clear trends of increasing stability limits and decreasing material cost with increasing tower heights. However, this comes with some uncertainty. This is especially regarding the surrogate models that are observed to be quite sensitive to GPR-parameters. It has also been confirmed that torsional stiffness and structural damping have a clear influence on the stability and should therefore be paid attention to, to assure trustable results. Additionally, the cost function should be improved to increase the accuracy of the optimization.

Even though there are uncertainties in the results, it has been proven that there is potential in this approach for optimizing suspension bridge concepts. It can be both time and cost-saving, by making the concept phase more effective, as well as potentially reducing material use with more optimal solutions. It can also help gaining general knowledge on aerodynamic suspension bridge design by exploring a wide range of design options. The program was adjusted to

optimize the Langenuen crossing, but can readily be implemented for other concept studies as well. With the work Øyvind Wiig Petersen has done on developing a parametric Abaqus model for suspension bridges, the applicability of the program is only limited by the available wind-tunnel data.

Chapter 7

Further work

The work on developing the optimization program throughout this project can be regarded as a pilot project. With Langenuen as an example, the program suggests an optimal configuration, but there is still significant uncertainty in the result. Potentially, additional variables can be parameterized as main input parameters to further optimize the concept. To improve the program's performance in aerodynamic optimization from a cost-perspective, the authors suggest prioritizing:

- Explore opportunities for utilizing machine learning to automatically choose and tune GPR-kernels for the surrogate models.
- Develop a database of wind-tunnel data to include additional cross-section parameters, such as inclination angle and railing alternatives, in the program.
- Add parameter dependencies, such as tower design, to improve the accuracy of the analysis.
- Implement more accurate cost functions.
- Make the program more user-friendly by gathering all inputs into a main script or GUI.

When adding n main parameters to the optimization, the grid expands by n dimensions and the number of iterations is drastically increased. In such a case, measures to keep the running time within reasonable limits may be necessary. This can be achieved by implementing a smarter optimization function such as constrained Bayesian Optimization, which enables equally accurate surrogate models in critical regions with fewer sampling points. Another opportunity is to speed up the FE-analysis by improving the implementation of Abaqus or switching to another self-made or commercial FE-software.

There is also a lot of potential for increasing the value of such a program by expanding its interface. Constraints like limited buffeting and static response can readily be implemented to get a more general concept optimization. Environmental impact is becoming a priority in today's infrastructure projects and can be implemented as a second objective function in the program, with a weighting against the cost to choose the best concept.

Bibliography

- [1] W.-F. Chen and L. Duan, Eds., *Bridge Engineering Handbook*, CRC, 2000.
- [2] N. J. Gimsing and C. T. Georgakis, *Cable Supported Bridges*. John Wiley & Sons, 2012.
- [3] NPRA, 'Håndbok N400 - Bruprosjektering,' p. 178, Jan. 2015. [Online]. Available: <https://www.vegvesen.no/globalassets/fag/handboker/hb-n400-bruprosjektering.pdf>.
- [4] NPRA. 'Ferjefri E39,' Statens vegvesen. (), [Online]. Available: <https://www.vegvesen.no/vegprosjekter/europaveg/ferjefrie39/> (visited on 31/05/2022).
- [5] P. Gülkan, A. Caner and N. Memisoglu Apaydin, Eds., *Developments in International Bridge Engineering: Selected Papers from Istanbul Bridge Conference 2018*, vol. 17, Springer Tracts on Transportation and Traffic, Cham: Springer International Publishing, 2021, ISBN: 978-3-030-59168-7 978-3-030-59169-4. DOI: 10.1007/978-3-030-59169-4. [Online]. Available: <https://link.springer.com/10.1007/978-3-030-59169-4> (visited on 24/05/2022).
- [6] Z.-F. Fu and J. He, *Modal Analysis*. Elsevier, 4th Sep. 2001, 305 pp., Google-Books-ID: ElwhqUtJUj8C, ISBN: 978-0-08-051178-8.
- [7] A. K. Chopra, *Dynamics of Structures*. Pearson Education, Sep. 2007, 916 pp., Google-Books-ID: OdU1bDaRyP4C, ISBN: 978-81-317-1329-7.
- [8] K. Bell, *An engineering approach to finite element analysis of linear structural mechanics problems*. Fagbokforlaget, 2013. (visited on 27/01/2022).
- [9] X. Wang, *Frequency Analysis of Vibration Energy Harvesting Systems*. Academic Press Inc., 2016. (visited on 01/02/2022).
- [10] H. Holden, *fouriertransformen*, in *Store norske leksikon*, 28th Nov. 2019. [Online]. Available: <http://snl.no/fouriertransformen> (visited on 24/01/2022).
- [11] D. E. Newland, *Introduction to Random Vibrations, Spectral & Wavelet Analysis*, Third Edition, 3. Dover Publications Inc., 2005, 477 pp., ISBN: 978-0-486-44274-7.
- [12] E. N. Strømmen, *Theory of bridge aerodynamics*, 2nd ed. Berlin ; New York: Springer, 2010, 302 pp., OCLC: ocn660060098, ISBN: 978-3-642-13659-7.
- [13] B. Siedziako, O. Øiseth and A. Rønquist, 'An enhanced forced vibration rig for wind tunnel testing of bridge deck section models in arbitrary motion,' *Journal of Wind Engineering and Industrial Aerodynamics*, vol. 164, pp. 152–163, 2017, ISSN: 0167-6105. DOI: 10.1016/j.jweia.2017.02.011. [Online]. Available: <https://www.sciencedirect.com/science/article/pii/S0167610516307498> (visited on 03/02/2022).
- [14] T. J. A. Agar, 'Aerodynamic flutter analysis of suspension bridges by a modal technique,' *Engineering Structures*, vol. 11, no. 2, pp. 75–82, 1st Apr. 1989, ISSN: 0141-0296. DOI: 10.1016/0141-0296(89)90016-3. [Online]. Available: <https://www.sciencedirect.com/science/article/pii/0141029689900163> (visited on 24/05/2022).

- [15] O. Øiseth, A. Rönnquist and R. Sigbjörnsson, ‘Simplified prediction of wind-induced response and stability limit of slender long-span suspension bridges, based on modified quasi-steady theory: A case study,’ *Journal of Wind Engineering and Industrial Aerodynamics*, vol. 98, no. 12, pp. 730–741, 1st Dec. 2010, ISSN: 0167-6105. DOI: 10.1016/j.jweia.2010.06.009. [Online]. Available: <https://www.sciencedirect.com/science/article/pii/S0167610510000711> (visited on 04/06/2022).
- [16] K. A. Kvåle, R. Sigbjörnsson and O. Øiseth, ‘Modelling the stochastic dynamic behaviour of a pontoon bridge: A case study,’ *Computers & Structures*, vol. 165, pp. 123–135, 1st Mar. 2016, ISSN: 0045-7949. DOI: 10.1016/j.compstruc.2015.12.009. [Online]. Available: <https://www.sciencedirect.com/science/article/pii/S004579491500334X> (visited on 28/05/2022).
- [17] Y. J. Ge and H. Tanaka, ‘Aerodynamic flutter analysis of cable-supported bridges by multi-mode and full-mode approaches,’ *Journal of Wind Engineering and Industrial Aerodynamics*, vol. 86, no. 2, pp. 123–153, 1st Jun. 2000, ISSN: 0167-6105. DOI: 10.1016/S0167-6105(00)00007-6. [Online]. Available: <https://www.sciencedirect.com/science/article/pii/S0167610500000076> (visited on 27/05/2022).
- [18] C. E. Rasmussen and C. K. I. Williams, *Gaussian processes for machine learning*, ser. Adaptive computation and machine learning. Cambridge, Mass: MIT Press, 2006, 248 pp., OCLC: ocm61285753, ISBN: 978-0-262-18253-9.
- [19] J. Wang, ‘An intuitive tutorial to gaussian processes regression,’ *arXiv:2009.10862 [cs, stat]*, 1st Feb. 2021. arXiv: 2009.10862. [Online]. Available: <http://arxiv.org/abs/2009.10862> (visited on 19/04/2022).
- [20] J. Wang, ‘An intuitive tutorial to gaussian processes regression,’ *arXiv:2009.10862 [cs, stat]*, 1st Feb. 2021. arXiv: 2009.10862. [Online]. Available: <http://arxiv.org/abs/2009.10862> (visited on 09/02/2022).
- [21] ‘Sklearn.gaussian_process.kernels.RBF,’ scikit-learn. (), [Online]. Available: https://scikit-learn/stable/modules/generated/sklearn.gaussian_process.kernels.RBF.html (visited on 19/04/2022).
- [22] M. L. Stein, *Interpolation of Spatial Data*, ser. Springer Series in Statistics. New York, NY: Springer, 1999, ISBN: 978-1-4612-7166-6 978-1-4612-1494-6. DOI: 10.1007/978-1-4612-1494-6. [Online]. Available: <http://link.springer.com/10.1007/978-1-4612-1494-6> (visited on 19/04/2022).
- [23] ‘Sklearn.gaussian_process.kernels.matern,’ scikit-learn. (), [Online]. Available: https://scikit-learn/stable/modules/generated/sklearn.gaussian_process.kernels.Matern.html (visited on 19/04/2022).
- [24] ‘Optimization and root finding (scipy.optimize) — SciPy v1.8.1 manual.’ (), [Online]. Available: <https://docs.scipy.org/doc/scipy/reference/optimize.html> (visited on 23/05/2022).
- [25] R. H. Byrd, S. L. Hansen, J. Nocedal and Y. Singer, ‘A stochastic quasi-newton method for large-scale optimization,’ *SIAM Journal on Optimization*, vol. 26, no. 2, pp. 1008–1031, Jan. 2016, Publisher: Society for Industrial and Applied Mathematics, ISSN: 1052-6234. DOI: 10.1137/140954362. [Online]. Available: <https://epubs.siam.org/doi/abs/10.1137/140954362> (visited on 23/05/2022).
- [26] P. I. Frazier, ‘Bayesian optimization,’ in *Recent Advances in Optimization and Modeling of Contemporary Problems*, ser. INFORMS TutORials in Operations Research, Section: 11, INFORMS, Oct. 2018, pp. 255–278, ISBN: 978-0-9906153-2-3. DOI: 10.1287/educ.

- 2018.0188. [Online]. Available: <https://pubsonline.informs.org/doi/abs/10.1287/educ.2018.0188> (visited on 19/04/2022).
- [27] D. T. O. Olsen, 'Langenuen suspension bridge: Aluminium bridge girder alternative,' Statens Vegvesen, 20th Jun. 2020.
- [28] V. Studio. 'Visual studio code - code editing. redefined.' (), [Online]. Available: <https://code.visualstudio.com/> (visited on 30/03/2022).
- [29] Simulia. 'AbaqusAnalysis user's manual (6.9).' (), [Online]. Available: <http://130.149.89.49:2080/v6.9/books/usb/default.htm?startat=pt06ch25s03alm09.html> (visited on 27/01/2022).
- [30] RWDI, 'Langenuen suspension bridge,' 2021.
- [31] Simulia. 'ABAQUSTheory manual (v6.6).' (), [Online]. Available: <https://classes.engineering.wustl.edu/2009/spring/mase5513/abaqus/docs/v6.6/books/stm/default.htm?startat=ch03s05ath78.html#stm-elm-meshedsections> (visited on 22/04/2022).
- [32] '1.7. gaussian processes,' scikit-learn. (), [Online]. Available: https://scikit-learn/stable/modules/gaussian_process.html (visited on 25/04/2022).
- [33] E. Cheynet, J. B. Jakobsen and J. Snæbjörnsson, 'Buffeting response of a suspension bridge in complex terrain,' *Engineering Structures*, vol. 128, pp. 474–487, 1st Dec. 2016, ISSN: 0141-0296. DOI: 10.1016/j.engstruct.2016.09.060. [Online]. Available: <https://www.sciencedirect.com/science/article/pii/S0141029616307660> (visited on 07/05/2022).
- [34] R. H. Scanlan, 'The action of flexible bridges under wind, II: Buffeting theory,' *Journal of Sound and Vibration*, vol. 60, no. 2, pp. 201–211, 22nd Sep. 1978, ISSN: 0022-460X. DOI: 10.1016/S0022-460X(78)80029-7. [Online]. Available: <https://www.sciencedirect.com/science/article/pii/S0022460X78800297> (visited on 07/05/2022).
- [35] J. C. Kaimal, J. C. Wyngaard, Y. Izumi and O. R. Coté, 'Spectral characteristics of surface-layer turbulence,' *Quarterly Journal of the Royal Meteorological Society*, vol. 98, no. 417, pp. 563–589, 1972, eprint: <https://onlinelibrary.wiley.com/doi/pdf/10.1002/qj.49709841707>, ISSN: 1477-870X. DOI: 10.1002/qj.49709841707. [Online]. Available: <https://onlinelibrary.wiley.com/doi/abs/10.1002/qj.49709841707> (visited on 08/05/2022).
- [36] S. Norge. 'NS-EN 1991-1-4:2005+NA:2009: Eurocode 1: Actions on structures - part 1-4: General actions - wind actions.' (2009), [Online]. Available: <https://www.standard.no/no/Nettbutikk/produktkatalogen/Produktpresentasjon/?ProductID=392208> (visited on 08/05/2022).
- [37] K. Matsuda, K. R. Cooper, H. Tanaka, M. Tokushige and T. Iwasaki, 'An investigation of reynolds number effects on the steady and unsteady aerodynamic forces on a 1:10 scale bridge deck section model,' *Journal of Wind Engineering and Industrial Aerodynamics*, 10th International Conference on Wind Engineering, vol. 89, no. 7, pp. 619–632, 1st Jun. 2001, ISSN: 0167-6105. DOI: 10.1016/S0167-6105(01)00062-9. [Online]. Available: <https://www.sciencedirect.com/science/article/pii/S0167610501000629> (visited on 15/05/2022).
- [38] B. Siedziako and O. Øiseth, 'On the importance of cross-sectional details in the wind tunnel testing of bridge deck section models,' *3145-3151*, 2017, Accepted: 2018-01-30T09:54:49Z Publisher: Elsevier, ISSN: 1877-7058. DOI: 10.1016/j.proeng.2017.09.573. [Online]. Available: <https://ntnuopen.ntnu.no/ntnu-xmlui/handle/11250/2480585> (visited on 31/05/2022).

Appendix A

Optimize Program

The program is attached in a digital appendix. Link to GitHub-repository: [Click here.](#)

A.1 User manual

A.1.1 Overview

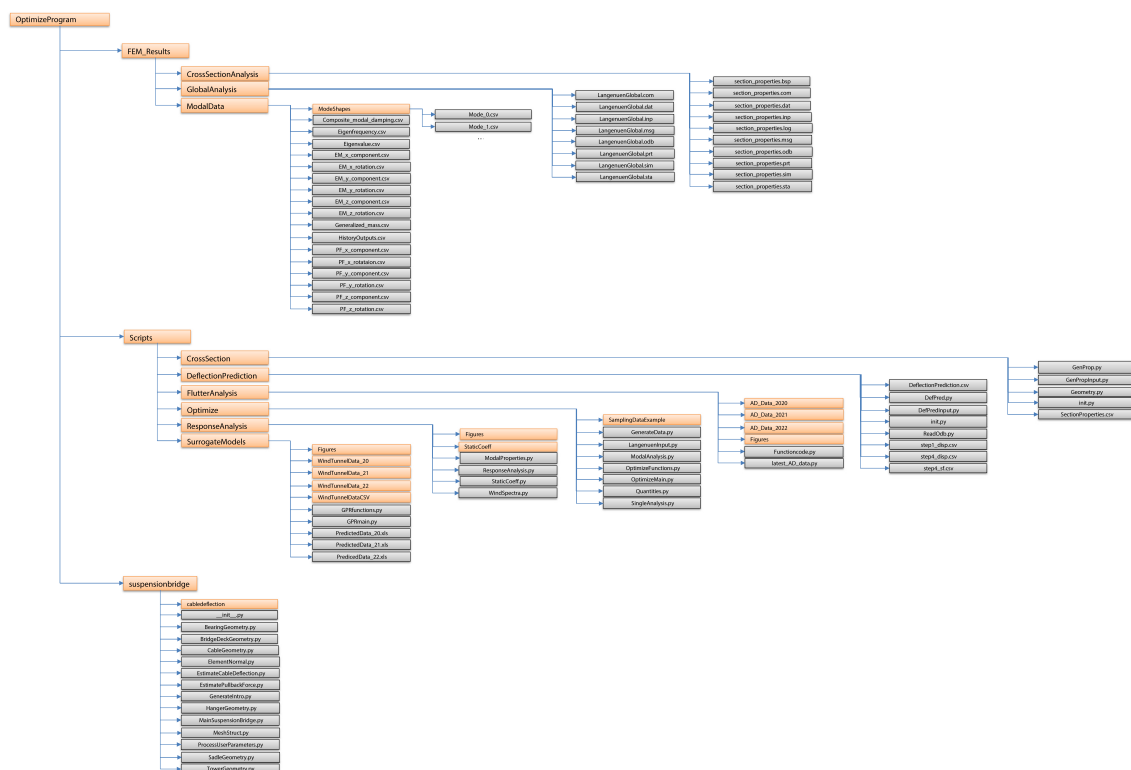


Figure A.1: General overview of the structure of the program.

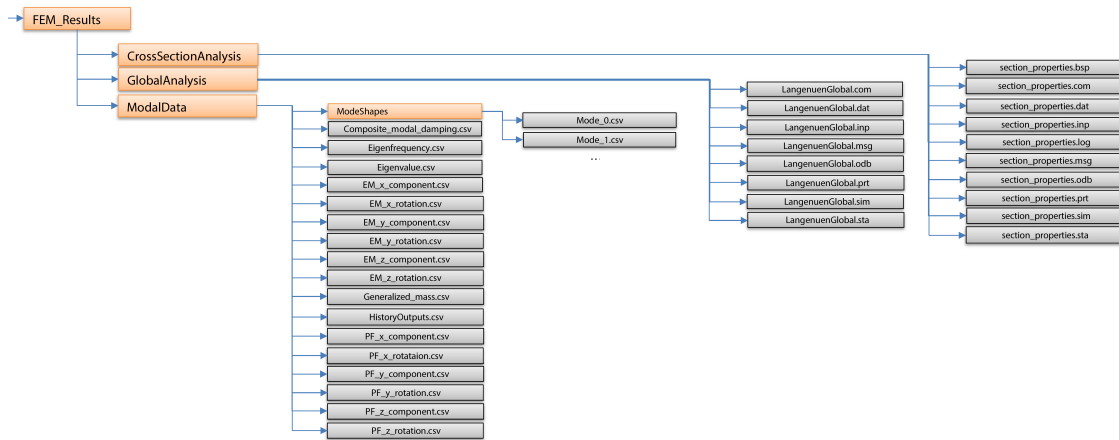


Figure A.2: The FEM_Results folder.

FEM_Results/ All the results from the Abaqus FE-analysis is stored in this folder.

CrossSectionAnalysis/ Collection of files generated by the latest cross-section analysis in Abaqus

GlobalAnalysis/ Collection of the files generated by the latest global analysis in Abaqus.

ModalData/ Modal properties for the latest configuration of which the *Pull_modeshapes.py* and *Pull_ModalData.py* are ran from a *LangenuenGlobal.odb*.

Modeshapes/ csv-files for the modeshapes, structured
 $nodenumber, x_{disp}, x_{rot}, y_{disp}, y_{rot}, z_{disp}, z_{rot}$

Eigenfrequency.csv csv-file for all the modal eigenfrequencies, structured
 $modenumber, \omega_n [rad/s]$

Generalized_mass.csv csv-file for all the modal masses structured
 $modenumber, \tilde{M}_n [kg]$

PF_i csv-file for all the modal participation factors in DOF i, structured
 $modenumber, PF_n$

EM_i csv-file for all the modal effective masses in DOF i, structured
 $modenumber, EM_n$

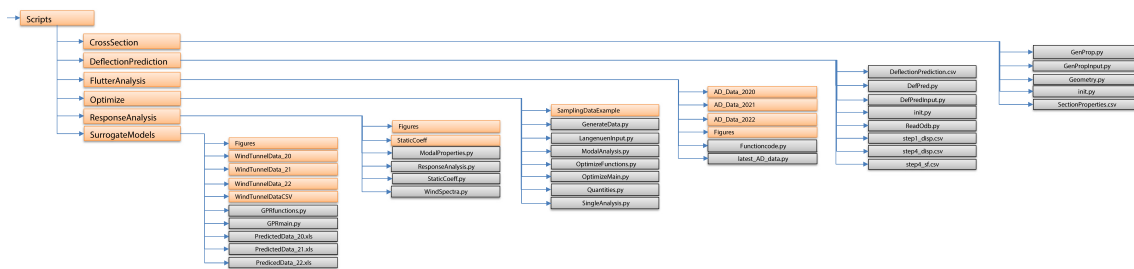


Figure A.3: The Scripts folder.

Scripts/ collection of the scripts carrying out the opti

CrossSection/ scripts carrying out the parametrized girder section analysis

GenProp.py contains the functions for writing to an input script, running the analysis, as well as reading and storing the desired section properties. It also contains the function that is used later to interpolate section properties.

GenPropInput.py the file that is sent to the Abaqus FEA

Geometry.py parametrization of the girder section. Primarily for plotting and visualizing the girder shapes.

init.py looping through the desired range of cross-sections, analysing them and storing the corresponding properties

SectionProperties.csv the storage of the section properties which are later to be used for interpolation to get the properties for arbitrary girder height.

DeflectionPrediction/ scripts to carry out the global analyses to determine static deflections and forces for a given configuration.

DeflectionPrediction.csv the storage of the predicted static deflections as well as the maximum cable- and hanger forces for different configurations. Later used to interpolate input variables for arbitrary configuration.

DefPred.py contains the function for writing to an input script, running the analysis, as well as reading and storing the desired static- deflections and forces. Also contains the function that is used later to interpolate deflections and forces.

DefPredInput.py the file that is sent to the Abaqus FEA

init.py double loop, looping through the desired range of cross-sections and tower heights, analysing them and storing the corresponding deflections and forces

ReadOdb script sent to the Abaqus interpreter to read the latest odb-file

step1_disp.csv csv-file containing the nodal displacements for the static step 1

step4_disp.csv csv-file containing the nodal displacements for the static step 4

step4_sf.csv csv-file containing the nodal forces for the static step 4

FlutterAnalysis/ scripts to carry out the stability limit calculation for a given configuration

AD_Data_y/ csv-files containing AD values extrapolated from the surrogate models from wind-tunnel tests in year, y

Figure/s figures that are automatically generated if plot=True in *Functioncode.flutter_speed*

Functioncode.py the function calculating the stability limit for a given configuration. Pulls AD-data from *AD_Data_y* and modal data from *FEM_Results/ModalData*

latest_AD_data csv-file containing the latest AD-data used in the stability limit calculation. If AD-data is not found for the given girder height, the data in *latest_AD_data.csv* is interpolated.

Optimize/ the main folder controlling the optimization

SamplingDataExample/ csv-files containing stability limits and cost for an example grid of configurations

GenerateData.py double loop, running the constraint function (stability limit) and objective function (cost) for a chosen grid of configurations

LangenuenInput.py input file for the modal analysis in Abaqus.

ModalAnalysis.py functions that writes input parameters to *LangenuenInput.py* and runs this. Uses interpolated values of cross-section properties and static deflections and forces from *SectionProperties.csv* and *DeflectionPrediction.csv* for a given configuration.

OptimizeFunctions.py the constraint and objective function, as well as the optimizing algorithm.

OptimizeMain.py function that initiates the optimizing algorithm based on generated sampling data such as in *SamplingDataExample*

Quantities.py scripts to calculate the material quantities for a configuration, which are utilized to calculate the objective function in *OptimizeFunctions.py*

SingleAnalysis.py function to calculate the stability limit of a single configuration. Made to run examples.

ResponseAnalysis/ scripts to calculate the buffeting response of a configuration

Figures/ figures that are automatically generated if `plot=True` in *ResponseAnalysis.ResponseAnalysis*

StaticCoeff/ xls-files containing static coefficient wind-tunnel data from 2020, 2021 and 2022

ModalProperties.py functions utilizing AD surrogate models to assemble in-wind M, C and K matrices

ResponseAnalysis.py function calculating the buffeting response of a configuration utilizing frequency domain analysis

StaticCoeff.py function that pulls the static coefficients and their derivatives for an arbitrary girder height within the test range, based on linear interpolation of girder heights

WindSpectra.py functions defining the turbulence spectra (Kaimal spectra) with the approach described in *N400 Bruprosjektering*

SurrogateModels/ functions creating surrogate models for AD-data based on wind-tunnel data

Figures/ figures of the 3D surrogate models created in *GPRmain.py*

WindTunnelData_y/ wind-tunnel data from year, y. xls-files of ADs for reduced velocities.

WindTunnelDataCSV/ csv-files with values from the surrogate models created in *GPRmain.py*

GPRfunctions functions creating the surrogate models based on data in *WindTunnelData_y* .xls-files, as well as functions to create figures

GPRmain.py initiates *GPRfunctions.py*

PredictedData_y.xls xls-files with the same data as in *WindTunnelDataCSV*. Used only for a better overview than with only csv-files.

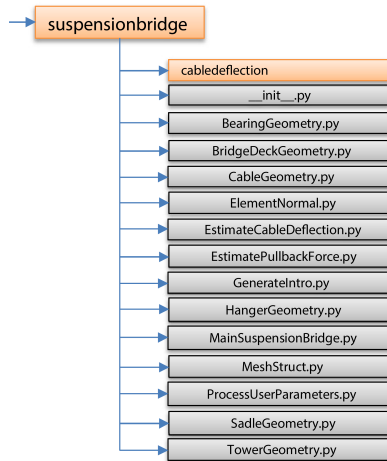


Figure A.4: The suspensionbridge folder

suspensionbridge/ folder containing all necessary scripts to establish and run the parametric suspension bridge model in Abaqus FEA. Developed by Øyvind Wiig Petersen.

A.1.2 How to run

A guide on how to run the program is listed below. Minor adjustments might be necessary to implement and run optimization for new data, while the functions are not yet completely generalized. Further description may be found in the scripts.

1. Set constant parameters in global analysis

The global analysis is based on a parametric FE-model in Abaqus. Geometric inputs customizing your suspension bridge must be set in **both** *Scripts/DeflectionPrediction/DefPredInput.py* and *Scripts/Optimize/LangenuenInput.py*. These input files are built up equally, but runs in the purpose of static deflections and modal properties, respectively.

2. Parametrize your cross-section

Make a parametrization of your cross-section based on corner coordinates and past this in to *GenPropInput.py*. Existing parametrization may also be used (p_type = [2020, 2021, 2022])

3. Initiate cross-section analysis

Set cross-section range and loop through this in *Scripts/CrossSection/init.py*. The results will be written to *SectionProperties.csv* for later use.

4. Initiate static deflection analysis

Set your range and run the double loop of configurations in *Scripts/DeflectionPrediction/init.py*. The results will be written to *DeflectionPrediction.csv*

5. Prepare your AD surrogate models

Load your AD-data as xls-files in the same way as in e.g. *Scripts/SurrogateModels/WindTunnelData_22*. Run *GPRmain.py* to generate the models.

6. Run the grid search

Set your ranges and run the double loop in *Scripts/Optimize/GenerateData.py*. Results will then be written to csv-files which are later to be utilized in a GPR of the constraint functions as well as the objective function.

7. Run the optimization function

Run *Scripts/Optimize/OptimizeMain.py* to execute the optimization algorithm returning the optimal configuration of tower height and girder height for a chosen stability criteria (V_{cr})

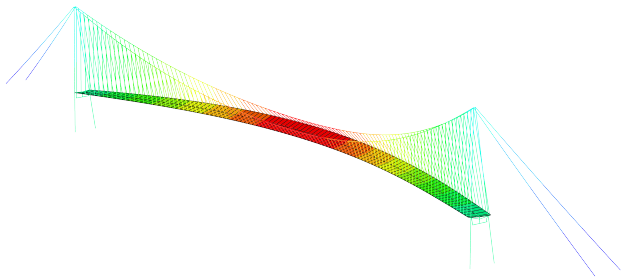
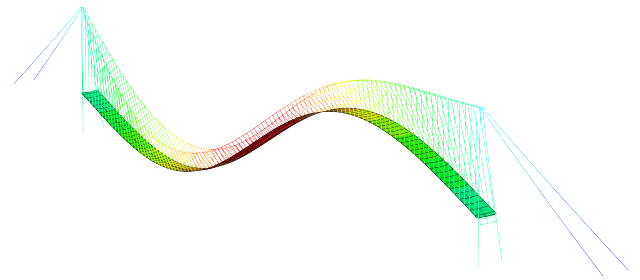
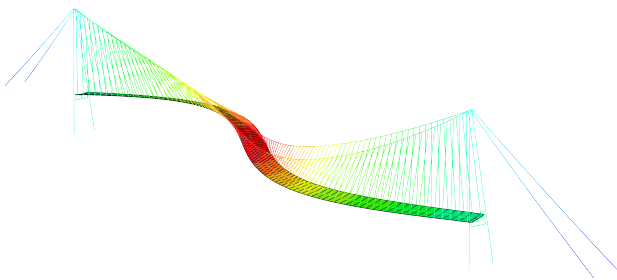
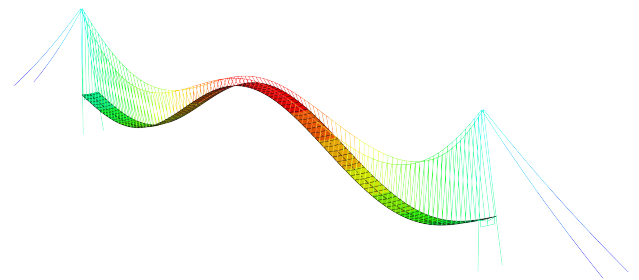
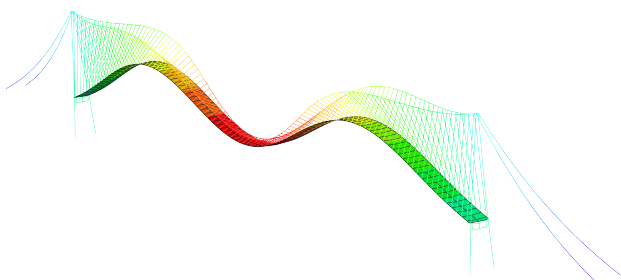
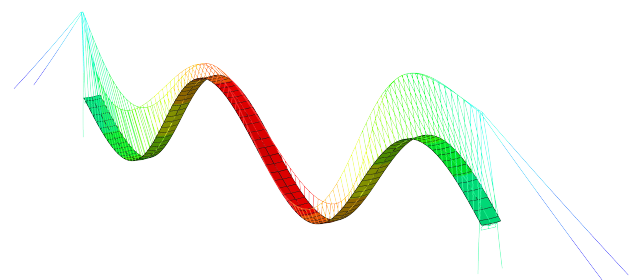
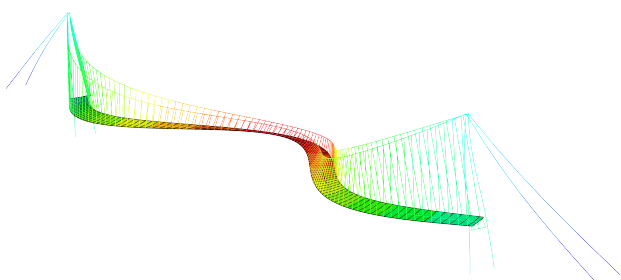
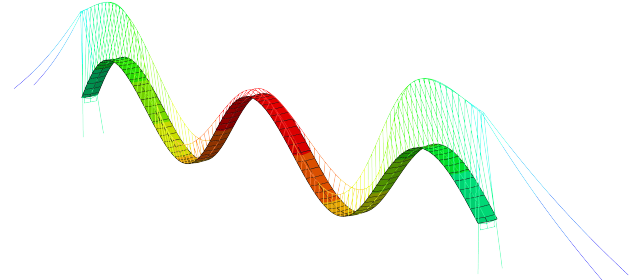
8. Calculate buffeting response

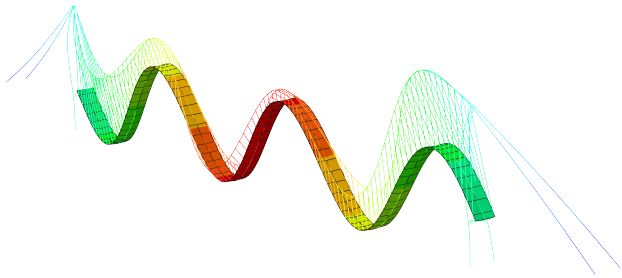
Load wind-tunnel data for static coefficients as the xls-files in *Scripts/ResponseAnalysis/StaticCoeff*. Run *ResponseAnalysis.py* for the chosen configuration. Make sure that the correct modal data is available i.e. by running *Scripts/Optimize/SingleAnalysis.py* for the same configuration prior to the *ResponseAnalysis.py*.

Appendix B

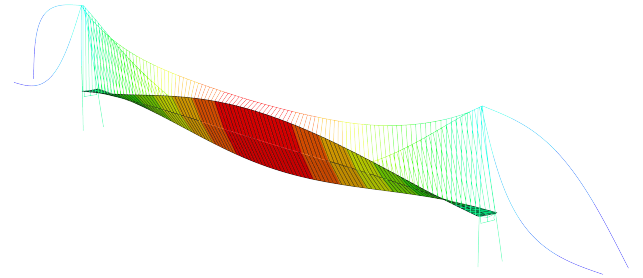
Modal analysis

Results for the modal analysis for the optimal design configuration $h_t = 220\text{m}$, $h_g = 3.68\text{m}$ is presented in this appendix.

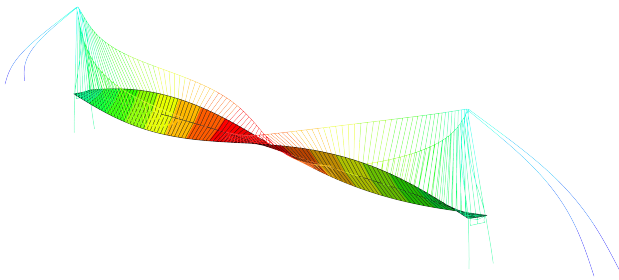
B.1 Mode shapes**(a) HS1****(b) VA1****(c) HA1****(d) VS1****(e) VS2****(f) VA2****(g) HS2****(h) VS3**



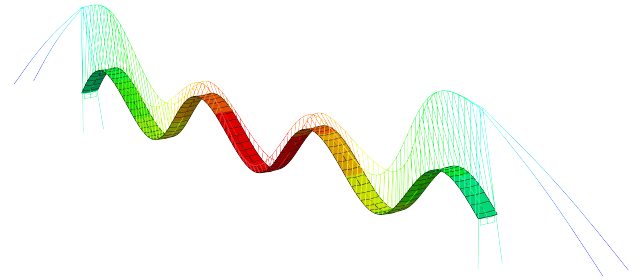
(a) VA3



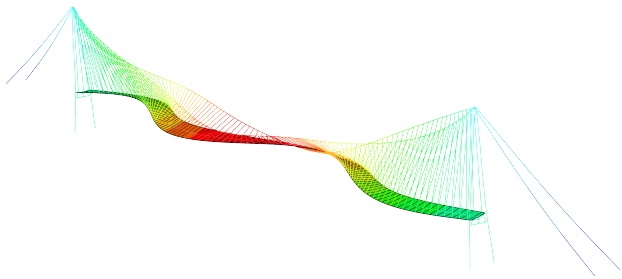
(b) TS1



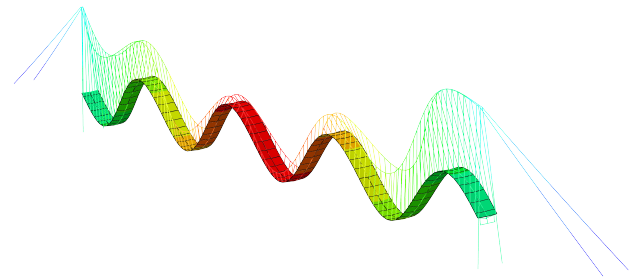
(c) TA1



(d) VS4







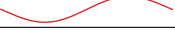













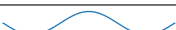




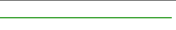




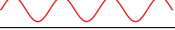
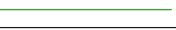

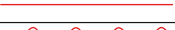










(e) HA2



(f) VA4

B.2 Modal properties

Table B.1: Modal properties for the optimal design configuration. $h_t = 220\text{m}$, $h_g = 3.68\text{m}$

Mode	Abaqus no.	Generalized mass \tilde{M}_i [kg]	Frequency [Hz]	Horizontal	Vertical	Torsional
HS1	1	10203440	0.0551			
VA1	2	11093105	0.1046			
VS1	3	5681536	0.1389			
HA1	4	8959294	0.1399			
VS2	5	8964031	0.1985			
VA2	7	10985696	0.2087			
VS3	12	9198672	0.2746			
HS2	13	9471826	0.2846			
VA3	15	11457903	0.3364			
TS1	23	4267371	0.3963			
VS4	29	10086643	0.4125			
TA1	30	5912600	0.4140			
VA4	34	10378214	0.4927			
HA2	37	8483582	0.5105			

Appendix C

Wind-tunnel results

C.1 ADs: sampling data

Results from the post-processed wind-tunnel data is presented in this appendix.

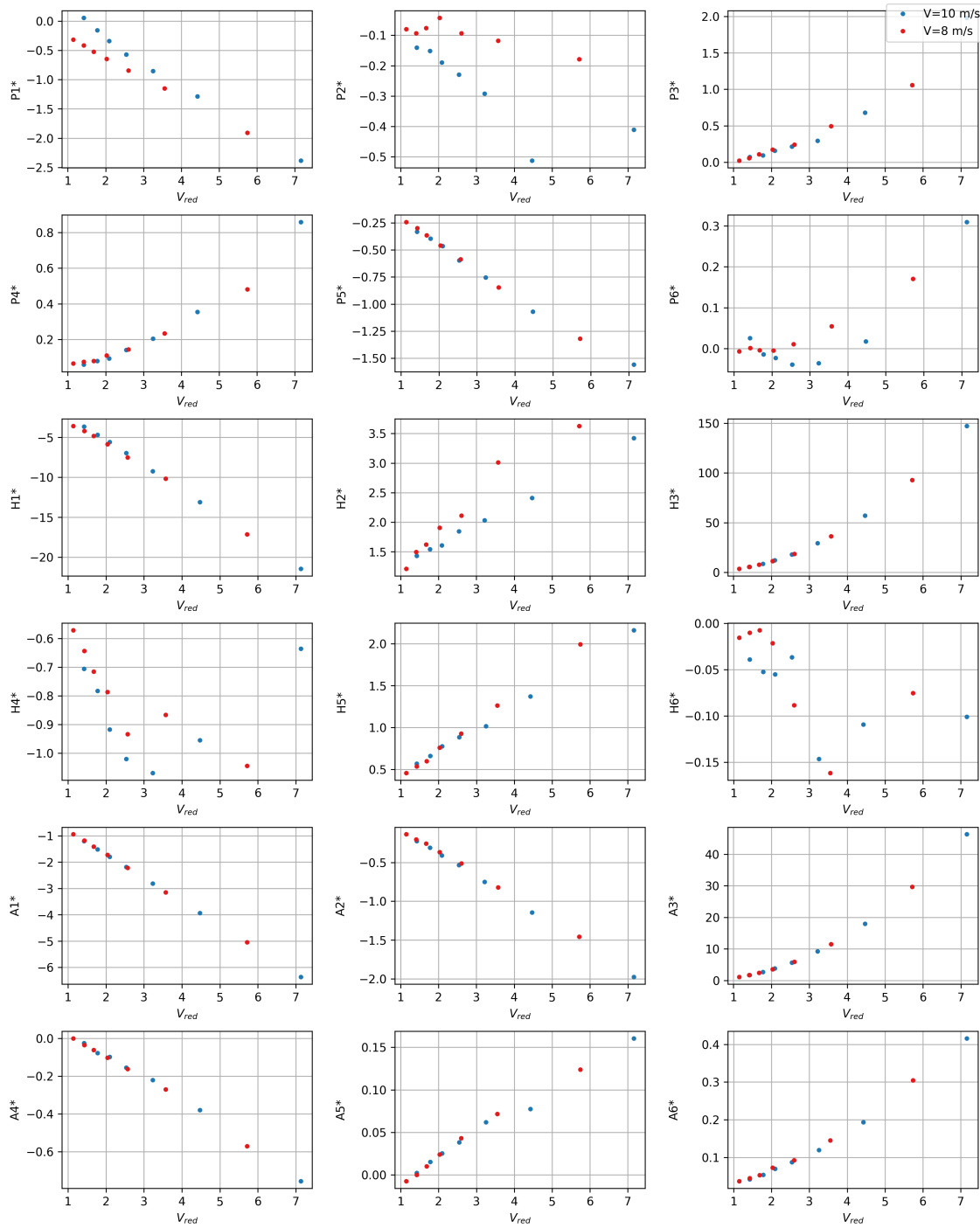


Figure C.1: Aerodynamic derivatives sampling data for girder height 3.5 m.

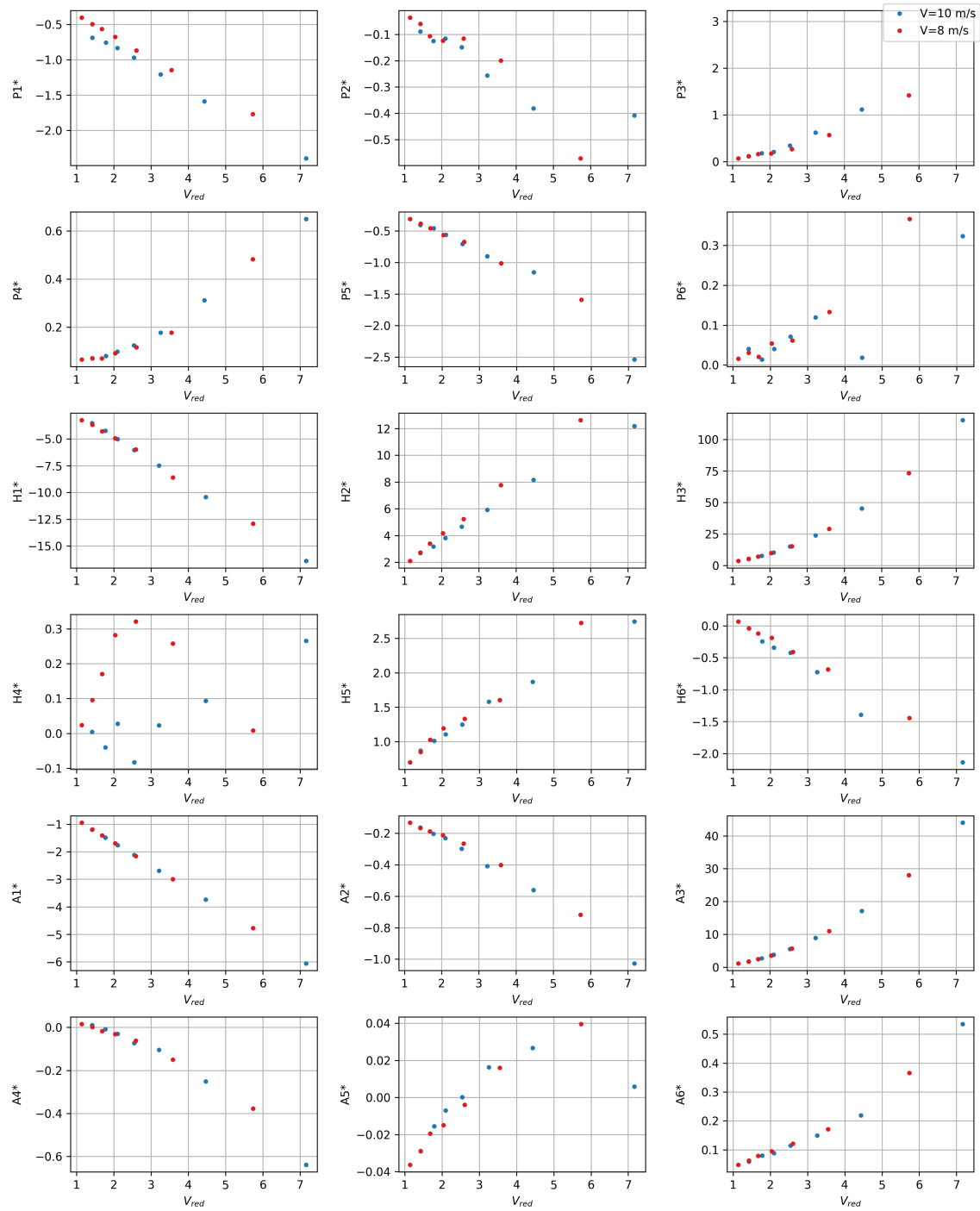


Figure C.2: Aerodynamic derivatives sampling data for girder height 3.75 m.

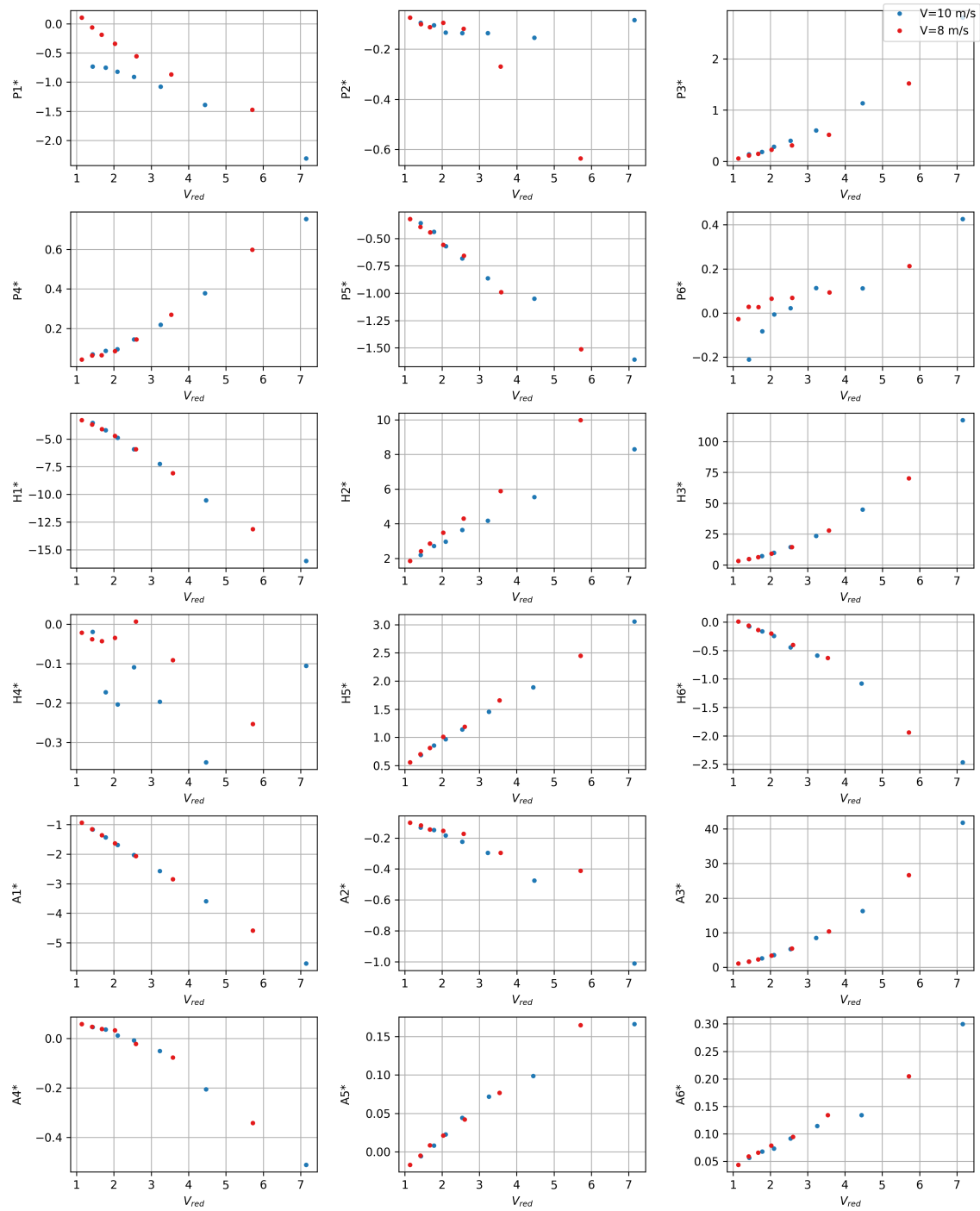


Figure C.3: Aerodynamic derivatives sampling data for girder height 4.0 m.

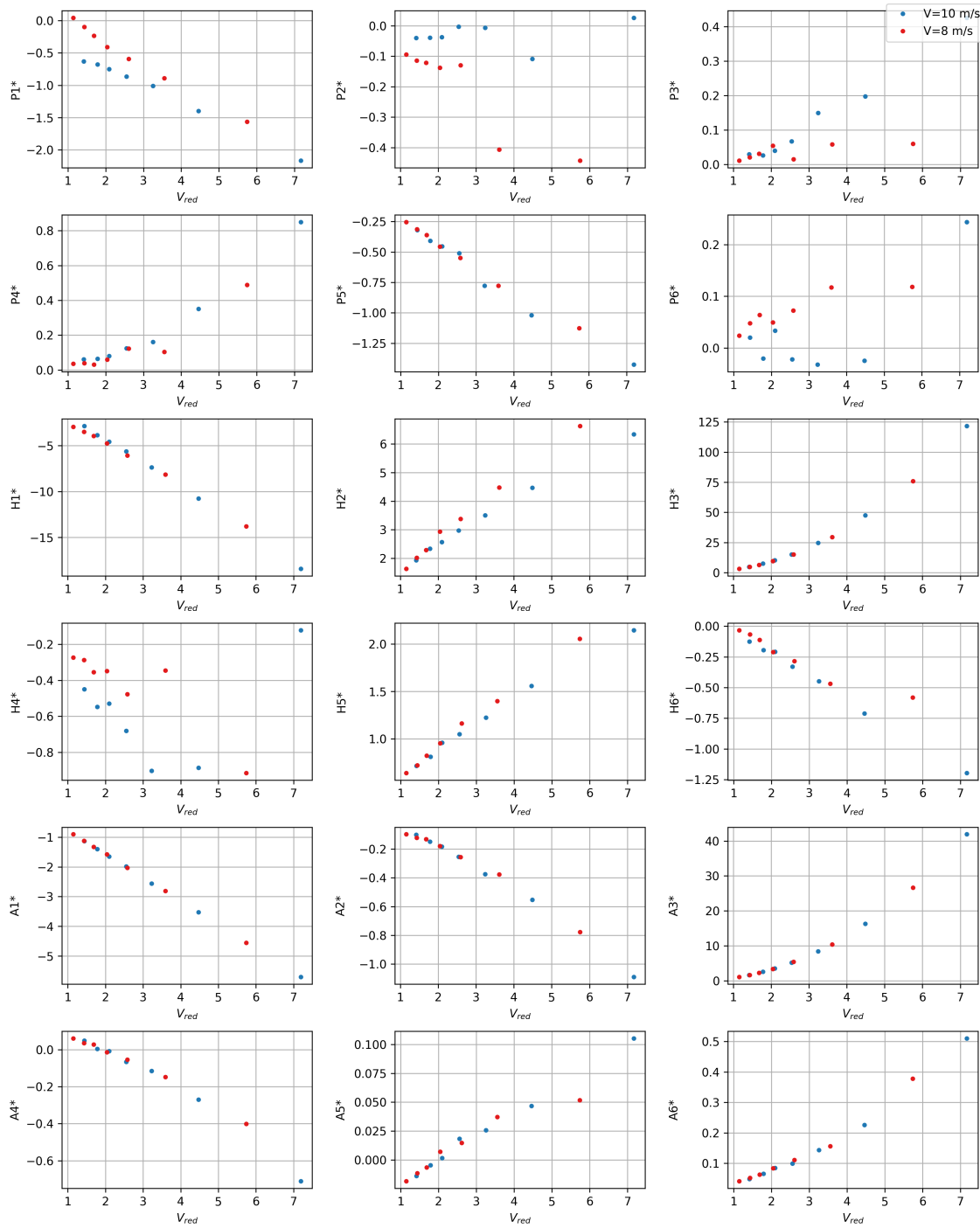


Figure C.4: Aerodynamic derivatives sampling data for girder height 4.25 m.

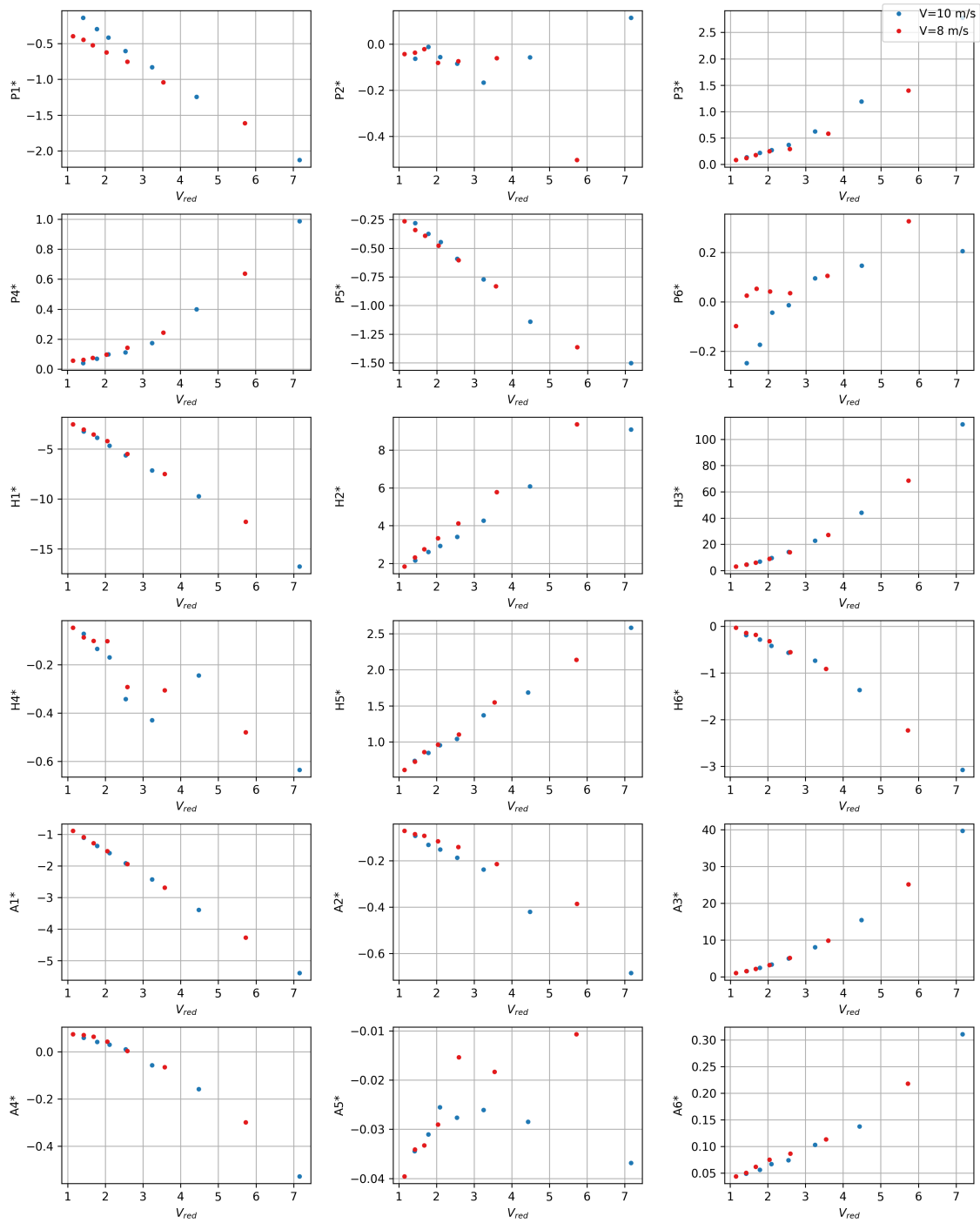


Figure C.5: Aerodynamic derivatives sampling data for girder height 4.5 m.

C.2 ADs: surrogate models

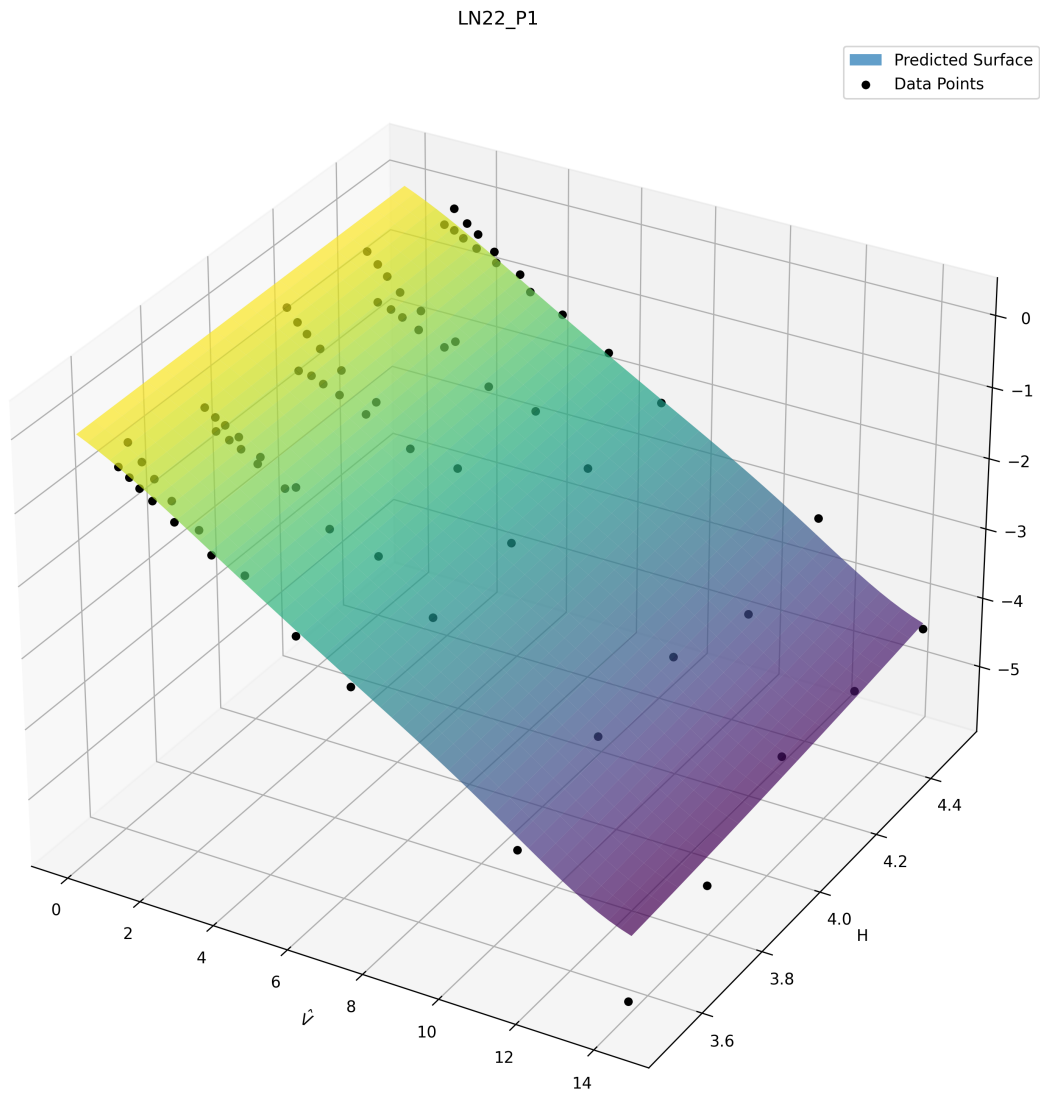


Figure C.6: Surrogate model for P1*.

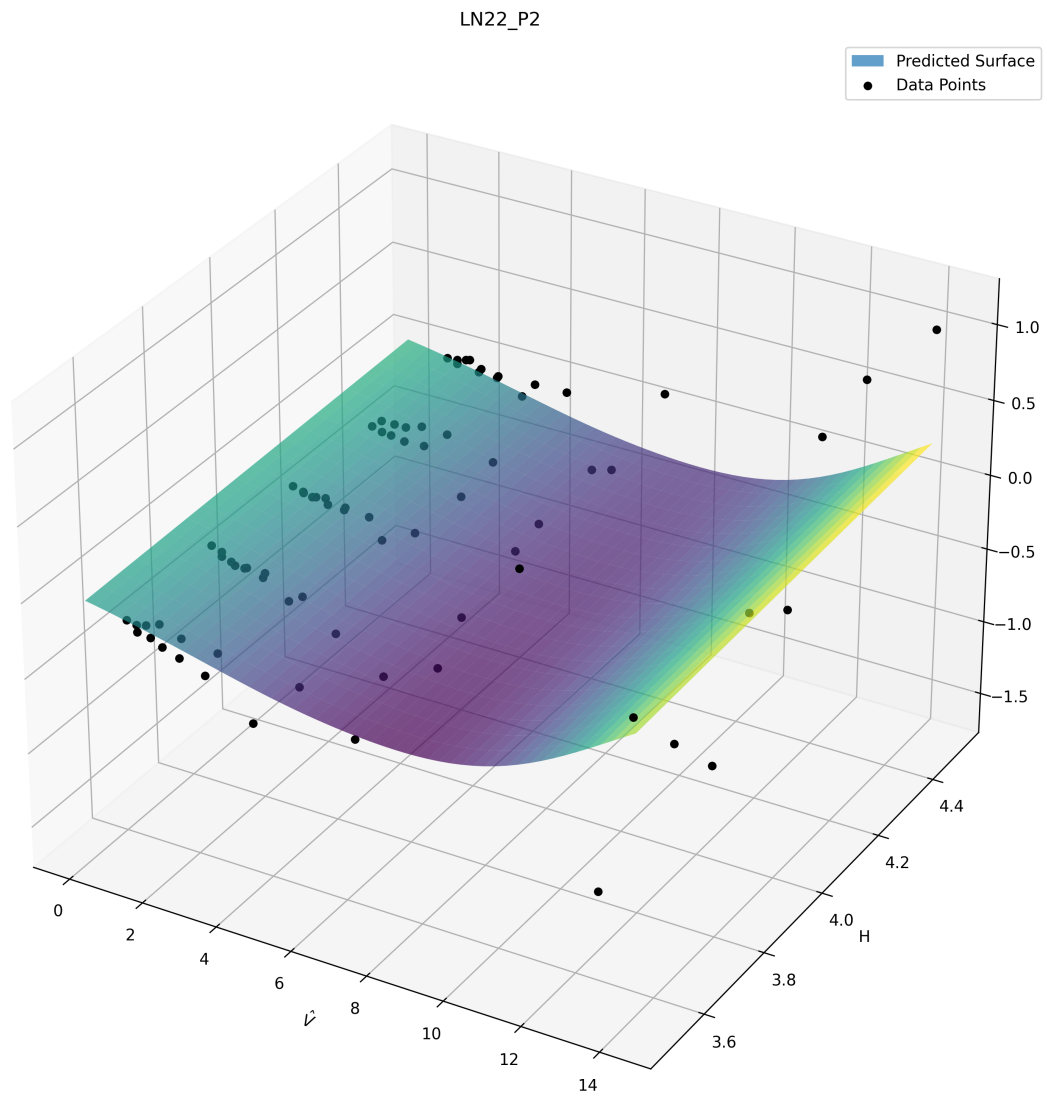


Figure C.7: Surrogate model for P2*.

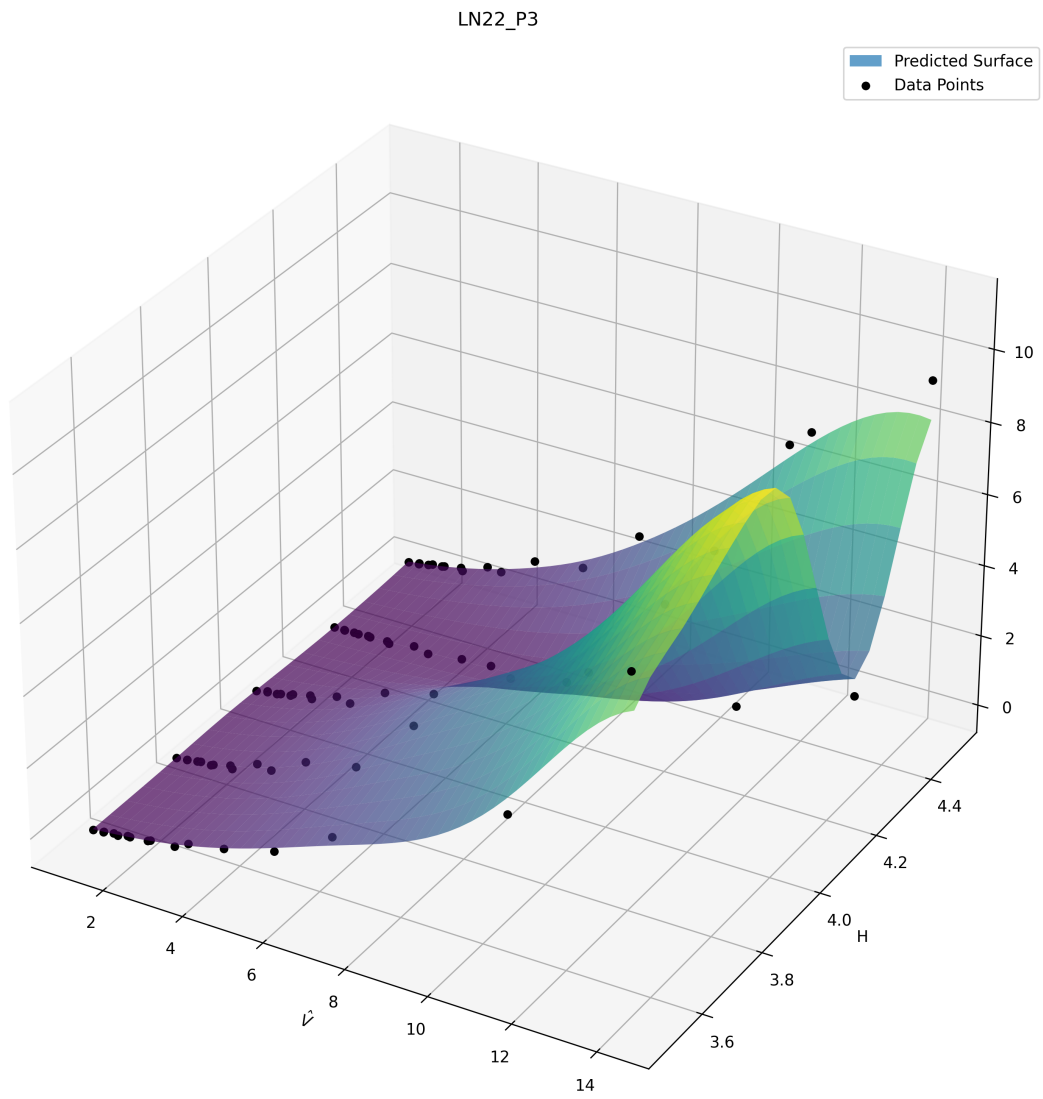


Figure C.8: Surrogate model for P3*.

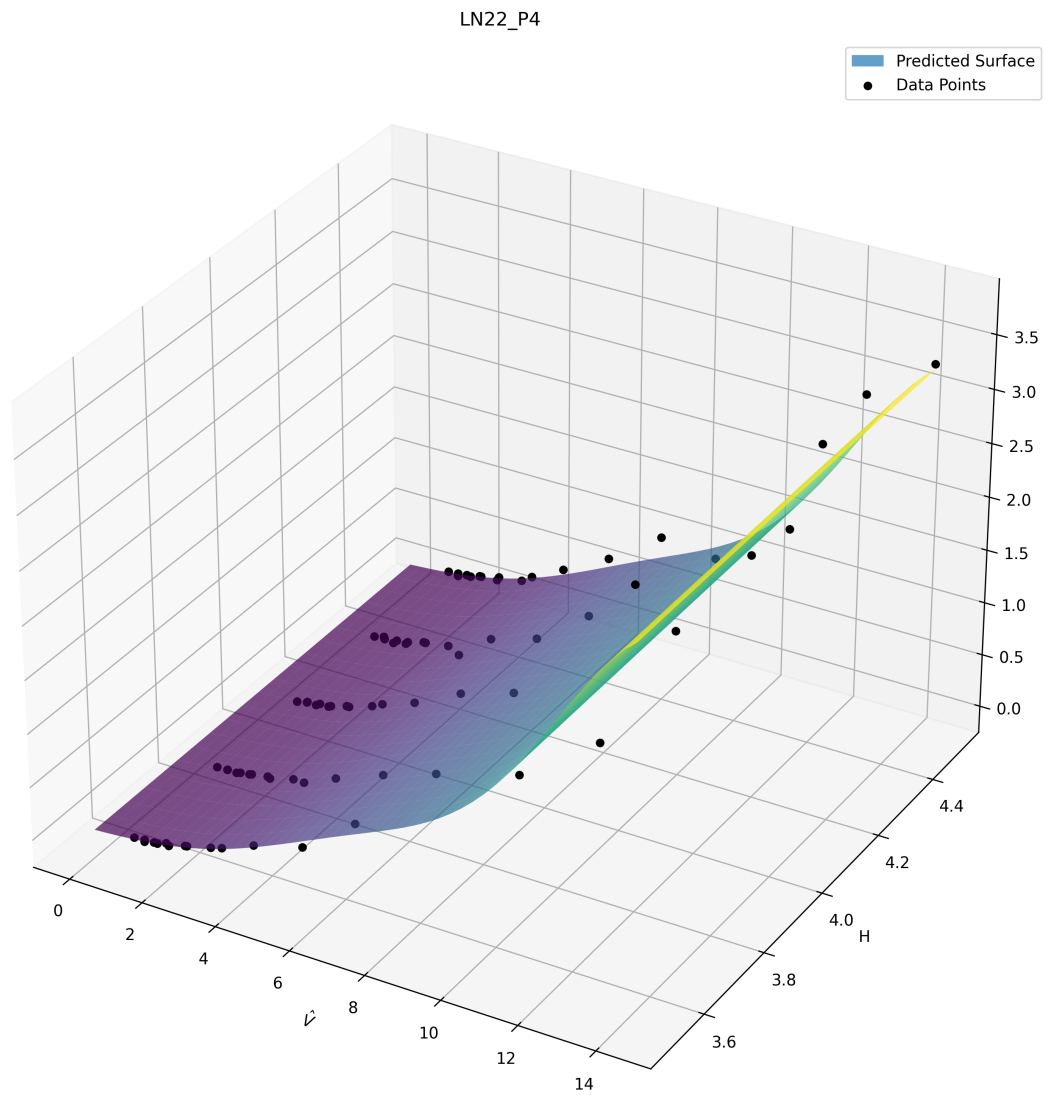


Figure C.9: Surrogate model for P4*.

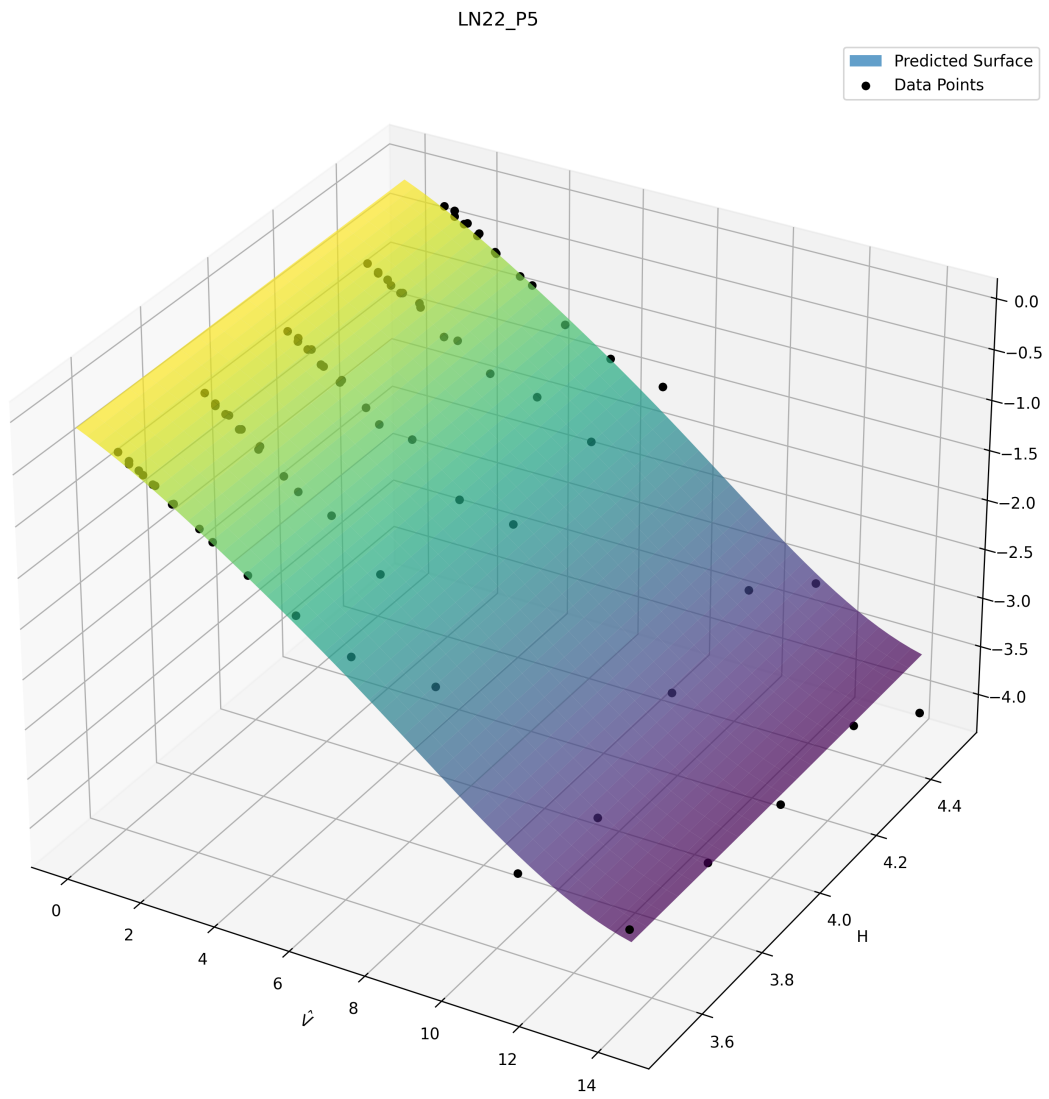
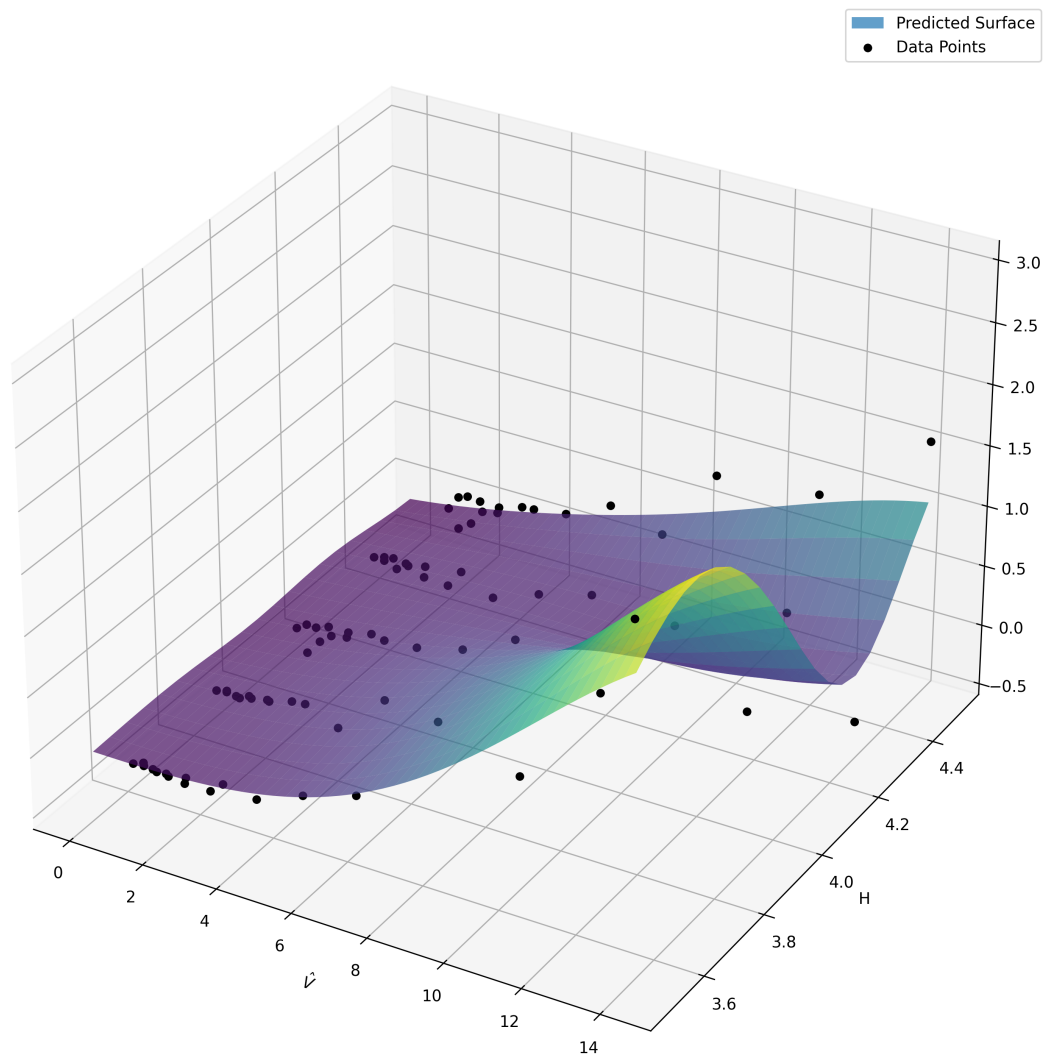


Figure C.10: Surrogate model for P5*.

LN22_P6

**Figure C.11:** Surrogate model for P6*.

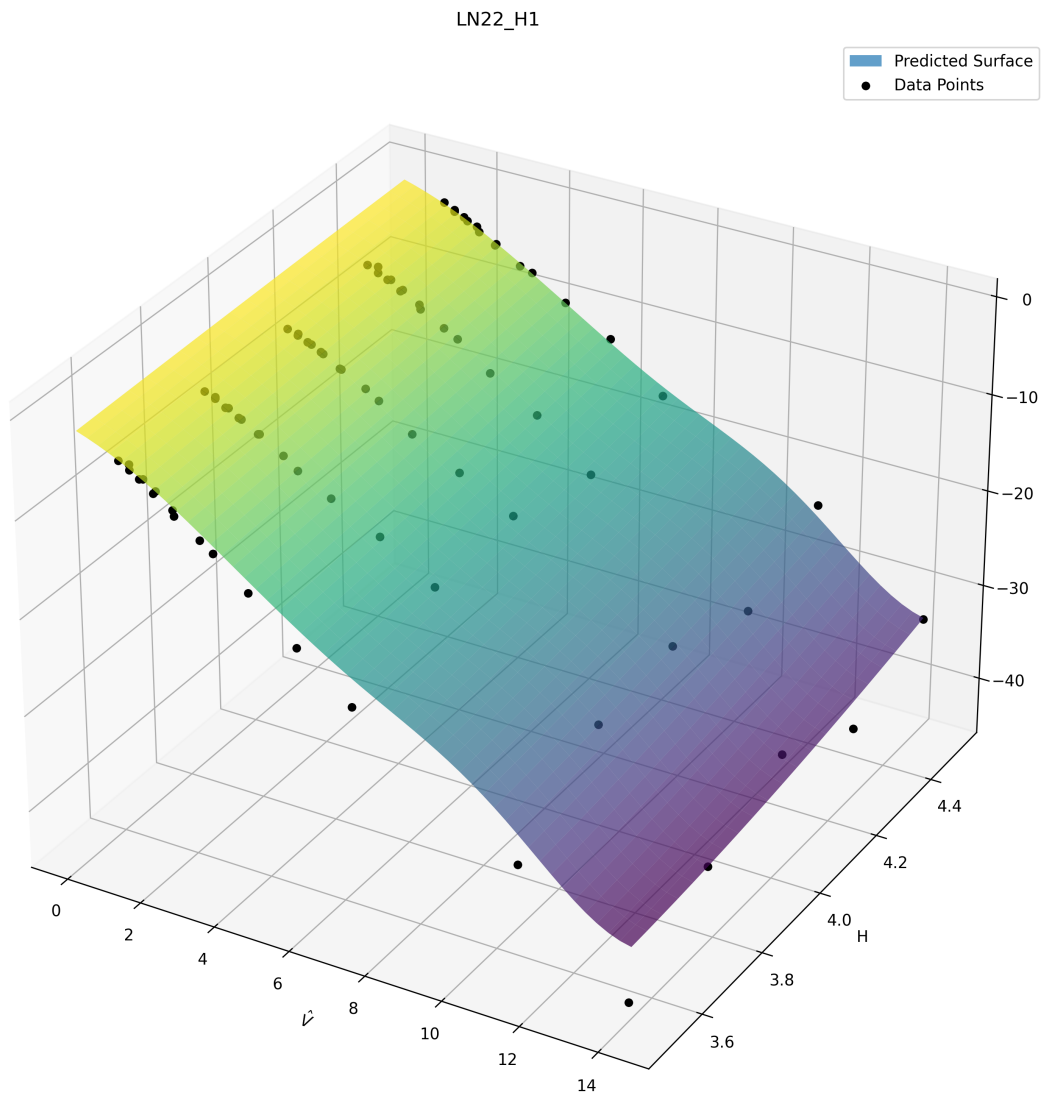


Figure C.12: Surrogate model for $H1^*$.

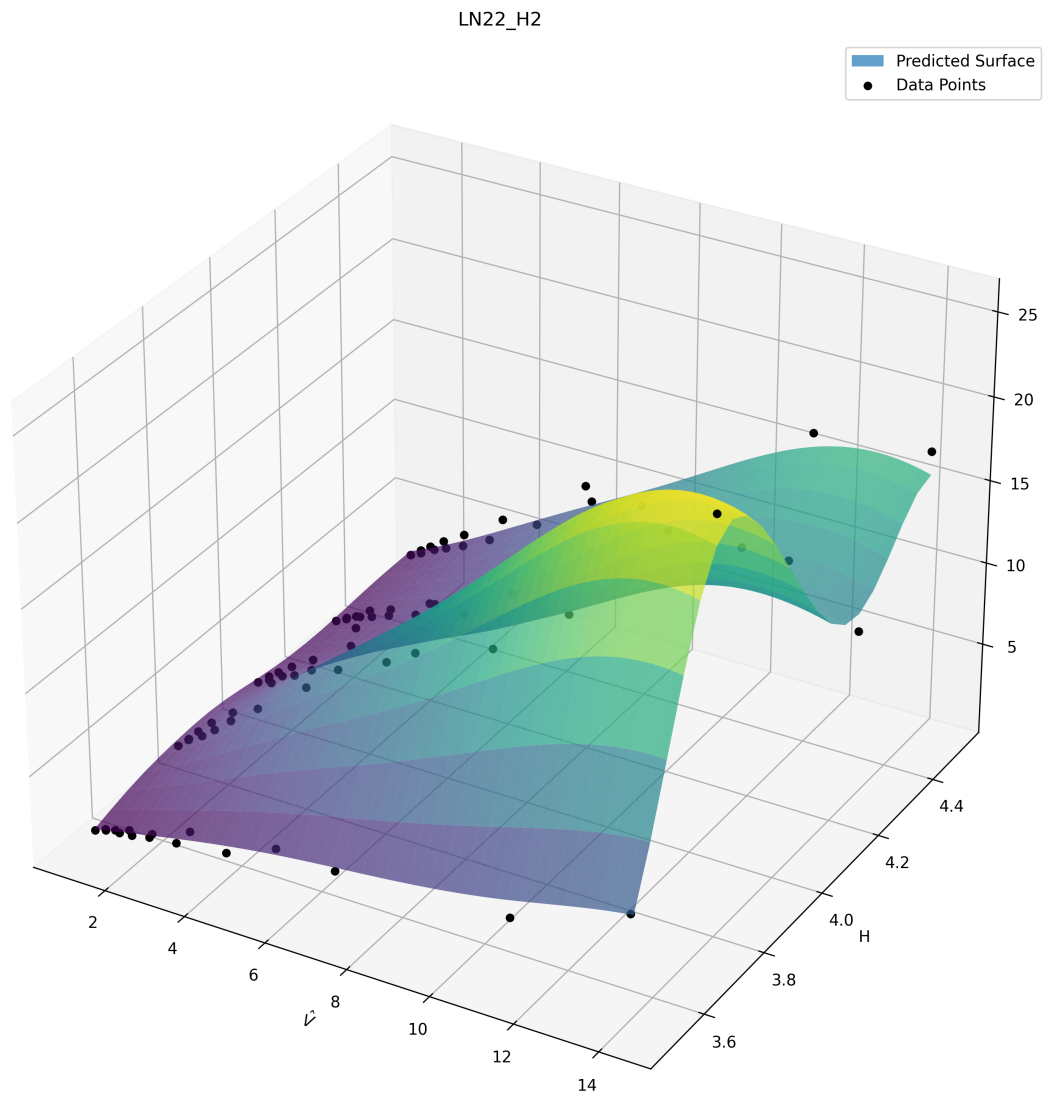


Figure C.13: Surrogate model for H2*.

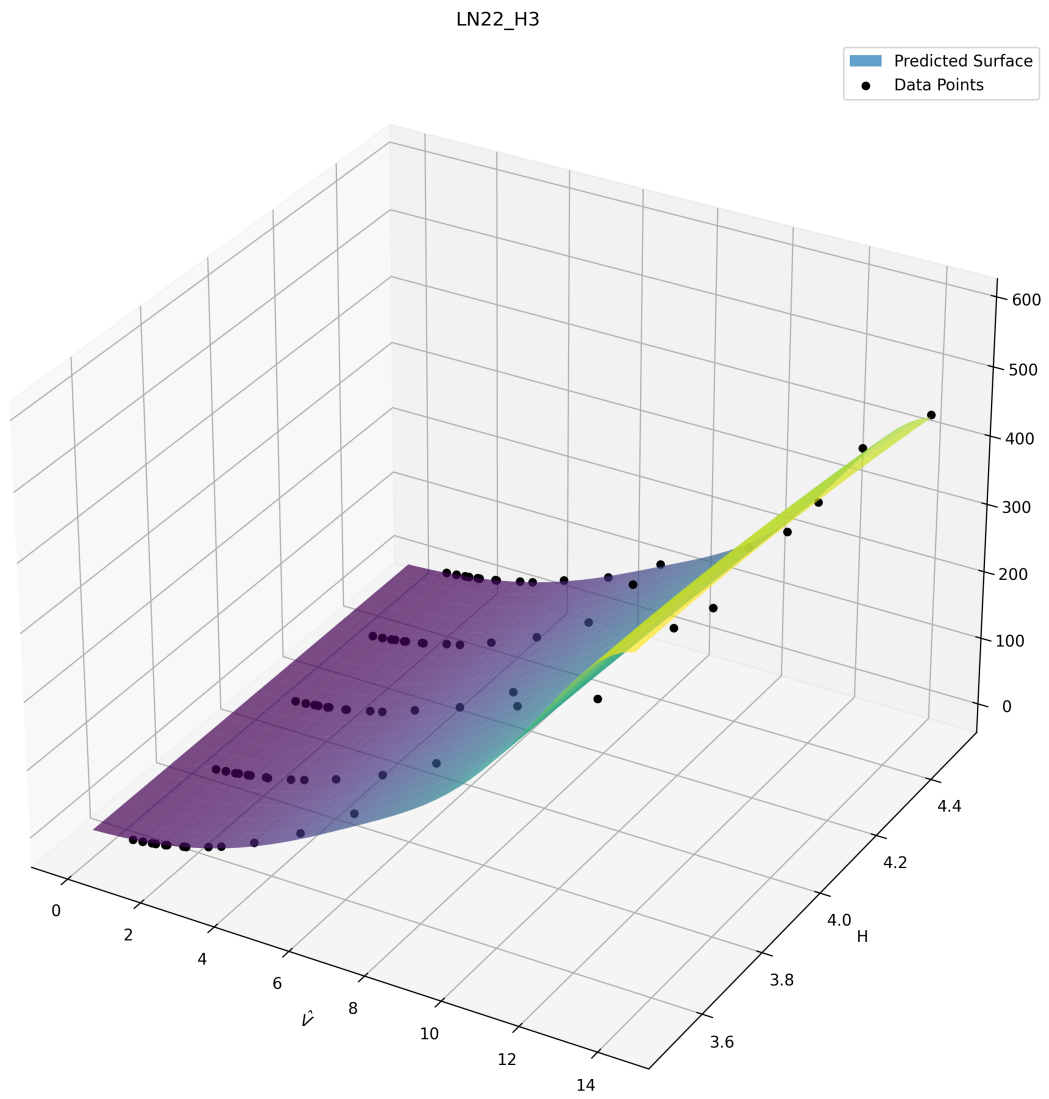


Figure C.14: Surrogate model for $H3^*$.

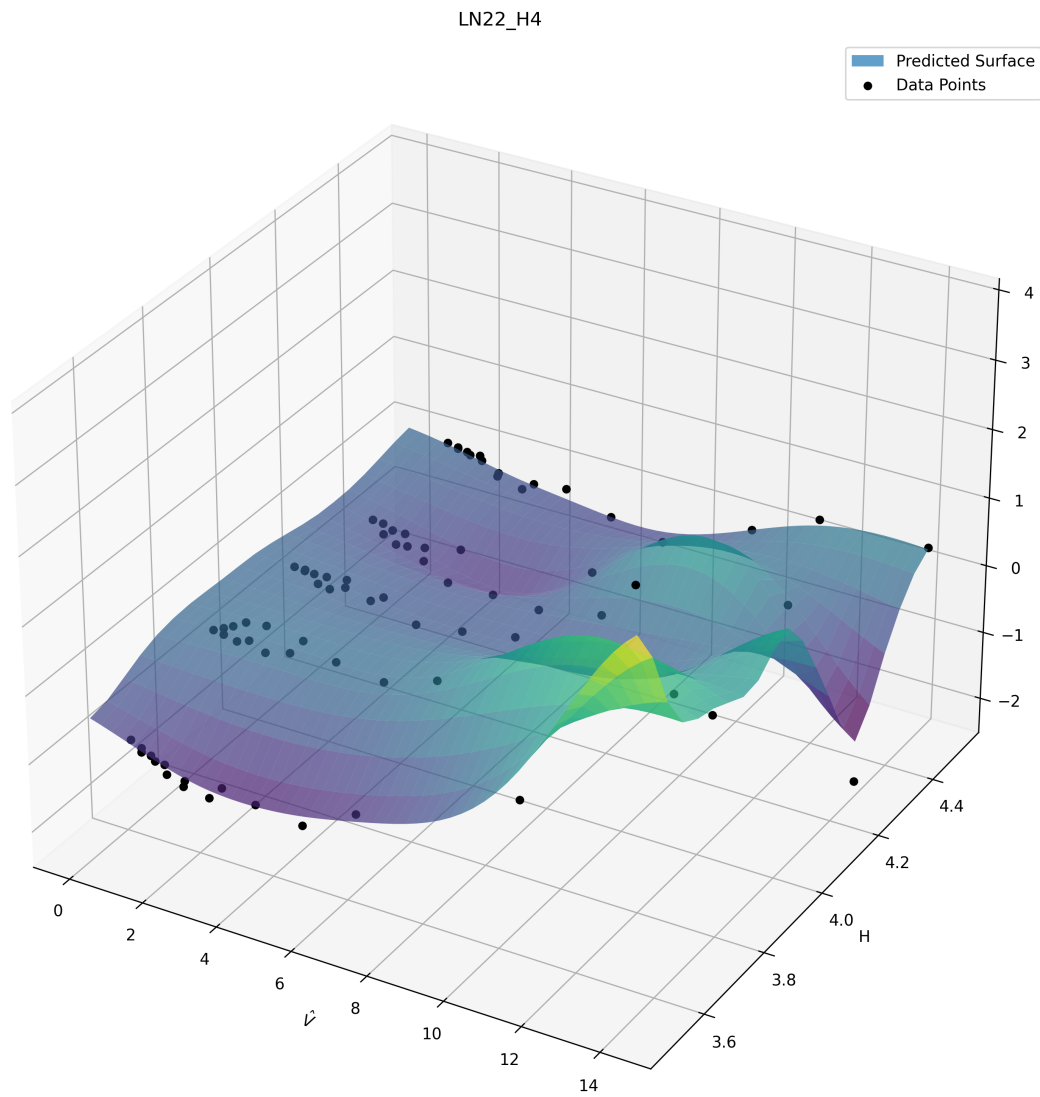


Figure C.15: Surrogate model for H4*.

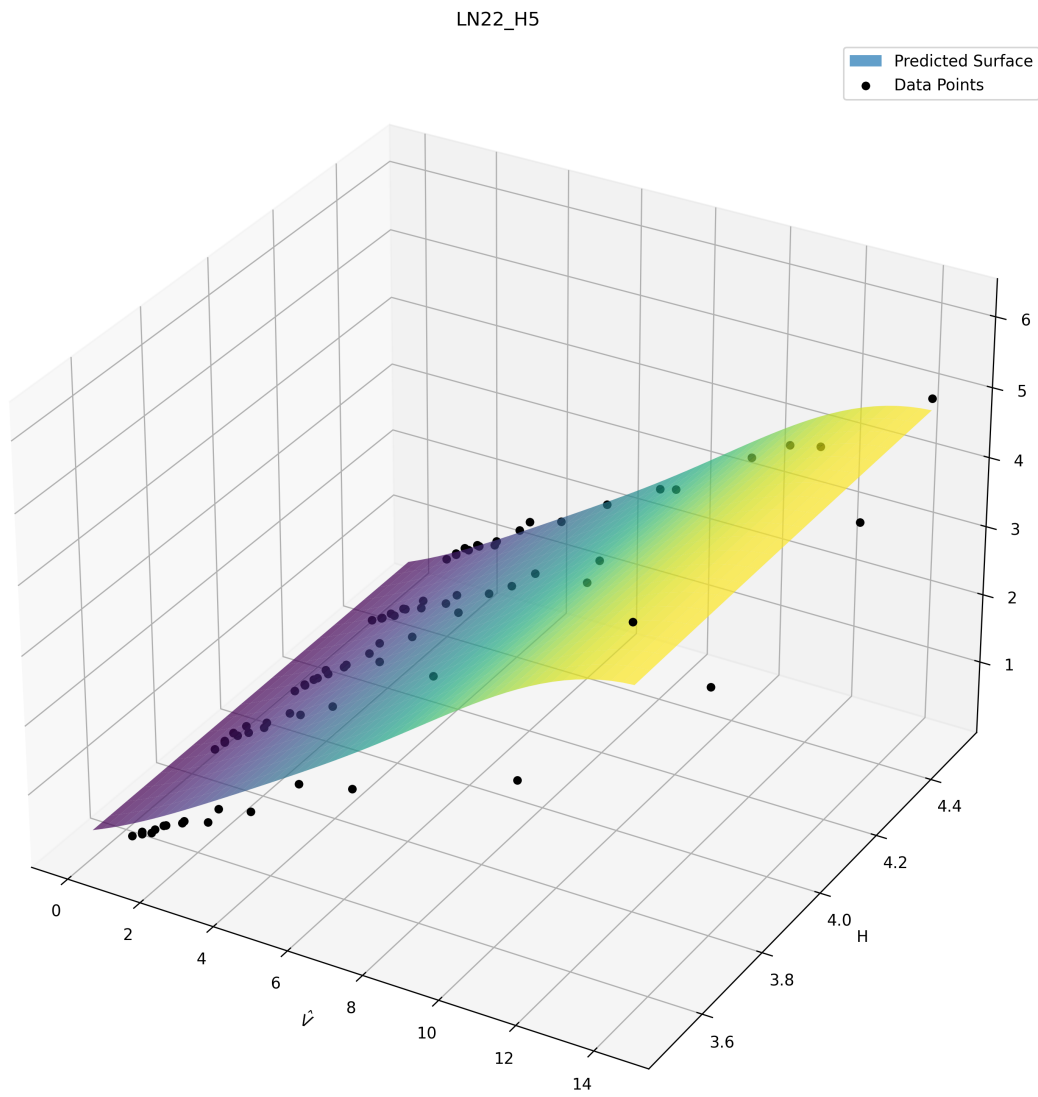


Figure C.16: Surrogate model for H5*.

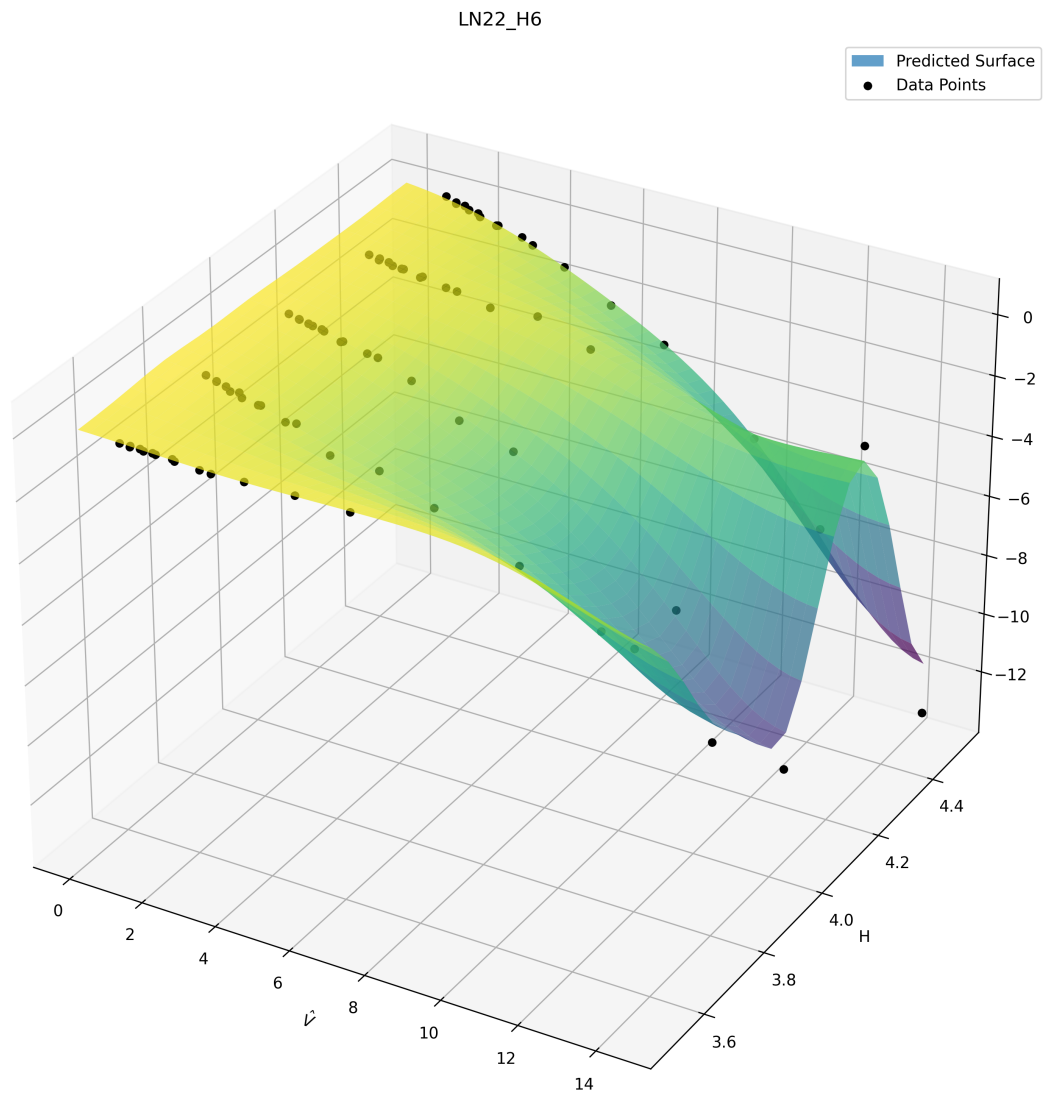


Figure C.17: Surrogate model for H6*.

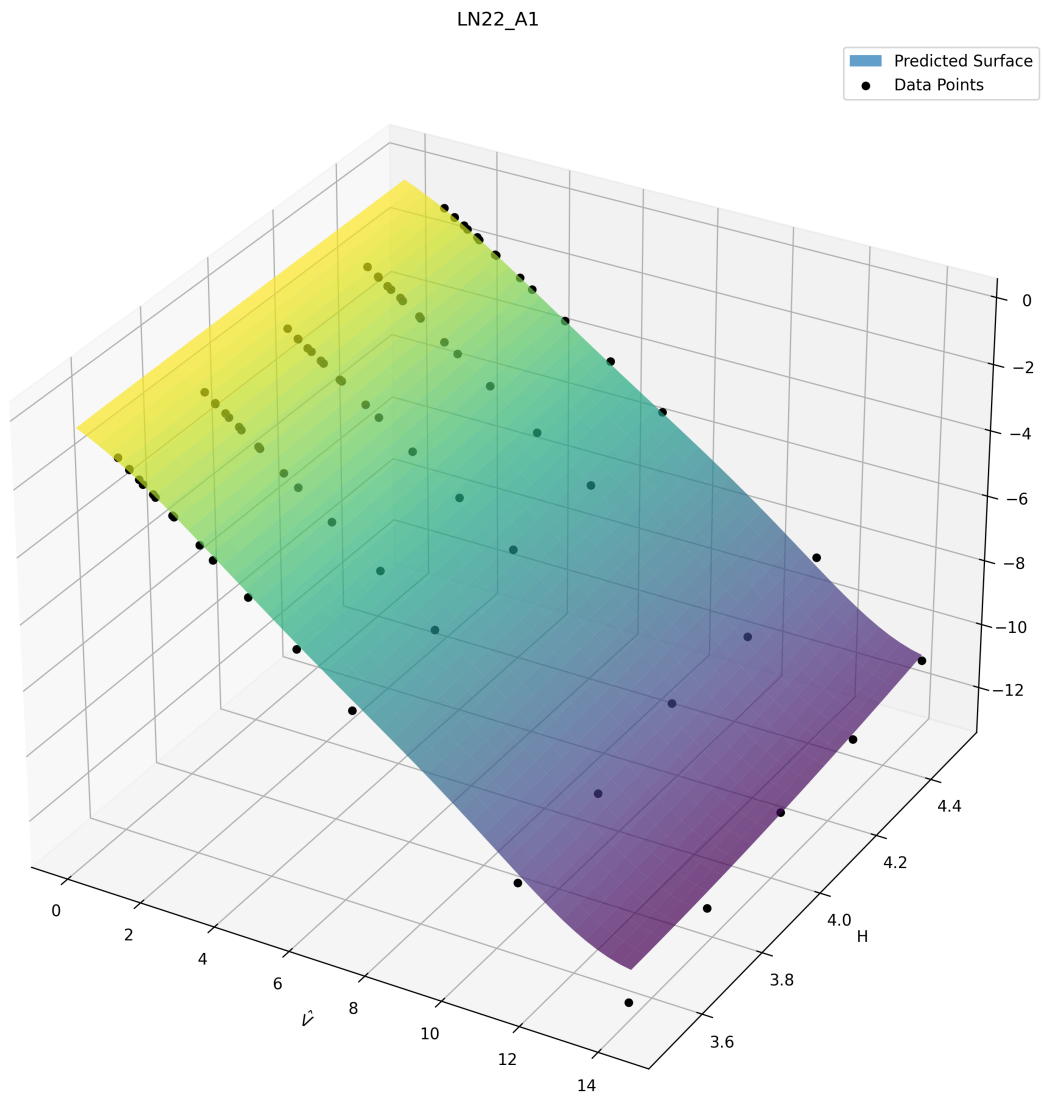


Figure C.18: Surrogate model for A1*.

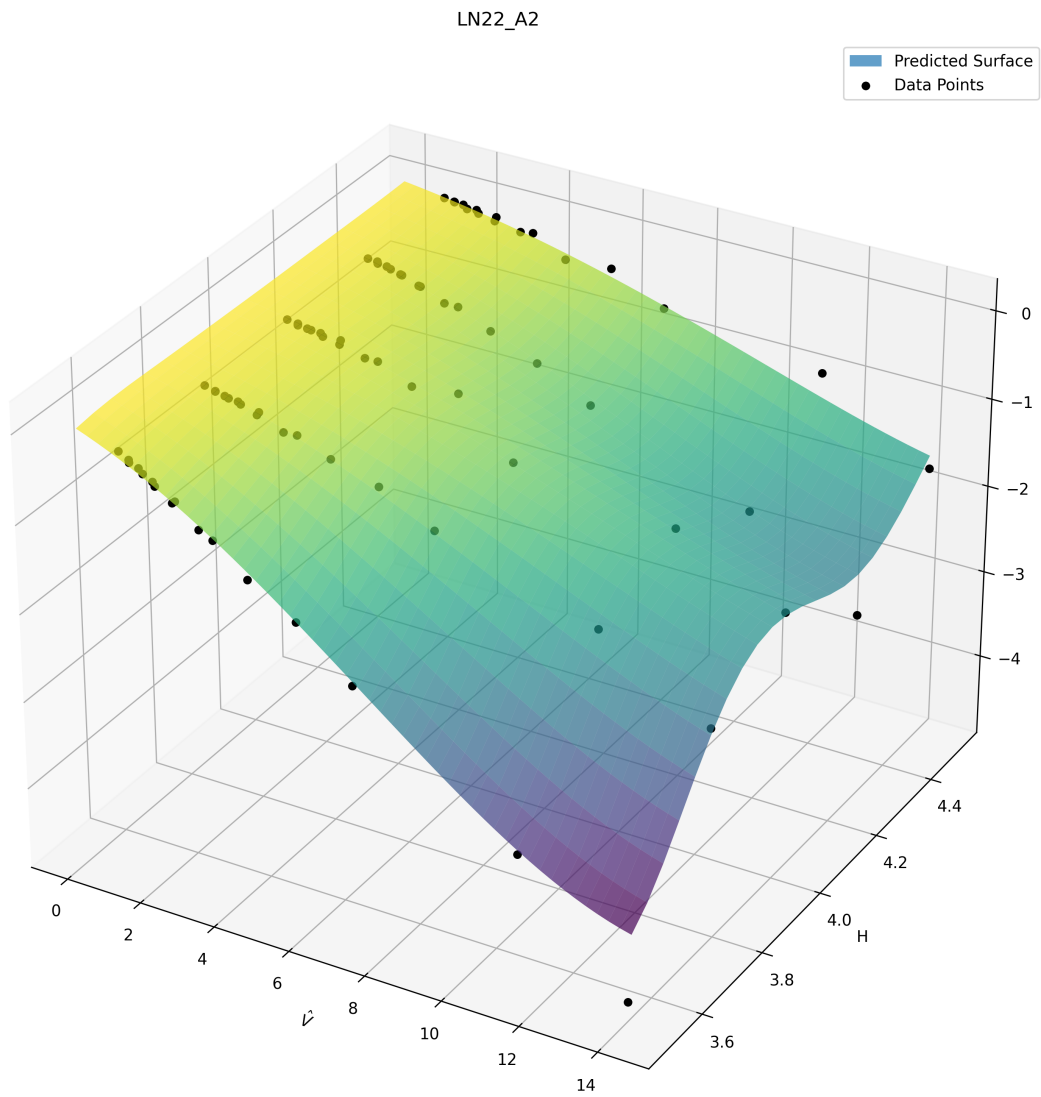


Figure C.19: Surrogate model for A2*.

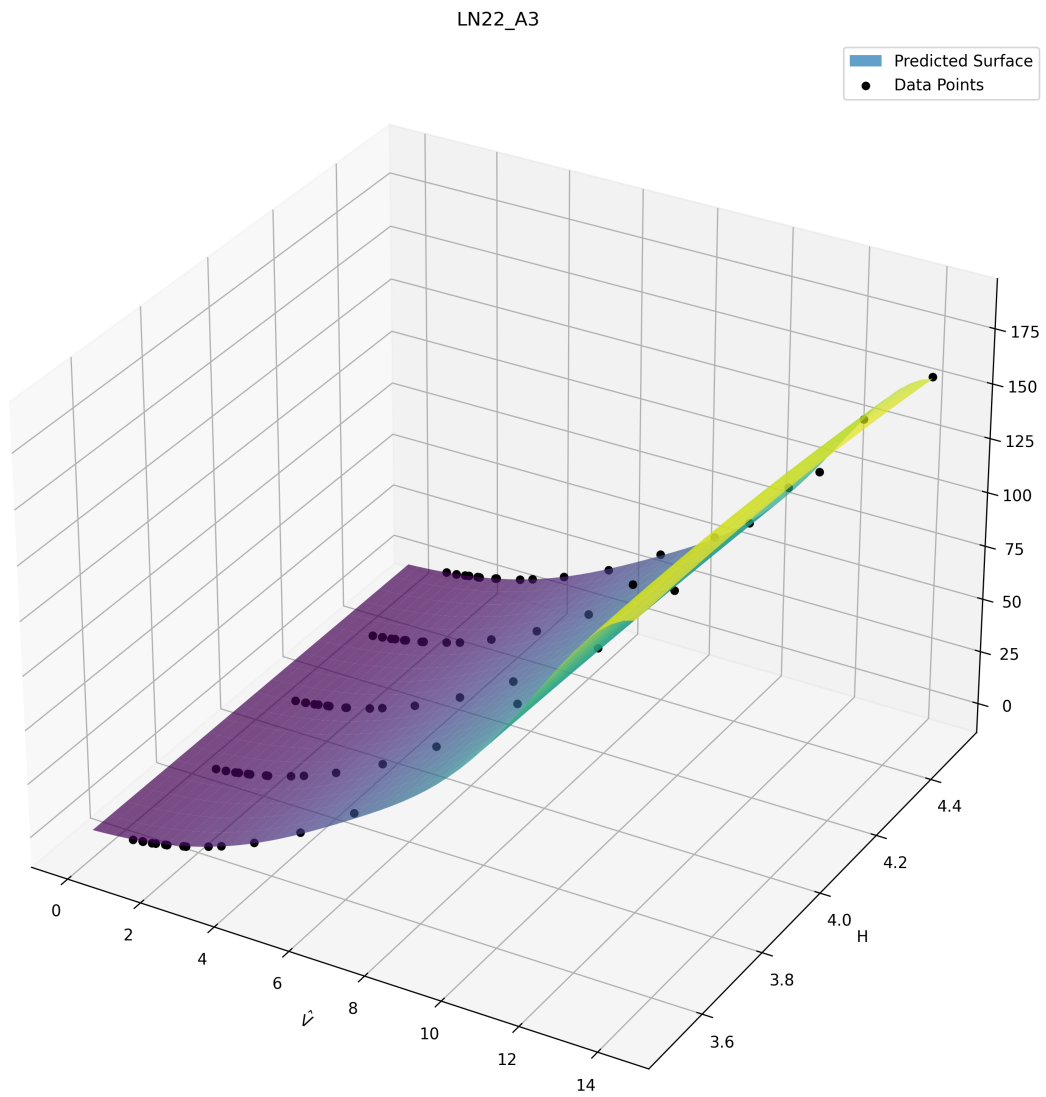


Figure C.20: Surrogate model for A3*.

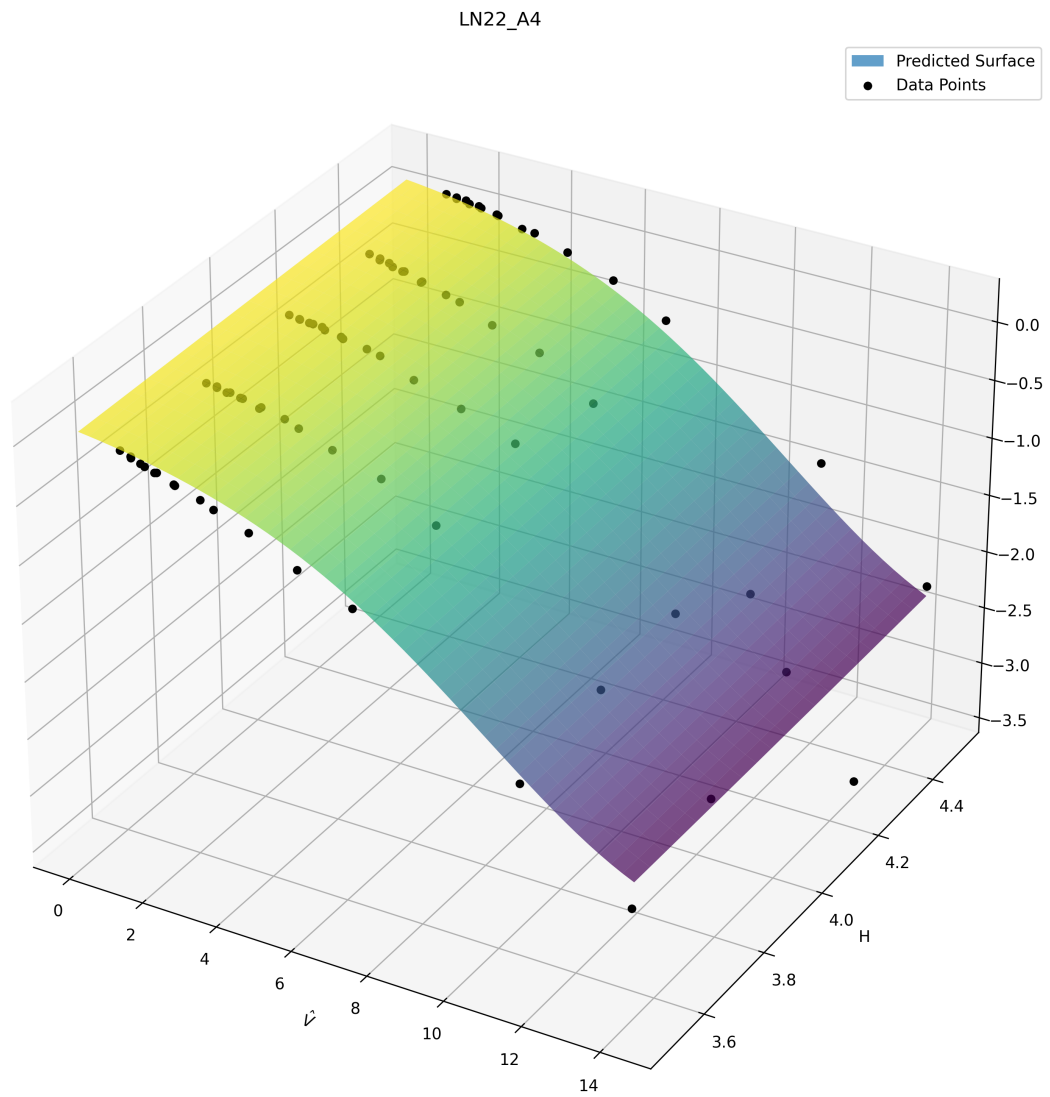


Figure C.21: Surrogate model for A4*.

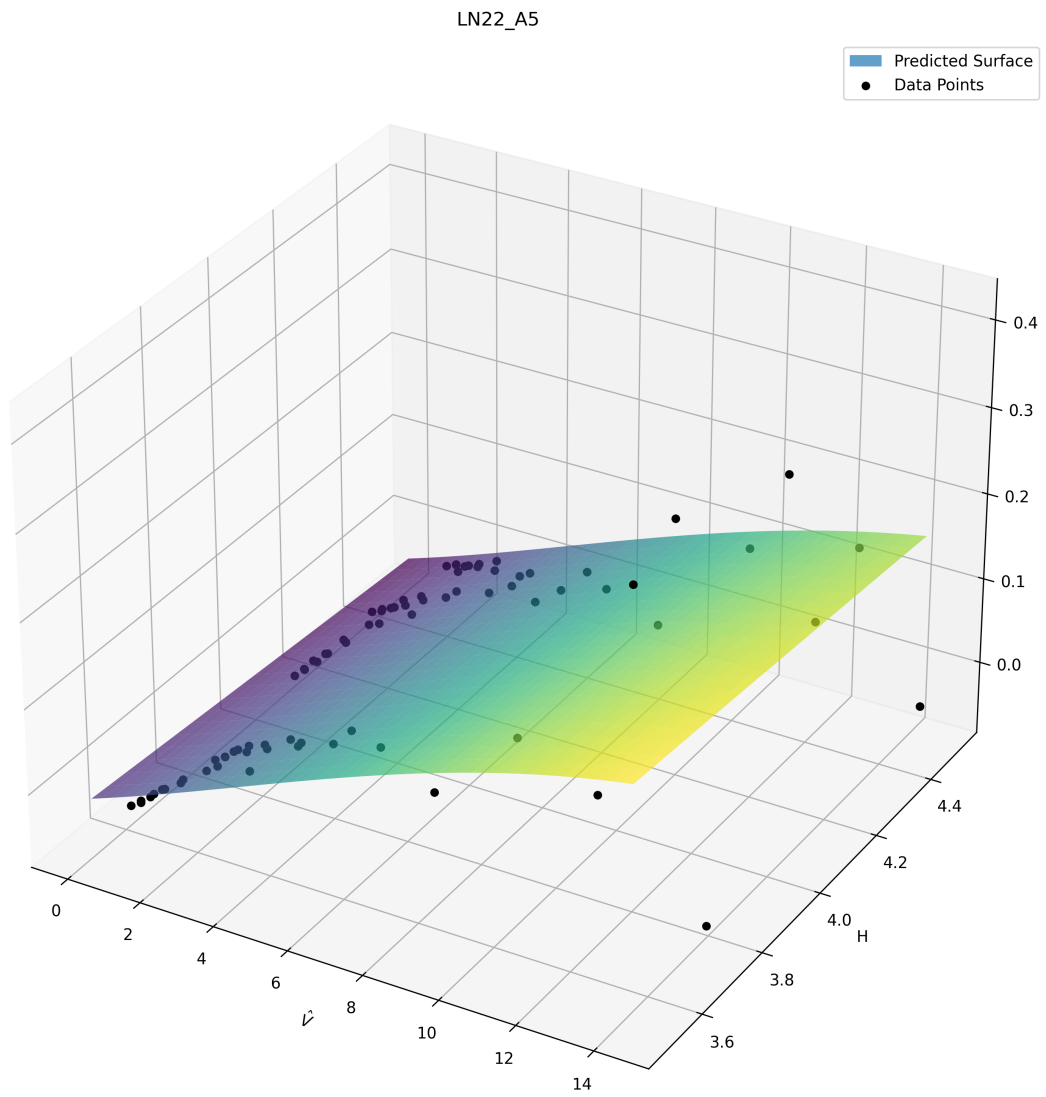


Figure C.22: Surrogate model for A5*.

LN22_A6

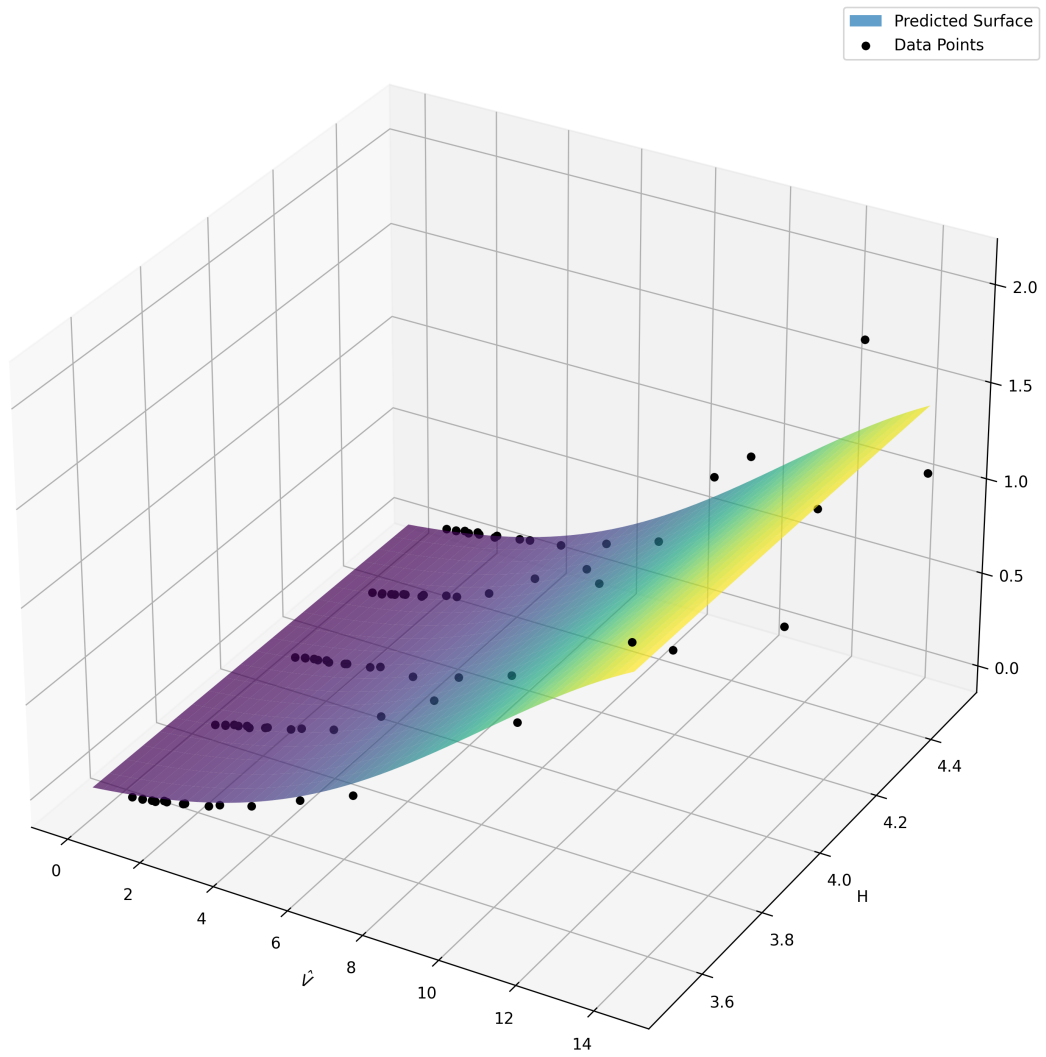


Figure C.23: Surrogate model for A6*.

Appendix D

Optimization

The data generated for the optimization algorithm is presented in this appendix.

Table D.1: Flutter speed for all generated configurations

h_t	h_g	$V_{cr}[m/s]$	h_t	h_g	$V_{cr}[m/s]$	h_t	h_g	$V_{cr}[m/s]$
180	3.5	71.1	194	3.5	76.2	208	3.5	79.1
180	3.75	62.9	194	3.75	66.2	208	3.75	72.3
180	4	64	194	4	67.9	208	4	74
180	4.25	70.6	194	4.25	74.7	208	4.25	81
180	4.5	64.4	194	4.5	69.7	208	4.5	77.7
182	3.5	72.1	196	3.5	76.5	210	3.5	79.6
182	3.75	63.5	196	3.75	66.7	210	3.75	73.7
182	4	64.8	196	4	68.5	210	4	75.3
182	4.25	71.3	196	4.25	75.3	210	4.25	82.3
182	4.5	65.2	196	4.5	71	210	4.5	73
184	3.5	73.3	198	3.5	76.9	212	3.5	80.1
184	3.75	64.2	198	3.75	67.4	212	3.75	75.2
184	4	65.4	198	4	69.4	212	4	76.6
184	4.25	72.2	198	4.25	76	212	4.25	83.6
184	4.5	65.8	198	4.5	72.9	212	4.5	73.7
186	3.5	74.9	200	3.5	77.2	214	3.5	80.8
186	3.75	64.5	200	3.75	68.1	214	3.75	76.9
186	4	65.8	200	4	70.3	214	4	76.8
186	4.25	72.8	200	4.25	76.8	214	4.25	85.2
186	4.5	66.2	200	4.5	72.2	214	4.5	74.6
188	3.5	77	202	3.5	77.6	216	3.5	81.7
188	3.75	64.8	202	3.75	68.8	216	3.75	78.1
188	4	66.2	202	4	71.4	216	4	76
188	4.25	73.2	202	4.25	77.5	216	4.25	84.7
188	4.5	66.8	202	4.5	73.3	216	4.5	76.4
190	3.5	75.6	204	3.5	78.1	218	3.5	79.6
190	3.75	65.2	204	3.75	69.9	218	3.75	75.8
190	4	66.7	204	4	72.9	218	4	76.1
190	4.25	73.7	204	4.25	78.6	218	4.25	83.6
190	4.5	67.6	204	4.5	75.1	218	4.5	74
192	3.5	75.8	206	3.5	78.5	220	3.5	81.2
192	3.75	65.6	206	3.75	71	220	3.75	75.1
192	4	67.1	206	4	74.5	220	4	77.2
192	4.25	74.1	206	4.25	79.6	220	4.25	83.5
192	4.5	68.4	206	4.5	76.7	220	4.5	73.9

Table D.2: Total cost for all generated configurations

h_t	h_g	Cost [NOK]	h_t	h_g	Cost [NOK]	h_t	h_g	Cost [NOK]
180	3.5	2154678461	194	3.5	2104077869	208	3.5	2037496442
180	3.75	2173819683	194	3.75	2088494911	208	3.75	2029349924
180	4	2176541032	194	4	2091064673	208	4	2031797484
180	4.25	2178915975	194	4.25	2093317870	208	4.25	2033952649
180	4.5	2181275800	194	4.5	2095557728	208	4.5	2036095644
182	3.5	2159841638	196	3.5	2092253777	210	3.5	2030846526
182	3.75	2164244515	196	3.75	2077784505	210	3.75	2023375726
182	4	2166944994	196	4	2080335039	210	4	2025807652
182	4.25	2169303067	196	4.25	2082572838	210	4.25	2027950206
182	4.5	2171646454	196	4.5	2084797466	210	4.5	2030080803
184	3.5	2157693008	198	3.5	2081141225	212	3.5	2024723797
184	3.75	2152292256	198	3.75	2067946408	212	3.75	2017894225
184	4	2154970406	198	4	2070478470	212	4	2020310913
184	4.25	2157310500	198	4.25	2072701475	212	4.25	2022441154
184	4.5	2159636232	198	4.5	2074911471	212	4.5	2024559671
186	3.5	2150626991	200	3.5	2070834091	214	3.5	2019072648
186	3.75	2139160693	200	3.75	2058904143	214	3.75	2012871616
186	4	2141816053	200	4	2061418359	214	4	2015273452
186	4.25	2144137841	200	4.25	2063627067	214	4.25	2017391672
186	4.5	2146445523	200	4.5	2065822921	214	4.5	2019498420
188	3.5	2140513340	202	3.5	2061352868	216	3.5	2013866749
188	3.75	2125725330	202	3.75	2050580778	216	3.75	2008270673
188	4	2128358128	202	4	2053077675	216	4	2010658011
188	4.25	2130661821	202	4.25	2055272496	216	4.25	2012764489
188	4.5	2132951623	202	4.5	2057454620	216	4.5	2014859748
190	3.5	2128761977	204	3.5	2052674700	218	3.5	2009121099
190	3.75	2112585898	204	3.75	2042913210	218	3.75	2004047602
190	4	2115196793	204	4	2045393245	218	4	2006420736
190	4.25	2117482932	204	4.25	2047574533	218	4.25	2008515717
190	4.5	2119755375	204	4.5	2049743285	218	4.5	2010599715
192	3.5	2116388144	206	3.5	2044643286	220	3.5	2004904129
192	3.75	2100113003	206	3.75	2035747174	220	3.75	2000148877
192	4	2102702867	206	4	2038210769	220	4	2002508001
192	4.25	2104972161	206	4.25	2040378844	220	4.25	2004591669
192	4.5	2107227941	206	4.5	2042534556	220	4.5	2006664542

